

1-1-2010

Dynamic Multivariate Simplex Splines For Volume Representation And Modeling

Yunhao Tan

Wayne State University

Follow this and additional works at: http://digitalcommons.wayne.edu/oa_dissertations



Part of the [Computer Sciences Commons](#)

Recommended Citation

Tan, Yunhao, "Dynamic Multivariate Simplex Splines For Volume Representation And Modeling" (2010). *Wayne State University Dissertations*. Paper 53.

This Open Access Dissertation is brought to you for free and open access by DigitalCommons@WayneState. It has been accepted for inclusion in Wayne State University Dissertations by an authorized administrator of DigitalCommons@WayneState.

**DYNAMIC MULTIVARIATE SIMPLEX SPLINES FOR VOLUME
REPRESENTATION AND MODELING**

by

YUNHAO TAN

DISSERTATION

Submitted to the Graduate School

of Wayne State University,

Detroit, Michigan

in partial fulfillment of the requirements

for the degree of

DOCTOR OF PHILOSOPHY

2010

MAJOR: COMPUTER SCIENCE

Approved by:

Advisor

Date

© COPYRIGHT BY
YUNHAO TAN
2010
All Rights Reserved

DEDICATION

To the memories of my beloved grandfather.

ACKNOWLEDGMENTS

First of all, I would like to express my special appreciation to my advisor, Dr. Jing Hua, for his continuous support in the Ph.D. program. During my Ph.D. study in Wayne State University these years, he has spent tremendous time and effort with me discussing research, teaching me to write papers, and answering my questions. He was always there to listen, discuss, and give advice. This dissertation would not have been possible without him.

Besides my advisor, I am very grateful to Dr. Farshad Fotouhi, Dr. Ming Dong, and Dr. Xiaohu Guo, for serving on my prospectus and dissertation committee. They gave me plenty of constructive suggestions and invaluable comments on this dissertation.

Also, I thank all my colleagues in Graphics & Imaging Laboratory, Dr. Guangyu Zou, Chang Liu, Darshan Pai, Jiaxi Hu, Zhaoqiang Lai, and Vahid Taimouri, for having insightful discussions with me.

I deeply acknowledge the support from my girl friend, Cui Lin, and my friends, Ron and Catherine Priskorn. They dedicated quite a lot of effort to the grammar and wording of my dissertation.

Last but not least, I am greatly indebted to my parents: my father, Baocai Tan, and my mother, Shifang Xue, for giving me life in the first place, for believing in me, for educating me, for unconditional support and encouragement to pursue my interests, even when the interests went beyond boundaries of experience, language, field, and geography. I hope I have made them as well as my whole family proud.

TABLE OF CONTENTS

Dedication	ii
Acknowledgments	iii
List of Tables	viii
List of Figures	ix
Chapter 1	
Introduction	1
1.1 Motivation	1
1.2 Contributions	6
1.3 Dissertation Organization	8
Chapter 2	
Background	10
2.1 Volume Representation Approaches	10
2.1.1 Parametric Volume Representation Approaches	10
2.1.2 Nonparametric Volume Representation Approaches	12
2.1.3 Comparison between Volume Representation Schemes	13
2.2 Solid Modeling Approaches	14
2.2.1 Boundary Schemes	14
2.2.2 Decomposition Schemes	15
2.2.3 Constructive Solid Geometry	15
2.3 Physically Based Modeling Approaches	16
2.3.1 Deformable Models	16
2.3.2 Physics-based Geometric Design	17
2.3.3 Geometric Modeling with Particle Systems	18
Chapter 3	
Volume Reconstruction with Multivariate Simplex Splines	20

3.1	Introduction and Motivation	20
3.2	Previous Work	22
3.3	Multivariate Simplex Spline Volume	24
3.3.1	Multivariate Simplex Splines Definition	24
3.3.2	Multivariate Simplex Spline Volume Definition	24
3.4	Tetrahedral Domain Construction	28
3.4.1	Initial Alignment of 2D Slices	28
3.4.2	Carver Algorithm for Tetrahedralization	30
3.5	Volume Reconstruction	31
3.5.1	Hierarchical Simplex Spline Volumes	32
3.5.2	Volume Reconstruction Problem Statement	35
3.5.3	Hierarchical Fitting	36
3.6	Experimental Results	37
3.7	Comparison with Existing Methods	38
3.8	Summary	40

Chapter 4

	Nonrigid Volume Registration with Multivariate Simplex Spline Based Free-Form Deformation	41
4.1	Introduction and Motivation	41
4.2	Previous Work	45
4.2.1	Volumetric Simplex Splines	46
4.2.2	Brain Volume Registration	46
4.3	Volumetric Simplex Splines	47
4.4	Embedding Space Initialization	48
4.4.1	Simplex Spline Initialization	49
4.4.2	Floating Volume Embedding	49
4.5	Volume Registration Problem Statement	50

4.6	Global Transformation Model	51
4.7	Local Deformation Model	51
4.7.1	Volume-Preserving Local Deformation	51
4.7.2	Normalized Mutual Information Measure	52
4.7.3	Volume-Preserving Term	53
4.7.4	Smoothness Term	55
4.8	Multiresolution Volumetric Simplex Splines	56
4.9	Experimental Results	59
4.9.1	Experiments on Simulated Brain Volumes	59
4.9.2	Comparison with Existing Algorithms	61
4.10	Comparison with Existing Methods	62
4.11	Summary	63
Chapter 5		
	Physically Based Modeling and Simulation with Dynamic Spherical Multivariate Simplex Splines	64
5.1	Introduction and Motivation	64
5.1.1	Previous Work	69
5.2	Spherical Multivariate Simplex Spline Volume	72
5.2.1	Spherical Volumetric Simplex Splines	72
5.2.2	Initial Construction of Spherical Volumetric Domain	73
5.2.3	Volumetric Parameterization	74
5.2.4	Fitting with Spherical Volumetric Simplex Splines	76
5.3	Dynamic Spherical Multivariate Simplex Splines	79
5.3.1	Geometry and Kinematics of Simplex Spline Volumes	79
5.3.2	Lagrange Equations of Motion	80
5.4	Finite Element Framework	81
5.4.1	Data Structures for Dynamic Simplex Spline Finite Elements	82

5.4.2	Calculation of Element Matrices	83
5.4.3	Discrete Dynamics Equations	84
5.5	Brain Simulation Using DSMSS Volume	86
5.5.1	Fitting Spherical Volumetric Simplex Splines to Brain Data	86
5.5.2	Brain Shifting during Surgery	87
5.5.3	Brain Injury Prediction	89
5.6	Experimental Results	91
5.7	Comparison with Existing Methods	92
5.8	Summary	93
Chapter 6		
Conclusion	99
6.1	Contributions	99
6.2	Future Work	101
Appendix	103
References	105
Abstract	118
Autobiographical Statement	119

LIST OF TABLES

Table 2.1:	Comparison between different parametric schemes in volume representation and modeling in terms of shape of the domain, topology support and high genus support.	13
Table 3.1:	Statistics of 3D reconstruction.	38
Table 3.2:	Comparison of 3D reconstruction schemes.	38
Table 4.1:	Statistics of multiresolution volumetric simplex spline domain and control space configuration.	59
Table 4.2:	Statistics of runtime comparison between the registration approaches using our multiresolution volumetric simplex spline-based free-form deformation and regular free-form deformation using tensor product B-spline scheme. Note that the degree of the domain is cubic in both cases.	62
Table 4.3:	Statistics of registration results using our MVSS-FFD method with comparison to TPBS-FFD method. The registration quality is evaluated using the normalized mutual information between the resulting floating brain volume and the reference brain volume.	62
Table 4.4:	Comparison of volume registration schemes.	62
Table 5.1:	Statistics of 3D reconstruction of brain models. The fitting error is presented by root-mean-square error.	91
Table 5.2:	Physical parameters and statistics of brain biomechanic simulations.	92
Table 5.3:	Comparison of object simulation schemes.	92

LIST OF FIGURES

Figure 2.1:	(a) Example of a more general domain Ω than the unit cube; (b) The tetrahedral partition Δ is obtained by uniformly subdividing each cube of I into 24 tetrahedra; (c) The intersections of Δ with planes parallel to the three coordinate planes are four-directional meshes which are well-known from the bivariate setting. (<i>Original image courtesy of Christian Rössl et al. at Max-Planck-Institut and Universität Mannheim.</i>)	12
Figure 3.1:	(a) A domain tetrahedron demonstrated with its knot clouds assigned and labeled. The underlying tetrahedron, $(\mathbf{p}, \mathbf{q}, \mathbf{r}, \mathbf{s})$, is rendered as a shaded tetrahedron; (b) The virtual tetrahedra of the domain tetrahedron are visualized in different colors with the opacity value of 0.4. In (a) and (b), the degree of the domain is cubic hence each vertex of the tetrahedron has three sub-knots. The primary-knots are presented with yellow dots while sub-knots are depicted with blue dots. The red lines connecting the primary-knots indicate the underlying tetrahedron. Each green line here denotes the association between primary-knot and sub-knot.	25
Figure 3.2:	(a) The Ω of a domain tetrahedron, formed by the interior of the underlying tetrahedron and virtual tetrahedra, is rendered with a blue polyhedron. The virtual tetrahedra are visualized in different colors with opacity value 0.1; (b) The virtual tetrahedra are removed to better visualize the Ω	27
Figure 3.3:	A part of a sequence of 2D images scanned from a histology sectioning profile. Histology structures gradually change from slice to slice.	29
Figure 3.4:	(a) Point set down-sampled as input of Delaunay tetrahedralization; (b) Arbitrary Delaunay tetrahedralization with convex hull as its boundary mesh; (c) Carver Algorithm removes outside tetrahedra away from volume; (d) Initial mesh after islands removal.	32
Figure 3.5:	(a) Knot insertion. After one knot is inserted at the barycenter of the original tetrahedron, the original one is subdivided into four tetrahedra; (b) Hierarchical simplices. After knots are inserted at the center of the edges of the original tetrahedron, the original one is subdivided into four tetrahedra.	34
Figure 3.6:	Illustration of hierarchical bivariate simplex splines surfaces. (a) A bivariate simplex spline surface; (b) Hierarchical structure of one domain triangle of (a); (c) Moving the free control points will not affect the continuity across the boundary; (d) Corresponding domain triangulation of (a); (e) Corresponding domain triangulation of (b); (f) Corresponding domain triangulation of (c).	35

Figure 3.7:	(a) 3D visualization of reconstructed 3D histology volume after similarity mapping; (b) 3D visualization of the corresponding μ CT volume from the same view point; (c) 3D visualization of reconstructed 3D histology volume after global faring; (d) 3D visualization of corresponding μ CT volume from the same view point.	39
Figure 4.1:	Illustration of the pipeline of our nonrigid registration framework. The rectangles inside the pipeline indicate tasks, and the icons with text under them denote the inputs and outputs of tasks. The text boxes inside the task denote the cost functions which fulfill the task.	45
Figure 4.2:	(a) A cubic volumetric simplex spline domain with knots associated; (b) The control solid defined over (a). The tetrahedra of the control solid are scaled in order to emphasize its non-empty solid interior geometry.	48
Figure 4.3:	(a) The relationship among the control net, the control space and the embedded objects. The dotted line of the blue rectangle denotes the boundary of a control net, the green rounded-corner rectangle denotes the control space with three yellow objects embedded; (b) The embedding space with the floating brain volume embedded. In the figure, the blue tetrahedra mesh denotes the control net while the green dots denote the control points. . . .	50
Figure 4.4:	(a) Multiresolution tensor product B-splines. While increasing the resolution of region of interest, other regions are affected because of its tensor product nature; (b) Multiresolution simplices. True local support can be steadily achieved because of its non-tensor product nature.	56
Figure 4.5:	(a) Knot insertion. After one knot is inserted at the barycenter of the original tetrahedron, the original one is subdivided into four tetrahedra; (b) Multiresolution simplices. After knots are inserted at the center of the edges of the original tetrahedron, the original one is subdivided into eight tetrahedra.	58
Figure 4.6:	One case study. (a) The reference brain volume; (b) The floating volume to be registered to (a); (c) The registered volume using our MVSS-FFD method; (d) The image difference between (a) and (c); (e) The control space before registration; (f) The control space after registration; (g) The registered volume using existing TPBS-FFD method; (h) The image difference between (a) and (g).	60
Figure 4.7:	Another case study. (a) The reference brain volume; (b) The floating volume to be registered to (a); (c) The registered volume using our MVSS-FFD method; (d) The image difference between (a) and (c); (e) The control space before registration; (f) The control space after registration; (g) The registered volume using existing TPBS-FFD method; (h) The image difference between (a) and (g).	61

Figure 5.1:	Illustration of the pipeline of our DSVSS framework. The rectangles inside the pipeline indicate tasks, and the icons with text under them denote the inputs and outputs of tasks.	68
Figure 5.2:	(a) The spherical domain with assigned knot clouds for defining spherical volumetric simplex splines. The yellow and blue dots denote primary-knots and sub-knots, respectively; (b) The spherical simplex spline volume defined upon the domain in (a). The green dots denote the control points. The evaluated spherical volume simplex volume is scaled to show its non-empty interior property.	73
Figure 5.3:	(a) A regular icosahedron, which is the best approximation of a solid sphere among all regular polyhedra; (b) Tetrahedralization of (a) is uniform and it is easy to implement; (c) Harmonic mapping from (b) to a unit solid sphere yields the domain tetrahedralization, consisting of uniform and well-shaped tetrahedra; (d) A domain with cubic knot clouds assigned to (c); (e) A close view of the domain picked from (d).	75
Figure 5.4:	(a) The discretized point set in the spherical domain space; (b) The discretized data point set in the physical space, from the same angle of view as (a); (c-f) The shapes are cut into halves sagittally (c-d) and axially (e-f) in order to show the interior mapping between the parametric domain and the physical object.	94
Figure 5.5:	Modeling discontinuities with separated domain triangles. Even though A and A' are co-located, and B and B' are co-located, the domain triangles in red and green are belonged to two different domains.	95
Figure 5.6:	(a) An axial view of a slice high-resolution brain SPGR MRI dataset; (b) Volume visualization of the reconstructed DSVSS volume; (c) The volume is split to show its reconstructed interior intensities.	95
Figure 5.7:	(a) One slice view of IMRI image; (b) The reconstructed DSVSS volume, where the cross-sectional view displays the DSVSS-captured image intensities reconstructed from the pre-operative high-resolution SPGR images; (c) The brain deformation simulated using our system, where the cross-sectional view is captured, from the same view angle as (b), to show the displacement from (b), and the green contour indicates the extent of displacement at the boundary. In (b) and (c) the red arrow denotes the orientation of gravity, and its position denotes the resected skull.	96

Figure 5.8:	(a) The color map used to describe the deformation scale. The red arrow on the ISO-surface indicates the position where skull is resected; (b-h) Brain shifting simulation with a time interval of 75ms; (i-j) To better visualize the deformation, cross-section views of the first key frame (b) and last one (h) are retrieved. Deformed junction between the two hemispheres indicates the global brain shifting.	96
Figure 5.9:	(a) The color map used to describe the stress field. The red arrow on the ISO-surface indicates the position where a blunt impact occurs; (b-j) Brain injury simulation with a time interval of 3ms. The blunt impact occurs at the front lobe. Simulation results indicate that in addition to the spot directly under the impact, there are some other positions where bleeding may happen.	97
Figure 5.10:	Comparison of stress evolutions of the right thalamus under a blunt impact. The green one is the simulation curve obtained from the real biomechanic experiments and the red one is the result simulated using our framework. . .	97
Figure 5.11:	(a-f) Another brain injury simulation with a time interval of 3ms. The blunt impact occurs at the left front lobe; (g) Comparison of stress evolutions of the right thalamus under the blunt impact.	98

CHAPTER 1:

INTRODUCTION

Volume representation and modeling of heterogeneous objects acquired from real-world are very challenging research tasks and have many potential applications, e.g., volume reconstruction, volume simulation and volume registration. The fundamental objectives are to unambiguously model high-dimensional heterogeneous objects, accurately and effectively simulate their behaviors, and rigorously analyze their geometry and physical natures. With ever-improved computing power and more state-of-the-art data acquisition technologies, volume representation and modeling become increasingly important in many research and academic realms since they play the role of foundation for any other further processes, such as analysis, visualization, and simulation, just to name a few.

1.1 Motivation

Researchers and professionals dedicated to those volume representation and modeling related domains are usually confronted with two inevitable difficulties.

The first difficulty is, it is usually difficult to choose one appropriate and efficient volume representation approach. The representations prevalently used nowadays are oftentimes discrete in nature, e.g., voxel-based regular grids and unstructured point samples [56, 57]. Geometry of an underlying volume is implicitly defined in the scalar field. Historically, volumetric primitives have been based on uniform or rectilinear grid, where the data is often regularly spaced along grid lines. In the past few years, an unstructured volume representation has started to emerge as a viable modeling tool, where a tetrahedral mesh is exploited to dictate the domain of a volume [9, 97, 8, 74]. This type of representation is expected to be more and more popular as the irregular, adaptive 3D scanning technologies becomes commonplace. However, from a pure visualizations point of view, tetrahedra are mainly exploited as rendering primitives, i.e., they serve as a good discrete representation for visualization. This kind of tetrahedral mesh representation is only C^0 continuous. It is less suitable for modeling contin-

uously varying material attributes without resorting to approximation. To satisfy the modeling requirement of high-order continuity, volumetric modeling based on splines such as B-splines or NURBS [67, 27, 78, 41] appears to be more appropriate. Nonetheless, modeling with B-splines or NURBS has severe shortcomings. Its modeling scope is extremely constrained in term of geometric, topological, and attribute aspects. First, B-spline and NURBS are defined over a regular, tensor-product domain. A single B-spline or NURBS can not represent volumes of arbitrary topology without patching or trimming operations. Furthermore, patching multiple B-splines or NURBS to form arbitrary topology is not easy to control at all. Second, tensor-product splines are essentially smooth everywhere. It is difficult to model high-frequency features. Third, when refining a region of interest in a tensor-product spline patch, it will introduce too many extra degrees of freedom in other less-interesting regions nearby in order to retain its regular structure. Attractive properties such as local adaptivity and multiresolution are rather difficult to achieve. In a nutshell, researchers usually are unwillingly forced to choose one inadequate volume representation scheme from those discrete or continuous approaches.

The second difficulty is, it is often difficult to choose one accurate and adequate volume representation scheme. Among many important aspects of volume representation and modeling, the accuracy is of utmost importance since only an accurate volume representation can be used to provide valuable information for the model-based assessment. However, in existing approaches, several different representations are typically required throughout the representation and modeling of real-world models in computerized environments. That is to say, each stage within the entire representation and modeling pipeline, including modeling such as meshing and material modeling, simulation, analysis, visualization, typically takes as input a different representation of the modeled object, which requires costly and error-prone data conversions throughout the entire modeling process. It will certainly introduce error into the pipeline. For instance, in order to simulate the brain deformation, a linear solid mesh needs to be generated for finite element methods (FEMs) from the voxel-based representation of the brain represent-

ing the geometry of the brain, which has a highly convoluted cortical surface and many subtle sub-cortical structures. Then, manual material editing needs to be conducted to assign material properties to solid meshes. The FEM properties are linearly interpolated during simulation and resampled once again to voxels' intensities for visualization. Certainly, conversions among volumetric datasets, solid meshes, finite elements, and voxels based on linear interpolation or resampling will introduce error. In addition, more errors will be brought into the pipeline as the constructed linear solid mesh may not well represent both geometry and material distribution simultaneously. The geometric, physical, and mechanical properties are not tightly integrated into the simulation. As a result, the current practice impedes the accurate modeling and simulation of digital models of real-world objects. With ever-improving computing power comes the strong demand for more accurate, robust, and powerful solid modeling and simulation paradigms that are efficacious for the modeling, simulation, analysis, and visualization of digital models of real-world objects.

In order to bridge the gap and overcome the aforementioned deficiencies, in this dissertation, we propose an integrated computational framework based on dynamic multivariate simplex splines (DMSS) that can greatly improve the accuracy and efficacy of modeling and simulation of heterogeneous objects since the framework can not only reconstruct with high accuracy geometric, material, and other quantities associated with heterogeneous real-world models, but also simulate the complicated dynamics precisely by tightly coupling these physical properties into simulation. The integration of geometric modeling and material modeling is the key to the success of representation of real-world objects.

In sharp contrast to existing techniques, our framework uses a single representation that requires no data conversion. The advantages of our framework result from many attractive properties of multivariate splines. In comparison with tensor-product B-splines or NURBS, multivariate simplex splines are non-tensor-product in nature. They are essentially piecewise polynomials of the lowest possible degree and the highest possible continuity everywhere across

their entire tetrahedral domain. For example, given an object of simplex splines with degree n , it can achieve C^{n-1} continuity. Furthermore, C^0 , other varying continuities, and even discontinuity can be accommodated through different knot and control point placements and/or different arrangements of domain tetrahedra in 3D. Furthermore, simplex splines are ideal to represent heterogeneous material distributions through the tight coupling of control points and their attributes. From dynamic simulation’s point of view, they are finite elements which can be directly brought into finite element formulations and physics-based analysis without losing any information. Finite elements can be derived directly from the simplex spline representation, which can also be visualized via volumetric ray-casting without discretization [25]. Trivariate simplex splines are obtained through the projection of n -dimensional simplices onto 3D. Projecting them one step further onto 2D for visualization results in bivariate simplex splines of one degree higher than the original solid model, therefore, simplex splines facilitate the visualization task with an analytical, closed-form formulation. It is not necessary to perform any resampling and/or interpolation operations. Local adaptivity and local/global subdivision via knot insertion can be readily achieved.

The novelties of this framework can be summarized as follows:

- **Unification.** We develop an integrated volume representation and modeling framework which seamlessly integrates geometric properties, physical properties, and dynamic behaviors of real-world objects together. The consistent, unified representation throughout each stage of modeling is a single degree n dynamic multivariate simplex spline. Hence in downstream processes such as analysis, visualization, and simulation, it is unnecessary to resorting to other representation approaches.
- **Accuracy.** The heterogenous model reconstructed from the digitalization of a real-world object is faithful and of high-fidelity in terms of its geometry and material distribution. The model reconstruction procedure is automatic, and the maximal fitting error to the original data can be controlled by user’s specification interactively.

- **Efficiency.** The proposed volume representation and modeling framework can achieve a faster performance than other B-spline based approaches in terms of assessment. This mainly attributes to the non-tensor-product property of multivariate simplex splines. Hierarchical continuous simplices greatly improve the evaluation of the heterogeneous model without introducing extra unnecessary complexity into the framework.
- **Flexibility.** The framework is capable of representing heterogeneous objects in real world of complex geometry and arbitrary topology. since its domain is intrinsically arbitrary tetrahedralization, the framework can represent and model high genus real-world objects naturally, without complicated trimming and patch operation. With the shared and/or non-shared control points assignments and different domain tetrahedra placements, we can also obtain continuous object representation as well as discontinuity without extra work flexibly.
- **Robustness.** Our volume representation and modeling paradigm is naturally a robust analytic approach with closed-form formulation. The geometry and physical properties of the volumetric model can be computed using the analytic representation without any need for numerical approximations such as cubic interpolation or quadratic resampling. Hence, physical simulation, including all downstream processes, such as analysis and evaluation, can be achieved more accurately and robustly.
- **Versatility.** We successfully apply the dynamic multivariate simplex splines (DMSS) scheme in several challenging volume related research topics such as volume reconstruction, nonrigid volume registration and physically based volume modeling and simulation. Preliminary experimental results demonstrate that our DMSS based framework has great potentiality to provide a versatile solution for volume representation and modeling.

1.2 Contributions

We have systematically developed the proposed framework based on dynamic multivariate simplex splines (DMSS) for volume representation and modeling of heterogeneous objects acquired from real-world. Based on this integrated framework, my research work has been fruitful in my Ph.D. study with important contributions to both academia and medical domain in the following problems:

- Reconstruction and Visualization of Medical Volume (*Chapter 3*)** The histopathological study of tissue is an important tool in the medical field for the prognosis of disease. Although informative in itself, histological slices are traditionally viewed under optical microscope to reveal only a 2D image. Hence medical professionals inevitably have an increasing demand of exploring the 3D structure of the tissue. Therefore we presented an effective framework for the reconstruction and visualization of volumetric data from a sequence of 2D images using multivariate simplex spline as its volume representation approach. The 2D images are first aligned to generate an initial 3D volume, followed by the creation of the tetrahedral domain. Then a solid model is reconstructed using multivariate simplex splines with fitting and fairing procedures. The reconstructed heterogeneous volumetric model can be quantitatively analyzed and easily visualized. We conduct extensive experiments using histology samples, and our empirical results demonstrate that the proposed paradigm significantly augments the current techniques within the medical, modeling, and visualization communities. Although we focus mainly on the volumetric reconstruction of 3D histology for the biomedical domain, the applications of our technique is diverse, including material editing and reconstruction, volume simplification, data exploration and visualization in geological fields, and so on. Novel techniques and algorithms proposed in this project can be applied to reconstruct heterogeneous solid model with complex geometry and topology from other visual data. This part of work has been published in the conference proceedings of *Com-*

puter Graphics International, 2007, then it was invited to *The Visual Computer*, which is one of the most prestigious computer science journals specialized in visualization.

- **Registration and Visualization of Nonrigid Volume (Chapter 4)**

Non-rigid registration of intermodality and intramodality images is playing an increasingly important role both in medical and research realms for the reason many medical activities often rely on the complementary information retrieved from different images, which are usually obtained from intermodality or intramodality. Existing volume registration algorithms using free-form deformation scheme based on tensor product B-spline volumes, although well established, have severe drawbacks such as expensive computational demand, topological limitation of the model, awkward multiresolution support, etc. Instead, we propose a novel nonrigid volume registration framework using multiresolution volumetric simplex spline based free-form deformation to achieve more efficiency, flexibility, and accuracy. With the native non-tensor product property of simplex spline and its true multiresolution support, the computational cost of our framework was reduced to one third that of tensor product B-spline volume scheme. By applying multiresolution volumetric simplex spline as the volume representation scheme, other downstream applications can be easily and steadily achieved, such as medical volume visualization, lesion repositioning, correlation analysis, etc. We have successfully applied the framework to the registration of magnetic resonance imaging brain volumes and the preliminary experimental results demonstrate the powerful potentiality of our framework being employed to register volumes acquired from intermodality and intramodality imaging systems in other biomedical applications. This part of work has been submitted to *SPM 2010: ACM Solid and Physical Modeling Symposium* and now it is under the first round review.

- **Physically Based Modeling, Simulation and Visualization (Chapter 5)**

For a long time, researchers dedicated into realms of physically based modeling and simulation have been eagerly awaiting an integrated volume representation of geometric

and material properties. The representations prevalently used nowadays are oftentimes discrete in nature, although ideal for visualization, it is less suitable for modeling continuously varying material attributes without resorting to approximation. Although tensor product B-spline based representations can achieve the continuities of the model to some extent, they have severe drawbacks in high genus support. Existing modeling and simulation approaches, several different representations are typically required throughout the representation and modeling of real-world models in computerized environments. Hence we proposed integrated computational framework based on dynamic multivariate simplex splines that can greatly improve the accuracy and efficacy of modeling and simulation of heterogeneous objects. The proposed framework can not only reconstruct with high accuracy geometric, material, and other quantities associated with heterogeneous real-world models, but also simulate the complicated dynamics precisely by tightly coupling these physical properties into simulation. We have successfully applied the framework for biomechanic simulation of brain deformations, such as brain shifting during the surgery and brain injury under blunt impact. The evaluations demonstrate the excellent performance of our new technique. This part of work has been published in the conference proceedings of *ACM Solid and Physical Modeling Symposium, 2008*, then it was invited to *Computer-Aided Design*, which is one of the most prestigious computer science journals specialized in the realm of CAD.

1.3 Dissertation Organization

The dissertation is organized in the following way. *Chapter 2* briefly reviews the theoretical background of dynamic multivariate simplex splines and the volume related research topics such as volume reconstruction, nonrigid volume registration, and physically based volume modeling and simulation. *Chapter 3* presents an effective paradigm for reconstruction of volumetric data from a sequence of 2D images using our DMSS framework. An efficient computational algorithm for nonrigid volume registration using multivariate simplex spline based

free-form deformation will be presented in *Chapter 4*. *Chapter 5* further introduces our DMSS framework into the physically based modeling and simulation area and employ the framework to model and simulate the biomedical behaviors of human brain. Finally, *Chapter 6* summarizes the presented framework and points towards the future work along this research direction.

CHAPTER 2: BACKGROUND

My dissertation research work, DMSS, is based on previous work in volume representation and modeling. In this section we review the prior work done in these related research fields. Note that there are a lot of schemes of volume representation and modeling and we only review the commonly-used ones of them in the interest of space. This chapter is organized as follows. *Chapter 2.1* reviews volume representation schemes, including parametric ones and nonparametric ones. A brief comparison of these approaches will be presented at the end of this chapter. *Chapter 2.2* and *Chapter 2.3* review representative solid volume modeling approaches and physically based modeling approaches, respectively.

2.1 Volume Representation Approaches

There are many other volume representation approaches. Among them, we only survey two widely-employed parametric representatives, tensor product B-spline and quadratic super spline.

2.1.1 Parametric Volume Representation Approaches

Tensor Product B-spline Volumes

Analogous to tensor product B-spline surfaces, we can use tensor product uniform trivariate B-spline functions for the object representation. Like all tensor product B-spline functions, these trivariate functions have a control-volume that consists of scalar coefficients, $P_{ijk} \in R$. These trivariate functions are of the form:

$$q(u, v, w) = \sum_{i=0}^{i-1} \sum_{j=0}^{m-1} \sum_{k=0}^{n-1} P_{ijk} B_i(u) B_j(v) B_k(w), \quad (2.1)$$

where $B_i(u)$, $B_j(v)$ and $B_k(w)$ are the uniform B-spline basis functions, P_{ijk} are the scalar coefficients in a volumetric mesh of size $l \times m \times n$, and $q(u, v, w)$ is a scalar function.

Although intuitive and concise, tensor product B-spline can only represent G^0 solid model

which greatly confines its application. To extend its application, Raviv and Elber [67] presented a three dimensional interactive sculpting paradigm that employed a collection of scalar uniform trivariate B-spline functions.

Quadratic Super Spline Volumes

Rössl *et al.* [71, 72, 73] presented quadratic super splines to reconstruct solid models from structure-gridded volume samples.

The splines they developed, are piecewise polynomials of lowest possible total degree, where the polynomial pieces have the form $\sum_{i+j+k \leq 2} a_{i,j,k} x^i y^j z^k$, where $a_{i,j,k} \in \mathbb{R}$, $i+j+k \leq 2$. Thus the total degree is 2.

Let \diamond be a uniform cube partition of the cubic domain $\Omega = [0, n]^3 \subseteq \mathbb{R}^3$, where every cube $Q \in \diamond$ has edge length 1. A more general domain can be achieved by trimming and patching the domain, shown in *Figure 2.1-(a)*. They divided each of the n^3 cubes Q into six Egyptian pyramids by connecting its center point v_Q with the four vertices of every face of Q . Then, they inserted both diagonals into these six faces of Q and connect their intersection points with v_Q . This subdivides each of the six pyramids in Q into four tetrahedra, forming a natural, uniform tetrahedral partition Δ of Q , where every cube $Q \in \diamond$ contains 24 congruent tetrahedra. *Figure 2.1-(b)* illustrates the construction of Δ . The partition Δ is a generalization of the four-directional mesh which is well-known in the bivariate setting [55, 53, 52]. The relation to the bivariate setting is shown in *Figure 2.1-(c)*. Then they constructed consistent splines which satisfy many smoothness conditions, and such splines are called “Super Splines”.

The space of quadratic super splines with respect to I is defined by

$$S_2(\Delta) = \{s \in C(\Omega) : s|_{T \in P_2}, T \in \Delta, \quad (2.2)$$

and s is smooth at v , for all v vertices of \diamond , where $P_2 = \text{span}\{x^i y^j z^k : i, j, k \geq 0, i+j+k \leq 2\}$ denotes the ten dimensional space of quadratic polynomials, i.e., the space of trivariate polynomials of total degree two. In their approximation method, they employed quasi-interpolating

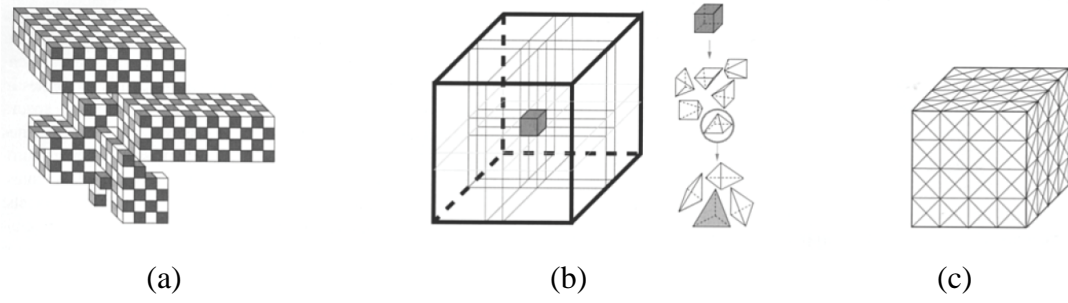


Figure 2.1: (a) Example of a more general domain Ω than the unit cube; (b) The tetrahedral partition Δ is obtained by uniformly subdividing each cube of I into 24 tetrahedra; (c) The intersections of Δ with planes parallel to the three coordinate planes are four-directional meshes which are well-known from the bivariate setting. (Original image courtesy of Christian Rössl et al. at Max-Planck-Institut and Universität Mannheim.)

splines from $S_2(\Delta)$ which posses many additional natural smoothness properties. Mathematically speaking, this means that they deal with appropriate subspaces of $S_2(\Delta)$ where the number of free parameters is considerably lower.

In essence, a spline $s \in S_2(\Delta)$ can be written in its piecewise Bernstein-Bézier form [60, 61, 52, 51].

2.1.2 Nonparametric Volume Representation Approaches

In general, surfaces expressed by an implicit form can be formulated as: $(x, y, z) | F(x, y, z) = c$. The function F is called the implicit function, which defines the scalar field or the density field. an implicit solid is the collection of all the level-sets whose return values are greater, or smaller, than a given threshold. Formally it can be defined as:

$$\begin{cases} w = F(x, y, z) \\ w > w_0. \end{cases} \quad (2.3)$$

Although the basic idea is intuitive, the point lies in how to choose the implicit function. In Hua and Qin [27, 28, 29], they collected different B-spline patches defined over the 3D working space to form a volumetric implicit function that can be collectively used to represent objects of complicated geometry and arbitrary topology. Their solution was significantly

different from frequently used parametric B-splines. In their environment, they enhanced the scalar B-spline representation power by incorporating the modeling advantages from hierarchical splines, generalized CSG-based boolean operations, and nonuniform knot insertion. They took N B-spline patches in the sculpting space into consideration, which are located at any location and with any orientation. In general, these patches may be formulated by different numbers of control coefficients in order to achieve the goal of multi-resolution analysis and other operations. Consequently, the density value at the location (x, y, z) can be computed as:

$$F(x, y, z) = \sum_{i=1}^N s_i(T_i(x, y, z)), \quad (2.4)$$

where T_i is an affine transformation from the Euclidian space to the parametric domain of patch s_i . Since the B-spline has the property of affine invariance, this transformation can be easily calculated. For each different patch s_i , there is a corresponding transformation T_i . Hence, $F(x, y, z)$ becomes a new volumetric implicit function defined over the 3D working space. In essence, *Equation 2.4* is a hierarchical organization of the N patches.

2.1.3 Comparison between Volume Representation Schemes

Method	Domain	Topology	High Genus Support
Tensor Product B-Splines	Uniform Cube-shaped Grid	G^0	Trimming and Patching
Quadratic Super Splines	Uniform Tetrahedralization	G^0	Trimming and Patching
Implicit Functions	No	Any	Not Necessary

Table 2.1: Comparison between different parametric schemes in volume representation and modeling in terms of shape of the domain, topology support and high genus support.

The domain of tensor product B-spline volumes is a uniform cube and the domain of quadratic super spline volumes is a tetrahedralized cube, respectively. This confines the solid volume represented are G^0 . The continuity of these two models are the corresponding degree of the spline function. The degree of tensor product B-spline volume is the highest degree of the three dimensions of the cube. For example, in *Equation 2.1*, the continuity is

$\alpha = \max\{l - 1, m - 1, n - 1\}$. So the volume is C^α . Intuitively, the quadratic super spline volume is C^1 continuous everywhere.

To model high genus volume, designer should do trimming and patching to the tensor product B-spline volumes. Blending function should also be carefully chosen to guarantee cross-boundary continuity. Quadratic super spline may represent high genus volumes, if a more general tetrahedra domain is presented, as shown in *Figure 2.1-(a)*.

Non-parametric volume's continuity is mainly confined by the degree of its implicit function representation. For instance, In Hua and Qin's work [29], the versatility of their dynamic implicit modeling enables the user to easily modify both the geometry and the topology of modeled objects.

2.2 Solid Modeling Approaches

Based on specific geometric representations, modeling techniques are employed to create shapes from those representations. Since this dissertation research is centered on solid objects, we mainly review solid modeling techniques. Generally, solid modeling involves the creation and manipulation of complete, unambiguous mathematical representations of 3D objects. Traditional solid presentations fall into one of three fundamentally distinct categories: boundary schemes, decomposition schemes, and constructive solid geometry.

2.2.1 Boundary Schemes

In a boundary representation (B-rep) scheme [3], objects are modeled as unions of their boundaries or enclosing surfaces. The modeling power of B-reps depends on the allowed classes of surfaces which may include planar polygons, quadrics, spline surfaces, and surface patches. In most cases, the surfaces are limited to polynomials of small degree, and ensuring geometric continuity of patched surfaces is difficult, if not impossible. Additionally, topological information consisting of connectivity relationships between geometric entities must be provided to fully represent a solid. A variety of schemes have been proposed for representing topological information, but maintaining a formally valid B-rep is inevitably a tedious process.

2.2.2 Decomposition Schemes

Decomposition schemes have three general forms: spatial enumeration, cell decomposition, and octree encoding. Spatial enumeration is perhaps the oldest and most direct approach to solid modeling. The “world” is composed of a three dimensional grid of cuboids and an object is represented as the union of cells which contain part of the object. Correct object representations are easy to maintain but difficult to create due to the simplistic structure. Cell decomposition [43], typically employed for finite element mesh generation, is a generalization of spatial enumeration in which objects are represented as the union of simple primitives which are not required to have the same size or shape. The octree method is similar to both spatial enumeration and cell decomposition in that objects are modeled as a collection of fundamental primitive solids or cells. However, the representation is made more efficient by organizing the cells in an eight-ary tree. Cells which are partially full can then be subdivided, but the required storage increases exponentially as the tree depths increase.

2.2.3 Constructive Solid Geometry

Constructive solid geometry (CSG) has its origins in the work of Rvachev [77, 81], and Voelcker and Requicha [68]. Objects are organized as a collection of primitive solids, which are leaves of a tree whose nodes correspond to Boolean operators that perform unions, intersections and differences. The number and types of allowed primitives control the scope of the representation. Topology is stored both implicitly (in the tree structure and set operators) and explicitly (in the primitive objects), and formally valid object representations are easily maintained. CSG is appealing due to its intuitive formulation which is directly analogous to physical manufacturing processes where complicated solids are created by “cutting and pasting” together primitive solids. Although we categorize solid modeling techniques into three fundamentally distinct categories, the currently-used solid modeling techniques oftentimes combine two or three of them together in order to enhance the modeling capability. Also, there are some invariants of these three techniques. Note that these solid modeling techniques can be used on

the aforementioned geometric representations.

2.3 Physically Based Modeling Approaches

In recent years, physics-based modeling has emerged as an important approach in computer graphics. Generally, physics-based modeling techniques augment geometric objects with physical attributes such as mass, damping and stiffness distributions. Physics-based models are governed by the mechanical laws of continuous bodies, which can be expressed in the form of dynamic differential equations. The dynamic and realistic behaviors can be obtained by solving an associated motion equation numerically.

2.3.1 Deformable Models

Free-form deformable models were first introduced to computer graphics by Terzopoulos *et al.* [92]. They employed elasticity theory to construct differential equations that model the behavior of non-rigid curves, surfaces, and solids as a function of time. Elastically deformable models respond in a natural way to applied forces, constraints, ambient media, and impenetrable obstacles. The equations governing a deformable model's motion can be written in Lagrange's form as follows:

$$\frac{\partial}{\partial t}(\mu \frac{\partial \mathbf{r}}{\partial t}) + \gamma \frac{\partial \mathbf{r}}{\partial t} + \frac{\delta \varepsilon(\mathbf{r})}{\delta \mathbf{r}} = \mathbf{f}(\mathbf{r}, t), \quad (2.5)$$

where $\mathbf{r}(\mathbf{a}, t)$ is the position of the particle \mathbf{a} at time t , $\mu(\mathbf{a})$ is the mass density of the body at \mathbf{a} , $\gamma(\mathbf{a})$ is the damping density, and $\mathbf{f}(\mathbf{r}, t)$ represents the externally applied forces. $\varepsilon(\mathbf{r})$ is a functional which measures the net instantaneous potential energy of the elastic deformation of the body.

The external forces are balanced against the force terms on the left hand side of Equation 2.5 due to the deformable model. The first term is the internal force due to the model's distributed mass. The second term is the damping force due to dissipation. The third term is the elastic force due to the deformation of the model away from its natural shape. Then, the poten-

tial energy of deformation for elastic models can be used as the measure of the deformation. By applying the external forces to the elastic models, we can achieve realistic dynamics.

To solve *Equation 2.5* with a computer, the continuous dynamic model may be discretized as follows:

$$\mathbf{M}\ddot{\mathbf{c}} + \mathbf{D}\dot{\mathbf{c}} + \mathbf{K}\mathbf{c} = \mathbf{f}, \quad (2.6)$$

where \mathbf{c} is the position vector of the collection of sample points on the discretized mesh, \mathbf{M} is a mass matrix, \mathbf{D} is a damping matrix, \mathbf{K} is a stiffness matrix, and the force at every mass-point in the mesh is the sum of all possible external forces: $\mathbf{f} = \sum \mathbf{f}_{ext}$. The deformable model then can be computed by numerical approaches such as the finite-difference method or the finite-element method. Later on, deformable models were further developed by Pentland and Williams [58], and Metaxas and Terzopoulos [44]. Gibson and Mirtich [19] gave a good survey on deformable models in computer graphics. More recently, James and Pai [30] presented an algorithm for fast, physically accurate simulation of deformable objects suitable for real time animation and virtual environment interaction. Pai [54] also presented Cosserat-type physical models for interactive simulation of thin elastic solids, which are visually well approximated as smooth curves, and yet possess essential physical behaviors characteristic of solid objects.

2.3.2 Physics-based Geometric Design

Physical simulation can be used as an effective, interactive tool for building and manipulating a wide range of models. It supports the dynamic manipulation of complex physical models. However, less effort has been applied to free-form dynamic interaction between designers and individual manufactured objects, which is especially useful for geometric design. Physics-based geometric design allows designers to directly manipulate and interactively sculpt shapes using a variety of force-based tools. It affords designers a natural and intuitive interaction with geometric objects. It appeals to a spectrum of users ranging from highly-trained engineers, computer professionals and artists, to even naive users with little computer skill.

Qin and Terzopoulos [66, 65, 93] developed D-NURBS by marrying advanced geometric

modeling with computational physics, which is an extension to traditional NURBS that permits more natural control of the surface geometry. In order to assign physical properties to the surface, they augment the geometric formulation with time information:

$$s(u, v, t) = \frac{\sum_{i=0}^m \sum_{j=0}^n w_{i,j}(t) \mathbf{p}_{i,j}(t) N_{i,k}(u) N_{j,l}(v)}{\sum_{i=0}^m \sum_{j=0}^n w_{i,j}(t) N_{i,k}(u) N_{j,l}(v)}, \quad (2.7)$$

where the control points $\mathbf{p}_{ij}(t)$ and weights $w_{ij}(t)$ are functions of time, comprising the D-NURBS generalized coordinates. Therefore, the velocity of the surface as well as the surface can be formulated by

$$\dot{s}(u, v, \mathbf{p}) = \mathbf{J} \dot{\mathbf{p}}, s(u, v, \mathbf{p}) = \mathbf{J} \mathbf{p}, \quad (2.8)$$

where $\mathbf{J}(u, v, \mathbf{p})$ is the Jacobian matrix of D-NURBS surface with respect to generalized coordinates \mathbf{p} . The equations of motion of the D-NURBS model are derived by applying the Lagrangian dynamics and numerically solved by the finite element method.

Although D-NURBS is a powerful physics-based geometric design framework, the NURBS-based dynamic model cannot represent objects of arbitrary topology. Therefore, Qin *et al.* [63] introduced a dynamic Catmull-Clark subdivision model in 1998. Mandal and Qin [40] further generalized this model to any subdivision scheme. Later, McDonnell and Qin [42] extended the dynamic subdivision techniques to solids, which makes the dynamic framework of subdivision models even more powerful for shape design and manipulation.

2.3.3 Geometric Modeling with Particle Systems

Particle systems consist of a large number of particles moving under the influence of external forces such as gravity, vortex fields, and collisions with stationary obstacles. Particles are objects that have mass, position, velocity, acceleration, and other attributes. Particles can be made to exhibit a wide range of interesting behavior such as join, split, or stretch operations, or simulate natural phenomena. There are mainly two types of particle systems: interacting and

non-interacting particle systems. For modeling with interacting particle systems, ideas from molecular dynamics have been used to develop models of deformable materials using collections of interacting particles. In these models, long-range attraction forces and short-range repulsion forces control the dynamics of the system. Typically, these forces are derived from an intermolecular potential function such as the Lennard-Jones function,

$$\phi_{LJ}(r) = \frac{B}{r^n} - \frac{A}{r^m}. \quad (2.9)$$

The force \mathbf{f}_{ij} attracting a particle to its neighbor is computed from the derivative of the potential function $\mathbf{f}_{ij} = -\nabla_r \phi_{LJ}(\|\mathbf{r}_{ij}\|)$, where $\mathbf{r}_{ij} = \mathbf{p}_j - \mathbf{p}_i$ is the vector distance between particles i and j . Particle systems whose dynamics are governed by potential functions and damping will evolve towards lower energy states. In 3D the particles will arrange themselves into hexagonally ordered layers. They are naturally used to model solid objects via applied external forces [96].

However, it is rather hard to model surfaces with particle systems, since, in the absence of external forces and constraints, 3D particle systems prefer to arrange themselves into solids rather than surfaces. Szeliski and Tonnesen [86] introduced oriented particle systems. They added an orientation to each particle's state and devised new interaction potentials for the oriented particles which favor locally planar or spherical arrangements. Therefore, oriented particle systems can be used to model more flexible surfaces.

CHAPTER 3: VOLUME RECONSTRUCTION WITH MULTIVARIATE SIMPLEX SPLINES

This chapter presents an effective framework for the reconstruction of volumetric data from a sequence of 2D images using proposed multivariate simplex spline as its volume representation approach. The 2D images are first aligned to generate an initial 3D volume, followed by the creation of a tetrahedral domain using the Carver algorithm. The resulting tetrahedralization preserves both geometry and topology of the original dataset. Then a solid model is reconstructed using simplex splines with fitting and faring procedures. The reconstructed heterogenous volumetric model can be quantitatively analyzed and easily visualized. Our experiments demonstrated that our approach can achieve high accuracy in the data reconstruction. Novel techniques and algorithms proposed in this chapter can be applied to reconstruct heterogeneous solid model with complex geometry and topology from other visual data.

3.1 Introduction and Motivation

In the past few years, an unstructured volume representation has started to emerge as a viable modeling tool, where a tetrahedral mesh is exploited to dictate the domain of a volume [9, 97, 8, 74]. This type of representation is expected to become increasingly popular as modeling and visualization of geometric structures plus physical attributes of heterogeneous objects become commonplace. To satisfy the modeling requirement of high-order continuity in heterogeneous objects, volumetric modeling based on splines, such as B-splines or NURBS [67, 78, 41, 28, 29], appear to be more appropriate. Nonetheless, modeling with B-splines or NURBS has serious limitation. Its modeling scope is extremely constrained in term of geometric, topological, and attribute aspects.

We aim to design a representation with flexible, hierarchical continuous simplices. In order to reconstruct a heterogenous model of high accuracy, a unified volume modeling and reconstruction based on hierarchical trivariate DMS-splines is proposed in this chapter. Our method

has the following advantages:

- It explores the intrinsic image features of a histology section, making it a fully automatic procedure without human intervention during the reconstruction.
- Our model makes use of a more general and flexible tetrahedral domain, laying a foundation for both visualization and modeling tasks. The unstructured volume being modeled can be of complicated geometry and arbitrary topology.
- The trivariate DMS-spline based representation offers a single, compact analytical representation, because it is a piecewise polynomial of the lowest possible degree and the highest possible continuity across the entire tetrahedral domain.
- This trivariate DMS-spline based representation can also enable the strong multiresolution modeling capability through interactively subdividing any region of interest, allocating more knots and control points accordingly. The volume can be represented at desired resolution by extracting specific layers from the hierarchical simplices.
- Our method can adaptively refine the domain tetrahedra with hierarchical simplices, which introduces more degrees of freedom, leading to better fitting results.

We conduct extensive experiments using histology samples, and our empirical results demonstrate that the proposed paradigm significantly augments the current techniques within the medical, modeling, and visualization communities. Although we focus mainly on the volumetric reconstruction of 3D histology image sequence for the biomedical domain, the applications of our technique is diverse, including material editing and reconstruction, volume simplification, data exploration and visualization in geological fields, and so on.

The chapter is organized in the following way. *Chapter 3.2* enumerates several milestones achieved by pioneers dedicated to this area. *Chapter 3.3* contains the condensed theoretical principal of multivariate simplex splines. *Chapter 3.4* illustrates the tetrahedral domain extraction procedure which creates tetrahedral mesh for further use in modeling and reconstruction.

Chapter 3.5 exhibits 3D volume reconstruction using simplex fitting and faring with hierarchical simplices. Experiments and discussion will be presented in *Chapter 3.6* followed by a conclusion in *Chapter 3.8*.

3.2 Previous Work

Many research efforts from the medical imaging community have been devoted to establishing techniques for 3D histology analysis and visualization. Chan *et al.* proposed a methodology for making optimal registration decisions during 3D volume reconstruction [5]. A semi-automatic registration technique for 3D volume reconstruction from fluorescent laser scanning confocal microscope (LSCM) imagery was presented by Lee *et al.* [34]. They later proposed a fusion-based approach to address the problem of 3D volume reconstruction from depth adjacent sub-volumes acquired using a confocal laser scanning microscope (CLSM) [35]. Tan *et al.* presented a feature curve-guided alignment algorithm to register microscopic slices based on the NURBS-based optimization of the extracted feature curves from the microscopic data [88]. Readers may find other relevant literature in [7, 1, 70].

Volume modeling and rendering via tetrahedral mesh has recently gained more popularity as well. Researchers are primarily interested in constructing or using the volumetric tetrahedral mesh dataset to achieve better rendering effects. Cignoni *et al.* [9] proposed a multi-resolution model for the representation and visualization of unstructured volumetric datasets based on a decomposition of the 3D domain into tetrahedra. Later, they presented a tetrahedral mesh simplification approach based on accurate error evaluation [8]. Roxborough and Nielson [74] presented a method for the visualization of freehand collected 3D ultrasound data based on adaptive, progressive construction of the tetrahedral mesh. A tetrahedral mesh structure to represent anatomical structures was adopted by Yao and Taylor [105]. They proposed an efficient and automatic algorithm to construct a tetrahedral mesh from contours in CT images. A rich body of previous work on tetrahedral meshes suggest that a simplicial complex is potentially promising to serve for both visualization and modeling.

Even though volume modeling using univariate splines, such as B-splines or NURBS, has received much attention from modeling and visualization communities in recent years [67, 78, 28, 41], multivariate simplex splines-based volume techniques based on a domain of simplices are less explored. They have only been extensively investigated in mathematical science. Motivated by an idea of Curry and Schoenberg for a geometric interpretation of univariate B-splines, de Boor [56] first presented a brief description of multivariate simplex splines. Since then, their theoretical perspectives have been explored extensively. From the blossoming point of view, Dahmen *et al.* [13] proposed triangular B-splines. Since then, Seidel and his colleagues demonstrated the practical feasibility of bivariate DMS-splines in graphics and shape design in [21, 60]. In sharp contrast to theoretical advances, the application of trivariate simplex splines has been severely under-explored. Hua *et al.* [25] initiated using simplex spline for heterogeneous solid modeling and derived several theoretical formula for fast rendering of the simplex spline volumes. Recently, Rössl *et al.* [56] presented a novel approach to reconstruct volume from structure-gridded samples using trivariate quadric super splines defined on a uniform tetrahedral partition. They used Bernstein-Bézier techniques to compute and evaluate the trivariate spline and its gradient. Also, the exact intersection for a ray and prescribed isovalue can be easily determined in an analytic and exact way. The major difference between Rössl *et al.* 's method and ours lies in:

- Our method uses arbitrary tetrahedral domain instead of regular.
- Our method uses a general trivariate DMS-splines of degree $n \geq 2$ which has more degrees of freedom (control points and knots); the continuity between adjacent tetrahedra can be easily maintained because of the optimal smoothness of DMS-splines.
- Our method uses hierarchical structures to model level-of-details.

3.3 Multivariate Simplex Spline Volume

In this section, we first briefly review multivariate simplex splines, which are the theoretical background throughout my dissertation. Then, we formalize the volume representation based on the multivariate simplex splines.

3.3.1 Multivariate Simplex Splines Definition

A degree n multivariate simplex spline, $M(\mathbf{x}|\mathbf{x}_0, \dots, \mathbf{x}_{n+3})$, can be defined as a function of $\mathbf{x} \in \mathbb{R}^3$ over the half open convex hull of a point set $\mathbf{V} = [\mathbf{x}_0, \dots, \mathbf{x}_{n+3}]$, depending on the $n+4$ knots $\mathbf{x}_i \in \mathbb{R}^3, i = 0, \dots, n+3$. The multivariate simplex splines may be formulated recursively, which facilitates point evaluation and its derivative and gradient computation. When $n = 0$,

$$M(\mathbf{x}|\mathbf{x}_0, \dots, \mathbf{x}_3) = \begin{cases} \frac{1}{|\text{Vol}_{\mathbb{R}^3}(\mathbf{x}_0, \dots, \mathbf{x}_3)|}, & \mathbf{x} \in [\mathbf{x}_0, \dots, \mathbf{x}_3], \\ 0, & \text{otherwise,} \end{cases}$$

and when $n > 0$, select four points $\mathbf{W} = \{\mathbf{x}_{k_0}, \mathbf{x}_{k_1}, \mathbf{x}_{k_2}, \mathbf{x}_{k_3}\}$ from \mathbf{V} , such that \mathbf{W} is affinely independent, then

$$M(\mathbf{x}|\mathbf{x}_0, \dots, \mathbf{x}_{n+3}) = \sum_{j=0}^3 \lambda_j(\mathbf{x}|\mathbf{W}) M(\mathbf{x}|\mathbf{V} \setminus \{\mathbf{x}_{k_j}\}), \quad (3.1)$$

where $\sum_{j=0}^3 \lambda_j(\mathbf{x}|\mathbf{W}) = 1$ and $\sum_{j=0}^3 \lambda_j(\mathbf{x}|\mathbf{W}) \mathbf{x}_{k_j} = \mathbf{x}$.

The directional derivative of $M(\mathbf{x}|\mathbf{V})$ with respect to a vector \mathbf{d} is defined as follows:

$$D_{\mathbf{d}}M(\mathbf{x}|\mathbf{V}) = n \sum_{j=0}^3 \mu_j(\mathbf{d}|\mathbf{W}) M(\mathbf{x}|\mathbf{V} \setminus \{\mathbf{x}_{k_j}\}), \quad (3.2)$$

where $\mathbf{d} = \sum_{j=0}^3 \mu_j(\mathbf{d}|\mathbf{W}) \mathbf{x}_{k_j}$ and $\sum_{j=0}^3 \mu_j(\mathbf{d}|\mathbf{W}) = 0$.

3.3.2 Multivariate Simplex Spline Volume Definition

Now let \mathbf{T} be an arbitrary “proper” tetrahedralization of the bounded domain $D \subset \mathbb{R}^3$. Here, “proper” means that every pair of domain tetrahedra are disjoint, or share exactly one

vertex, one edge, or one face. To each vertex t of the tetrahedralization \mathbf{T} , we assign a knot cloud, which is a sequence of points $[t_0, t_1, \dots, t_n]$, where $t_0 \equiv t$. We call t primary-knot and $[t_1, \dots, t_n]$ sub-knots. *Figure 3.1-(a)* shows 4 vertices with cubic knot clouds associated, which are labeled as $\mathbf{p}, \mathbf{q}, \mathbf{r}$, or \mathbf{s} group, respectively. The primary-knots are rendered with yellow dots and sub-knots with blue dots. We will use these two colors to differentiate the primary-knots and sub-knots in the rest illustrations.

For every tetrahedron $I \in \mathbf{T}$, assume $I = (\mathbf{p}, \mathbf{q}, \mathbf{r}, \mathbf{s}) = (\mathbf{p}_0, \mathbf{q}_0, \mathbf{r}_0, \mathbf{s}_0)$. We call $(\mathbf{p}, \mathbf{q}, \mathbf{r}, \mathbf{s})$ the underlying tetrahedron. All the other tetrahedra $[\mathbf{p}_i, \mathbf{q}_j, \mathbf{r}_k, \mathbf{s}_l]$ with $0 < i + j + k + l \leq n$ are called the virtual tetrahedra. *Figure 3.1-(a)* shows the underlying tetrahedron with shading. *Figure 3.1-(b)* demonstrates the virtual tetrahedra rendered with different shading colors.

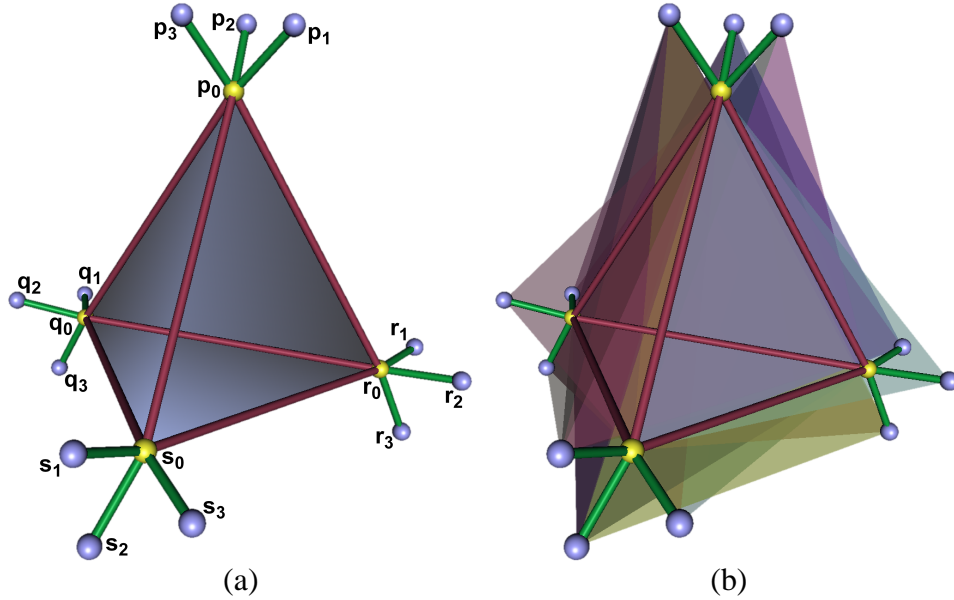


Figure 3.1: (a) A domain tetrahedron demonstrated with its knot clouds assigned and labeled. The underlying tetrahedron, $(\mathbf{p}, \mathbf{q}, \mathbf{r}, \mathbf{s})$, is rendered as a shaded tetrahedron; (b) The virtual tetrahedra of the domain tetrahedron are visualized in different colors with the opacity value of 0.4. In (a) and (b), the degree of the domain is cubic hence each vertex of the tetrahedron has three sub-knots. The primary-knots are presented with yellow dots while sub-knots are depicted with blue dots. The red lines connecting the primary-knots indicate the underlying tetrahedron. Each green line here denotes the association between primary-knot and sub-knot.

Then for every tetrahedron I , we require

- all the tetrahedra $[\mathbf{p}_i, \mathbf{q}_j, \mathbf{r}_k, \mathbf{s}_l]$ with $i + j + k + l \leq n$ are non-degenerate, i.e., the underlying tetrahedron and virtual tetrahedra should be valid.
- the set

$$\Omega = \text{interior}(\cap_{i+j+k+l \leq n} [\mathbf{p}_i, \mathbf{q}_j, \mathbf{r}_k, \mathbf{s}_l]) \quad (3.3)$$

is not empty.

- if I is a boundary tetrahedron, the sub-knots assigned to the boundary vertices must lie outside of D .

The condition that Ω is nonempty states that the sub-knots associated with different vertices of I are all separated from each other. The underlying tetrahedron I and its virtual tetrahedra have the same orientation. As shown in *Figure 3.1-(a)*, in our framework, the orientation of the tetrahedron is defined as, observing from \mathbf{p}_i , the triangle formed by $(\mathbf{q}_j, \mathbf{r}_k, \mathbf{s}_l)$ is clockwise-oriented where $i + j + k + l \leq n$.

The formation of Ω can be intuitively described as: starting from the underlying tetrahedron, we chop it using the triangle faces from each virtual tetrahedron, and only keep the part inside of the triangle faces. As the starting shape of the underlying tetrahedron is convex, the chopping operation will not affect its convexity. Hence the final shape of Ω is a convex, solid polyhedron if nonempty.

Figure 3.2-(a) and *Figure 3.2-(b)* depict the Ω of a cubic domain tetrahedron, with and without virtual tetrahedra rendered, respectively. Note that if $\Omega \neq \emptyset$, Ω must be a convex solid polyhedron formed by the interior of the underlying tetrahedron and virtual tetrahedra. *Figure 3.2-(a)* and *Figure 3.2-(b)* illustrate the Ω as a blue, convex, and solid polyhedron.

We then define, for each tetrahedron $I \in \mathbf{T}$ and $i + j + k + l = n$ (in the following, we use β to denote 4-tuple (i, j, k, l)), the knot sets are

$$V_{\beta}^I = [\mathbf{p}_0, \dots, \mathbf{p}_i, \mathbf{q}_0, \dots, \mathbf{q}_j, \mathbf{r}_0, \dots, \mathbf{r}_k, \mathbf{s}_0, \dots, \mathbf{s}_l]. \quad (3.4)$$

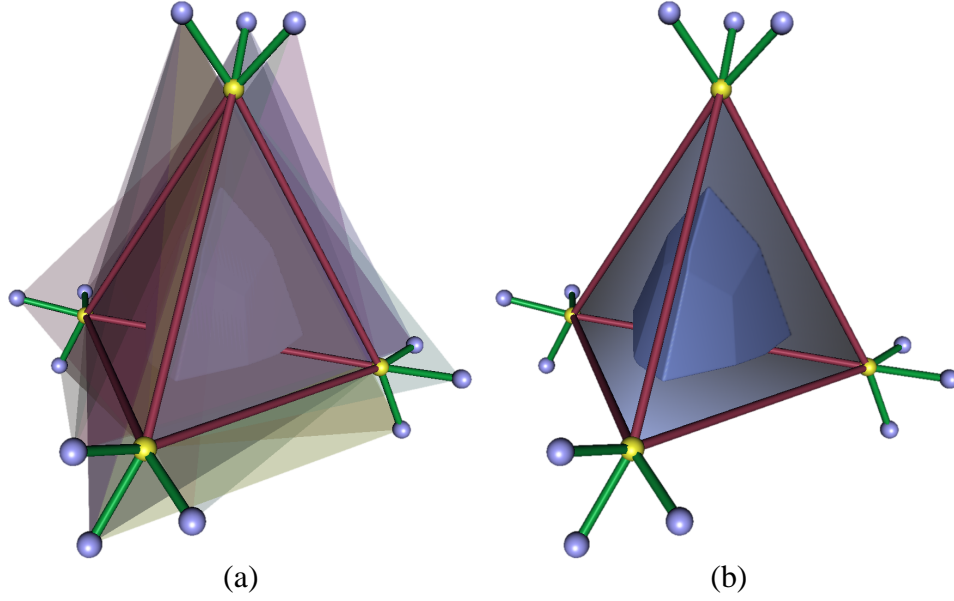


Figure 3.2: (a) The Ω of a domain tetrahedron, formed by the interior of the underlying tetrahedron and virtual tetrahedra, is rendered with a blue polyhedron. The virtual tetrahedra are visualized in different colors with opacity value 0.1; (b) The virtual tetrahedra are removed to better visualize the Ω .

For an example in *Figure 3.1* and *Figure 3.2*, as the degree of the domain is cubic, V_β^I has 16 elements: 4 primary-knots and 12 sub-knots.

The basis functions of normalized simplex splines are then defined as

$$N_\beta^I(\mathbf{u}) = |\det(\mathbf{p}_i, \mathbf{q}_j, \mathbf{r}_k, \mathbf{s}_l)| M(\mathbf{u}|V_\beta^I). \quad (3.5)$$

These basis functions can be shown to be all non-negative and to form a partition of unity. The multivariate spherical simplex spline volume is the combination of a set of basis functions with control points \mathbf{c}_β^I :

$$\mathbf{s}(\mathbf{u}) = \sum_{I \in \mathbf{T}} \sum_{|\beta|=n} \mathbf{c}_\beta^I N_\beta^I(\mathbf{u}). \quad (3.6)$$

The “generalized” control points \mathbf{c}_β^I are now $(k + 3)$ -dimensional vectors, including control points (p^x, p^y, p^z) for the solid geometry, and control coefficients (g^1, \dots, g^k) for the attributes, where k denotes the number of attributes associated with the geometry. The spherical simplex

splines are ideal to model genus-zero, heterogeneous solid objects. The number of physical properties is application-oriented. For a concise expression of the formulation, without loss of generality, we will deal with only one physical attribute in the following formulas.

3.4 Tetrahedral Domain Construction

In our volume reconstruction algorithm, we plan to employ multivariate simplex spline as the volume representation approach due to its attractive properties described before. The first important step is to construct a good initial tetrahedralization basis for the later data fitting and faring steps. When starting with a good initial tetrahedralization, the later refinement computation will be greatly reduced. The good initial domain tetrahedralization should preserve both geometric and attribute features of the original volume dataset.

3.4.1 Initial Alignment of 2D Slices

Before the structure of 3D histology can be explored and analyzed, generating a high-fidelity 3D volume is a crucial and preliminary step in which all histology slices need to be stacked into one volume. Structure-gridded volume data structure can be employed here and we choose Analyze 7.5 file format, which is already a well-established industry standard.

First, 2D histology slices are scanned into the computer through a digital histology film scanner. This high resolution equipment can produce quality images with detailed cell structures. In this step, necessary image processing filters, for instance, Gaussian smoother, will be applied to the raw data due to the inevitable noises. *Figure 3.3* shows a part of a sequence of 2D images scanned from a histology sectioning profile.

Between two neighboring histology sections, there is no high-order discontinuity in structure, i.e., there exists substantial similarities which can be used to match adjacent slices. Based on this observation, we need to minimize the following equation:

$$\min DIF_{den} = \sum_{i=1}^{n-1} \|I(i) - T \cdot I(i+1)\|^2, \quad (3.7)$$

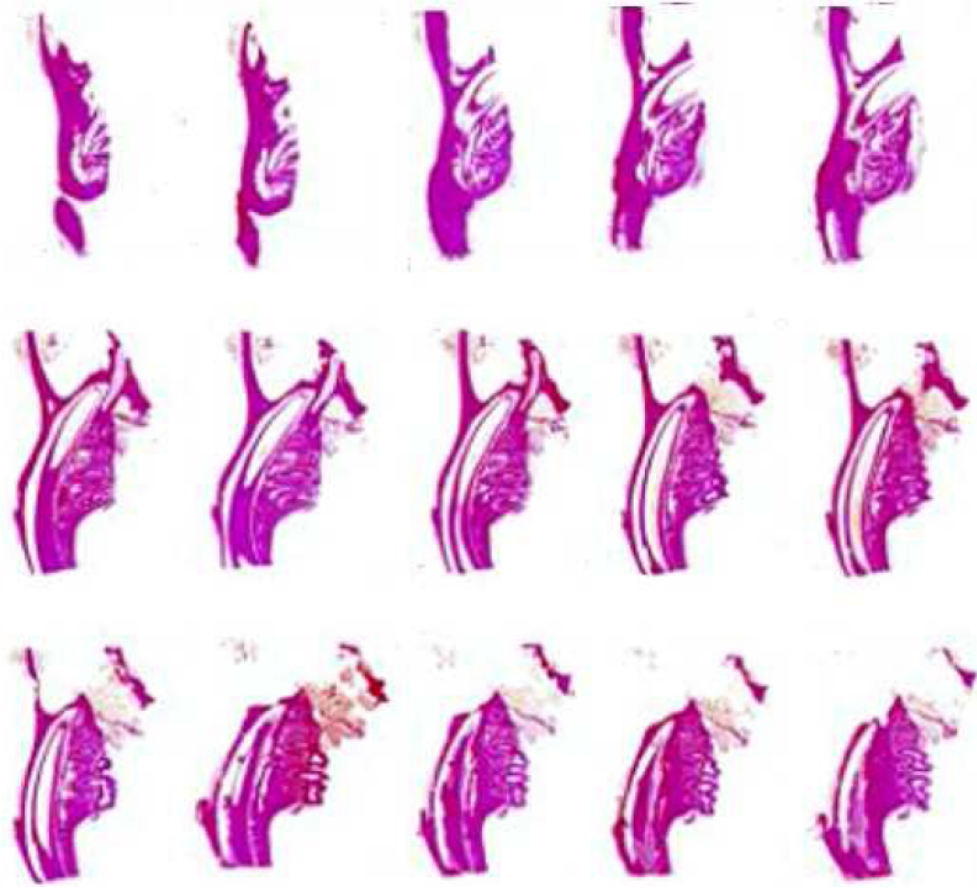


Figure 3.3: A part of a sequence of 2D images scanned from a histology sectioning profile. Histology structures gradually change from slice to slice.

where $I(i)$ indicates the density distribution of i^{th} slice. $I(i + 1)$ is subject to the affine transformation matrix T . Here we select the i^{th} slice as the stationary one, and apply affine transformation to the $(i + 1)^{th}$ slice. The correspondent affine transformation T is a 4×4 matrix as below:

$$\begin{bmatrix} x' \\ y' \\ z' \\ 1 \end{bmatrix} = T \begin{bmatrix} x \\ y \\ z \\ 1 \end{bmatrix} \quad (3.8)$$

where $T = \begin{bmatrix} t_{00} & t_{01} & t_{02} & t_{03} \\ t_{10} & t_{11} & t_{12} & t_{13} \\ t_{20} & t_{21} & t_{22} & t_{23} \\ t_{30} & t_{31} & t_{32} & t_{33} \end{bmatrix}$, and $\begin{bmatrix} x \\ y \\ z \\ 1 \end{bmatrix}$ denotes the original position of a voxel and

$\begin{bmatrix} x' \\ y' \\ z' \\ 1 \end{bmatrix}$ denotes the transformed position. Because we use homogeneous coordinates here, the

position vector in *Equation 3.8* is extended to order 4. Here T is the combination of rotation factor and translation factor. *Equation 3.7* is essentially a least square problem. Solving this system, we can obtain a set of transformations which construct an initial alignment of all 2D histology sections.

3.4.2 Carver Algorithm for Tetrahedralization

Constraint Delaunay Tetrahedralization (CDT) [15] is the most widely used algorithm to construct tetrahedral mesh. However, CDT works great only for those models from which corresponding isosurfaces can be explicitly extracted, i.e., those with simple geometry. To increase the versatility of our framework, we develop another algorithm for those without such well-defined isosurfaces, e.g., histology models. The algorithm fulfills the objective in two major steps: 1) arbitrary Delaunay tetrahedralization, and 2) outside tetrahedra removal using Carver Algorithm. The detail steps of our algorithm are described as follows:

1. From *Chapter 3.4.1*, what we obtain is a structure-gridded volume. The first step here is to down-sample the volume to get finite discretized points which are the later vertices of the tetrahedral domain. It's intuitive that we shall have more tetrahedra in the feature area. More points in feature-dense areas and less points in uniform areas are selected according to the voxels' intensity variation levels. Here, we simply use gradients of physical attributes as the level stated. *Figure 3.4-(a)* shows the discretized point sets.

2. Then we use the points selected from the initial volume as the vertices input of *genus – zero* Delaunay tetrahedralization. After arbitrary Delaunay tetrahedralization, the initial *genus – zero* tetrahedral mesh is retrieved with the convex hull of the vertices as its boundary mesh. Accordingly, more tetrahedra will be created in the feature area due to more vertices presented and vice versa. *Figure 3.4-(b)* is the mesh created by arbitrary Delaunay tetrahedralization.
3. Starting from one user specified tetrahedron, neighboring tetrahedra will be removed recursively. Those removed tetrahedra form another object, namely “OUTSIDER”, and we only need to detect the neighboring tetrahedra of its boundary. The criteria for stopping is that there are no additional tetrahedra to be added to “OUTSIDER”.
4. The carver algorithm yields tetrahedra of arbitrary topology. Islands should be removed based on the fact that histology may be of any topology, but its geometric feature is continuous anywhere. Islands mostly are caused by inevitable noise from original data set. *Figure 3.4-(c)* shows the tetrahedral mesh after 2 removal steps, with volume presented. *Figure 3.4-(d)* shows the initial mesh after islands being removed.

3.5 Volume Reconstruction

To model the histology attribute over the multivariate simplex spline based volume, it is much more desirable to have a fitting tool which converts the discrete volume data to continuous splines. In this section, we propose a method for volume reconstruction using multivariate simplex splines.

In this section, we will present an effective framework for the reconstruction of volumetric data from a sequence of 2D images. The 2D images are first aligned to generate an initial 3D volume, followed by the creation of a tetrahedral domain using the Carver algorithm. The resulting tetrahedralization preserves both geometry and topology of the original dataset. Then a solid model is reconstructed using simplex splines with fitting and faring procedures.

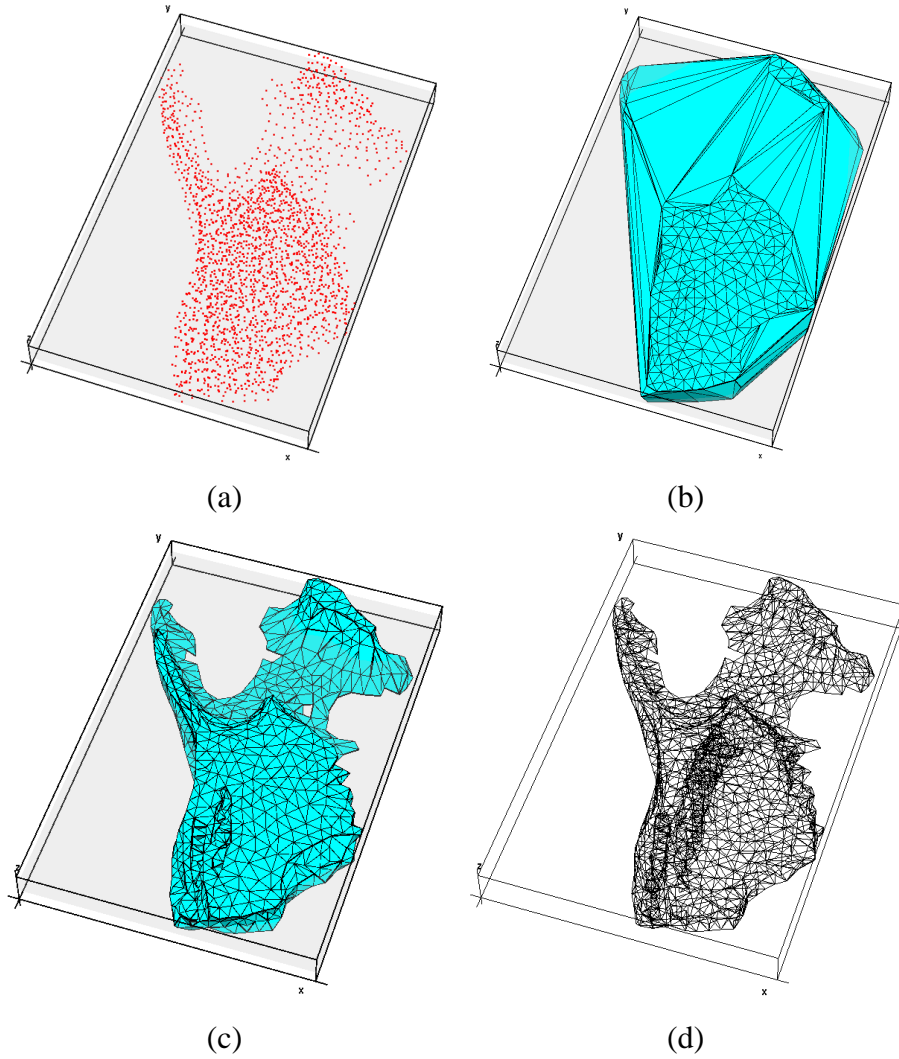


Figure 3.4: (a) Point set down-sampled as input of Delaunay tetrahedralization; (b) Arbitrary Delaunay tetrahedralization with convex hull as its boundary mesh; (c) Carver Algorithm removes outside tetrahedra away from volume; (d) Initial mesh after islands removal.

3.5.1 Hierarchical Simplex Spline Volumes

Before we introduce the hierarchical simplex spline volumes, let us first review some results on a triangular B-spline.

Theorem (Piecewise polynomial representation) [80] Let F be any piecewise polynomial of degree n over a given triangulation T , and let F_I be the restriction of F to the triangle $\Delta(I)$ and f_I be the polar form of F_I . Then the following identity holds for all \mathbf{u} :

$$F(\mathbf{u}) = \sum_{I \in T} \sum_{|\beta|=n} f_I() N_{\beta}^I(\mathbf{u}). \quad (3.9)$$

For more information about polar form, we refer the readers to [79, 80].

The above theorem holds for a general $s(\geq 2)$ -variate simplex spline. Let I be the tetrahedron of interest in the domain of $s(\mathbf{u})$, and we want to add more degrees of freedom in I to model the details. There are two different ways to solve this problem. The first is knot insertion, in which one knot is inserted into the tetrahedron I , and I is subdivided into four tetrahedra. Multiple knots can be inserted one by one. The second is hierarchical structures by building a new spline $s_I^1(\mathbf{u})$, whose domain is a regularly subdivided tetrahedra of I . The major differences between knot insertion and hierarchical structures (see *Figure 4.5*) are as follows:

- Hierarchical structures need additional splines $s_I^1(\mathbf{u})$, but do not change the original spline $s(\mathbf{u})$, while knot insertion does affect the spline $s(\mathbf{u})$.
- Hierarchical structures need special technique to maintain certain continuity between the original spline and new spline, while knot insertion does not.
- Knot insertion could introduce poor quality tetrahedra, while hierarchical structures do not.

In order to maintain certain continuity between s_u^1 and s_u , they must have “overlays”. Unlike the tensor-product B-splines which usually extend the domain one level to maintain C^1 -continuity between the two layers, we use the boundary tetrahedra as the overlays, which means the control points and knots inside these tetrahedra are fixed. The detailed hierarchical simplices construction is as follows:

1. Subdivide the I to a user-specified level.
2. Compute all the control points in the domain I by *Equation 4.21*.

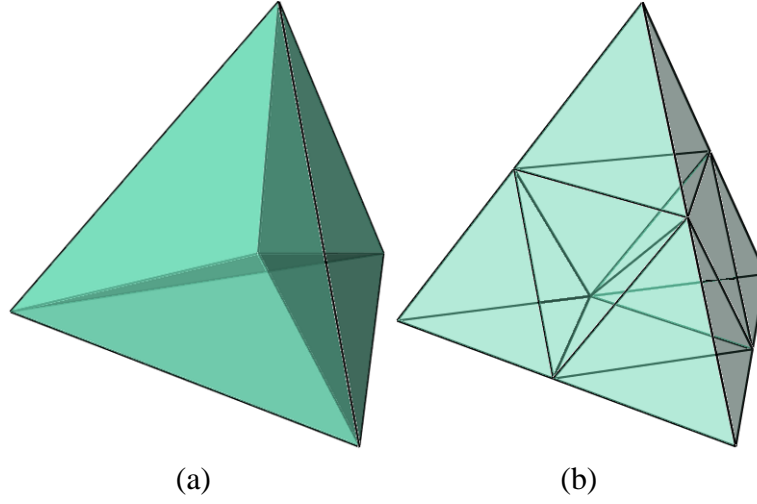


Figure 3.5: (a) Knot insertion. After one knot is inserted at the barycenter of the original tetrahedron, the original one is subdivided into four tetrahedra; (b) Hierarchical simplices. After knots are inserted at the center of the edges of the original tetrahedron, the original one is subdivided into four tetrahedra.

3. Set all the control points and knots associated to the boundary tetrahedra to be fixed and others be free.

Note that the refinement (1-3) produces the exact presentation of the original splines. Recall that movement of a free control point c_β^J only influences the splines on the tetrahedron $\Delta(J)$ and on the tetrahedra directly surrounding $\Delta(J)$. Since we fix the control points and knots of the boundary tetrahedra, any change of internal control points will not affect the function value and gradient across the boundary. Thus, we maintain C^1 -continuity between the new spline and original one.

For better understanding, we illustrate the above scheme with an example of triangular B-spline surface. *Figure 3.6-(a)* is the original surface and the marked area is the region of interest to be refined. In *Figure 3.6-(b)*, we construct another triangular B-spline surface that represents the marked area exactly. This new surface has refined domain triangulation and more control points. In *Figure 3.6-(c)*, we move a free control point of the new surface and the two surfaces still blend smoothly. Note that the surfaces in *Figure 3.6-(b)* and *Figure 3.6-(c)* use the same domain.

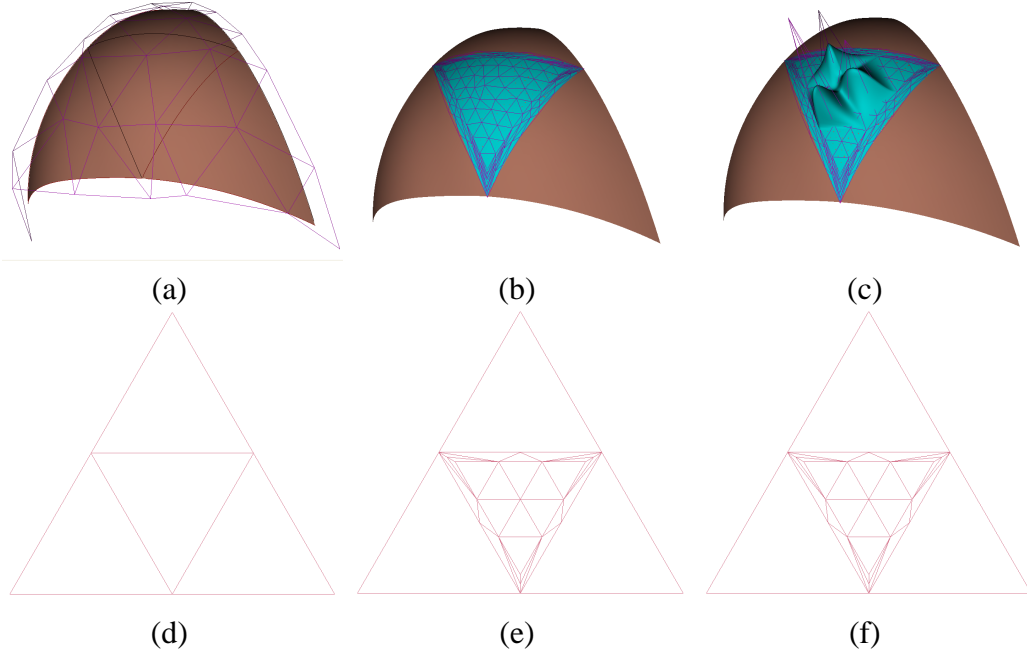


Figure 3.6: Illustration of hierarchical bivariate simplex splines surfaces. (a) A bivariate simplex spline surface; (b) Hierarchical structure of one domain triangle of (a); (c) Moving the free control points will not affect the continuity across the boundary; (d) Corresponding domain triangulation of (a); (e) Corresponding domain triangulation of (b); (f) Corresponding domain triangulation of (c).

3.5.2 Volume Reconstruction Problem Statement

Formally, the problem of volume reconstruction can be stated as follows: given a set $P = \{\mathbf{p}_i\}_{i=1}^m$ of points $\mathbf{p}_i = (x_i, y_i, z_i, d_i) \in \mathbb{R}^4$, find a multivariate simplex splines volume $s : \mathbb{R}^3 \rightarrow \mathbb{R}^4$ that approximates P .

Since we are interested only in reconstructing the data from attributes, our multivariate simplex spline volumes are scalar functions, i.e., the control points $\mathbf{c}_\beta^I \in \mathbb{R}$ are scalar values. Unlike the existing fitting algorithms with parametric representations which usually find a one-to-one mapping between the data points and the points in the parametric space, our method skips this parameterization procedure. As stated in *Chapter 3.4*, we first construct a tetrahedralization parametric domain which is close to the original geometry of the to-be-fitted dataset. We use the position (x_i, y_i, z_i) of the data point \mathbf{p}_i as its parametric value. Therefore, we need

to minimize the following objective function:

$$\min E(F) = E_{dist}(\mathbf{s}) + \lambda \cdot E_{fair}(\mathbf{s}), \quad (3.10)$$

where

$$E_{dist}(\mathbf{s}) = \sum_{i=1}^m (d_i - \mathbf{s}(x_i, y_i, z_i))^2, \quad (3.11)$$

and $E_{fair}(\mathbf{s})$ is a fairness function with the smoothing factor $\lambda \geq 0$.

The most commonly-used fairness functions, such as simplified membrane energy and thin-plate energy, require integration, which is usually computationally intensive. In this section, we use a simple, yet effective, fairness function:

$$E_{fair}(s) = \sum_{i=1}^m (n_i \cdot \mathbf{s}(x_i, y_i, z_i))^2, \quad (3.12)$$

where n_i is the gradient at point (x_i, y_i, z_i) . Note that these gradients can be calculated by local least-squares fitting to P .

3.5.3 Hierarchical Fitting

The above volume data fitting procedure attempts to minimize the total squared distance of the volume data points \mathbf{d}_i to the simplex spline $\mathbf{s}(\mathbf{u})$. For some regions with very dense points or sharp features, it is often desirable to introduce new degrees of freedom into the spline representation in order to improve the fitting quality. Hierarchical structures are suitable for this purpose.

If the error metric inside a tetrahedron I is greater than a user-specified value, and it contains enough points, e.g., $8 * N_{min}$ in our implementation, we construct the hierarchical simplex splines $\mathbf{s}_I^{(1)}(\mathbf{u})$ on I as follows:

1. We shrink I slightly and get a smaller tetrahedron, J . Denote $I \setminus J$ the narrow band between I and J .

2. Subdivide J into 8 tetrahedra.
3. Perform tetrahedralization for the narrow band between I and J .
4. Compute the control points of $\mathbf{s}_I^{(1)}(\mathbf{u})$ by *Equation 4.21*.
5. Fix the control points and knots associated to the tetrahedra in the band $I \setminus J$ and let others be free.
6. For all the data points inside I , define $e_i = d_i - \mathbf{s}(x_i, y_i, z_i)$.
7. Solve $E_{dist}^I = \sum_{(x_i, y_i, z_i) \in I} (e_i - \mathbf{s}_I^1(\mathbf{u}))^2$ with the free control points and knots.

This refinement step is called repeatedly until the stopping criteria is satisfied. Then the output of our volume reconstruction is a series of multivariate simplex splines, i.e., to evaluate $\mathbf{u} \in \Delta I$, we use

$$\mathbf{s}(\mathbf{u}) = \mathbf{s}^0 \mathbf{u} + \mathbf{s}_I^1(\mathbf{u}) + \mathbf{s}_I^2(\mathbf{u}) + \dots$$

The number of levels needed in evaluation depends the application.

Although the base domain tetrahedron contains enough points, the number of data points in some subdivided tetrahedra may be less than N_{min} due to the nature of unstructured data. If this happens, we also fix the control points inside the small tetrahedra to avoid the under-determined problem.

In order to improve the performance of our fitting method, we start with a down-sampled dataset in the coarse level and consider the whole dataset in the fine level. For example, when fitting the rat tooth data, we use 64,572 points in level 0 to reconstruct the rough geometry and density and use 350,000 points in level 2 to reconstruct the details.

3.6 Experimental Results

We have implemented a prototype system on a PC with 2.8 GHz P4 CPU and 2GB of RAM. The system is written in VC++ and VTK 4.2. *Table 3.1* shows the performance statistics of

our fitting algorithm on several datasets, where the fitting error is the root-mean-square error. With the help of hierarchical simplices, our volume reconstruction algorithm can achieve very good results. The entire 3D reconstruction procedure from 2D histology sequences takes a few hours to complete.

Sample	Continuous Simplices (Num.)	Fitting Error
1	10231	1.878×10^{-4}
2	12855	1.526×10^{-4}

Table 3.1: Statistics of 3D reconstruction.

Through our framework, aseptic loosening at rat apical root can be examined and compared by quantifying the reconstructed 3D histology data. We also propose a scheme to analyze the aseptic loosening region of interest by comparing histology data with μ CT data. Bone resorption can be measured along time axis. *Figure 3.7* shows an example. Because histology and μ CT are different modalities, necessary registration will be acquired before such analysis, to make the comparison substantial.

3.7 Comparison with Existing Methods

In this section, we will briefly compare our volume reconstruction paradigm with other volume reconstruction schemes. As there are quite a lot literature on this research topic, I only choose several of them as the representative ones.

Authors	Method	Output	Continuous
Krinidis <i>et al.</i> [33]	Distance Transform-Based Global Cost Function	Structure-gridded Volume	No
Lee <i>et al.</i> [35]	Sub-Volumes Adjacency Calculation	Structure-Gridded Volume	No
Tan <i>et al.</i> [88]	Feature-Curve Guided Volume Reconstruction	Structure-Gridded Volume	No
Our Method	Multivariate Simplex Spline Volume Fitting	Parametric Volume	Yes

Table 3.2: Comparison of 3D reconstruction schemes.

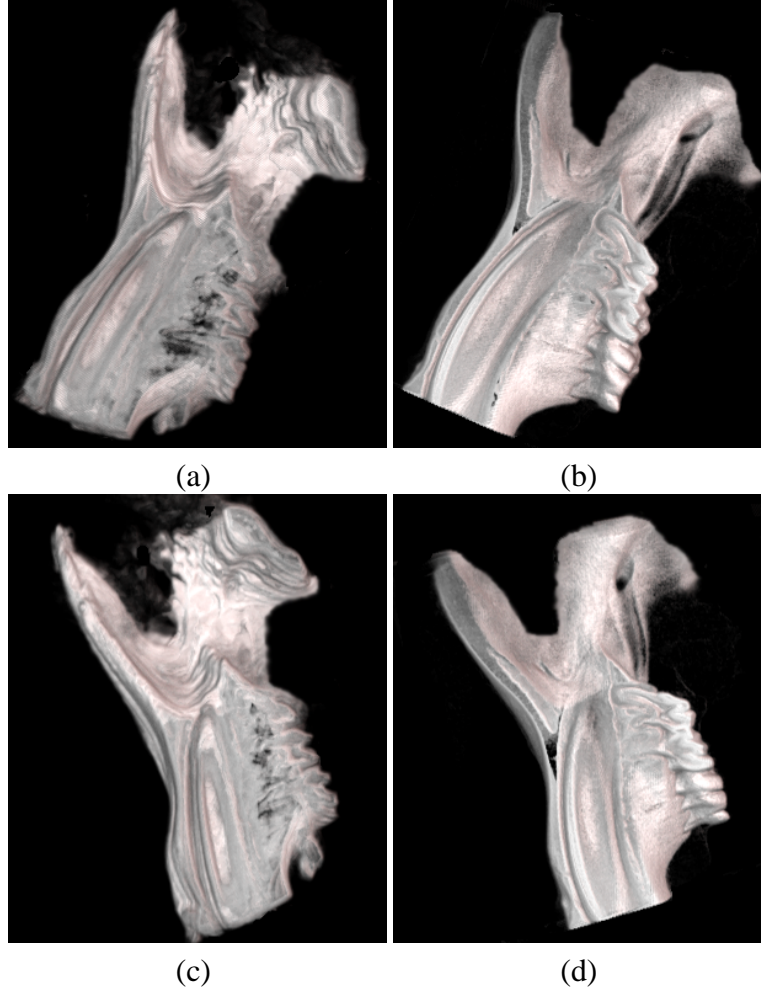


Figure 3.7: (a) 3D visualization of reconstructed 3D histology volume after similarity mapping; (b) 3D visualization of the corresponding μ CT volume from the same view point; (c) 3D visualization of reconstructed 3D histology volume after global faring; (d) 3D visualization of corresponding μ CT volume from the same view point.

As we may see from the table, most of current research on medical volume reconstruction focuses on the similarity measure of the adjacent slices and the output is a discrete and structure-gridded volume. On the other end of the spectrum, our unrival reconstruction scheme based on multivariate simplex spline is a true parametric and continuous method with high-genus and arbitrary geometry support.

3.8 Summary

In this chapter, we have articulated a new integral approach for representing, modeling, and reconstructing volume data. In particular, we employ a hierarchical multivariate simplex spline model that is defined over a hierarchical and progressive tetrahedralization of arbitrary 3D domains. Our framework supports both structured and unstructured data. The modeled volume can be of complicated geometry and arbitrary topology. We have developed a new paradigm to reconstruct non-discrete models from a sequence of 2D images. With the flexible hierarchical structures, our method can adaptively refine the domain tetrahedralization and introduce more degrees of freedom locally for better fitting results. The volumes can then be re-modeled and re-edited by manipulating the control vectors and/or associated knots of multivariate simplex splines easily. Our results demonstrate that the proposed paradigm augments the current tetrahedral representation and reconstruction techniques with new and unique advantages which can be applied to diverse research areas.

CHAPTER 4:

NONRIGID VOLUME REGISTRATION WITH MULTIVARIATE SIMPLEX SPLINE BASED FREE-FORM DEFORMATION

This chapter presents a novel and efficient computational framework for nonrigid volume registration using multiresolution volumetric simplex spline-based free-form deformation. In sharp contrast to existing volume registration algorithms using free-form deformation schemes based on tensor product B-spline volumes, we employ multiresolution volumetric simplex spline volume as our underline volume representation to achieve more efficiency, flexibility, and accuracy. Our framework first applies a rigid affine transformation to the floating volume to have it roughly aligned to the reference volume. Then the registration is achieved by searching for the optimum deformation that minimizes a cost function comprising a weighted combination of volume similarity measure, volume-preserving penalty term and smoothness penalty term. Our registration scheme can greatly reduce the degree of freedom due to its non-tensor product nature. With the merit from multiresolution simplices, our paradigm can further reduce the registration error without introducing unnecessary degree of freedom, which is usually required by traditional B-spline-based registration schemes. We have successfully applied our framework to the registration of magnetic resonance imaging (MRI) brain volumes and the preliminary experimental results demonstrate the powerful potentiality of our framework being employed to register volumes acquired from intramodality and intermodality imaging systems in other biomedical applications.

4.1 Introduction and Motivation

Nonrigid registration of intermodality and intramodality images is playing an increasingly important role both in medical and research realms for the reason many medical activities often rely on the complementary information retrieved from different images, which are obtained from intermodality or intramodality imaging system. For instance, computed tomography (CT)

data affords more precise dose calculation while magnetic resonance imaging (MRI) provides better performance in tumor outlining. Another case in point is brain disease diagnosis and surgery. Professionals usually interpret the brain MRI data before the operation. After a patient's skull is open, the brain will behave increasing deformation, known as brain shifting, during ongoing surgical procedures, predominantly due to the gravity and the drainage of cerebrospinal fluid. This will inevitably lead to the repositioning of the surgical targets embedded in brain. As a compensation to increase the spatial accuracy of modern neuronavigation systems, intraoperative magnetic resonance imaging (IMRI) is widely used for quantitative analysis and visualization of this phenomenon [50]. The output images from MRI and IMRI vary in terms of image density with different neuronavigation scanning parameters setup. Hence the registration between these images becomes an indispensable preliminary procedure before any further diagnosis, description, or surgery.

Current image registration generally includes two procedures: global transformation and local transformation. The overall motion of the object is described through the global transformation. The simplest, yet broadly adopted way, is a rigid affine transformation [76] parameterized by 6 degrees of freedom, i.e., 3 degrees of freedom for translation and 3 degrees of freedom for rotation. A more general transformation, which introduces additional 6 degrees of freedom, 3 degrees of freedom for scaling and 3 degrees of freedom for sheering, may be used as well. In medical imaging modalities, the scaling information can be obtained through the parameter setup of the neuro-navigation system, e.g., the detecting spacing of MRI scanning. There is either no sheering in these imaging modalities. Without loss of generality, we skip the degrees of freedom introduced by scaling and sheering.

The pure rigid affine transformation models merely take the geometry of the object into account, i.e., assuming the to-be-registered volumes share the same and uniform intensity, which is not always the case. As a compensation, in recent years, many voxel-based similarity measure have yielded increasingly promising results for intermodality registration. Particularly, voxel-

based similarity measures based on joint entropy [83], mutual information [11, 99, 84], and normalized mutual information [85, 38] are gaining more and more popularity. Rohlfing *et al.* [69] implemented the voxel-based similarity measure in their algorithm independently and successfully applied it to their study. Alternatively, Zuo *et al.* [109] proposed a registration which minimizes the ratio of variance between images. But the work conducted from those pioneers will not change the nature of the rigid motion. The rigid affine transformation is the best guess of the matching between the two volumes without any local transformation involved. Hence it only serves as the initial estimate for the nonrigid registration.

In the recent decades, researchers proposed all kinds of nonrigid registration algorithms to better achieve the local transformation. Generally speaking, these algorithms can be broadly classified into two categories: those based on elastic deformations and those based on spline-based deformations. The animal model proposed by Collins *et al.* [12], and the demon model proposed by Thirion [94], fall into the former category. Their models are based on the assumption that the intensity of tissues remains constant in different modalities, which is not always true. Edwards *et al.* [16] modeled 2D deformation of the brain during surgery using a 3-component model consisting of rigid, elastic, and fluid structures. Hagemann *et al.* [23] proposed a 2D nonrigid image registration scheme that aims to model the actual mechanical properties of the brain tissue. Both methods were originally described in 2D cases, and can be generalized to 3D counterpart. But the computation cost of their methods is prohibitively high in 3D cases.

On the other end of the spectrum, Meyer *et al.* [45] proposed a registration algorithm based on a thin-plate spline deformation guided by a voxel-based similarity measure using mutual information. Their algorithm is confined to a limited number of degrees of freedom because of the prohibitive computational complexity of the thin-plate spline warps. Since then, B-spline-based free-form deformation using mutual information (or its variance) as the similarity measure, becomes more and more viable in nonrigid registration schemes [76, 69, 6].

Later, Wang *et al.* [100] further proposed a nonrigid registration scheme of brain MRI, which employs non-uniform rational B-spline (NURBS) as its mathematic foundation instead of B-splines. However, the nature deficiency of family of tensor product B-spline is that they can only represent genus-zero object without tedious trimming and patching operation.

In stead, we propose a novel nonrigid volume registration framework using multiresolution volumetric simplex spline-based free-form deformation to address the above difficulty. Volumetric simplex splines, the 3D case of general simplex splines, have many attractive properties such as piecewise polynomials over general tetrahedral domains, local support, higher-order smoothness, and positivity, making them potentially ideal in volume representation, visualization and analysis [21].

As depicted in *Figure 5.1*, the pipeline of our framework can be summarized as follows. We first establish the volumetric simplex spline volume for the floating volume and embed the floating volume into the control space. In the global transformation part, we first conduct a rigid affine transformation to the floating volume with the guidance from normalized mutual information (E_{NMI}), both of which employ the volumetric simplex spline as their mathematic foundation. In the local deformation part, we further exploit the merits of multiresolution volumetric simplex splines and integrate volume similarity term (E_{NMI}), volume preserving term (E_{Volume}) and smoothness term (E_{Smooth}) into our framework to achieve more efficiency, flexibility and accuracy. The developed framework is fully automated without human intervention.

Our contributions in this chapter can be summarized as follows

- We develop a unified volume registration scheme which incorporates global transformation and local deformation into the scheme using multiresolution volumetric simplex spline-based free-form deformation. With less degree of freedom, our multiresolution volumetric simplex spline volumes exhibit more local control capability than other tensor product B-splines volumes.
- By applying normalized mutual information, smoothness term, and volume-preserving

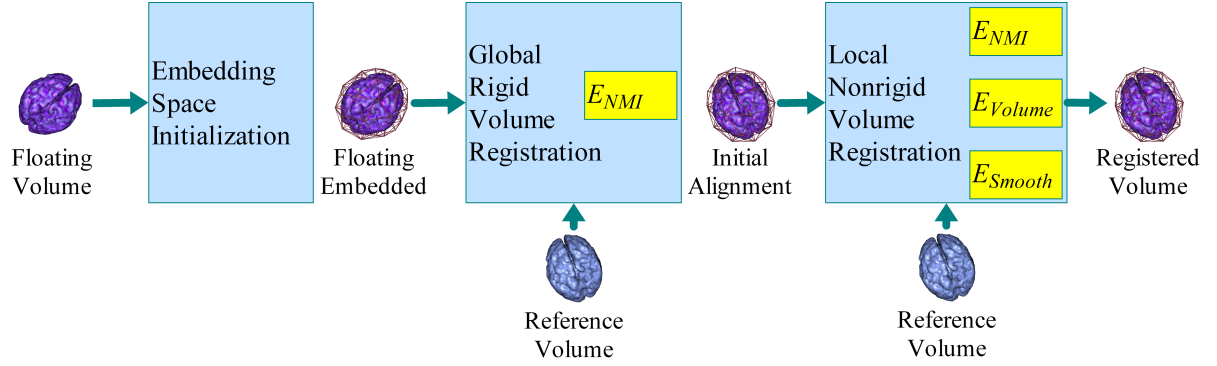


Figure 4.1: Illustration of the pipeline of our nonrigid registration framework. The rectangles inside the pipeline indicate tasks, and the icons with text under them denote the inputs and outputs of tasks. The text boxes inside the task denote the cost functions which fulfill the task.

terms into the free-form deformation, our local deformation model is capable of further minimizing the volume difference between the two volumes and achieving high fidelity. Our experiments exhibit the efficacy and robustness of our volume-preserving volume registration scheme.

- We apply the multiresolution simplex spline-based free-form deformation in the brain volume registration. The experimental results demonstrate the efficacy and accuracy of our nonrigid volume registration paradigm. Although we mainly focus on brain MRI volumes registration in this study, our method can be generally applied to other inter-modality and intramodality volumes registration.

4.2 Previous Work

This chapter is related to the theory and application of volumetric simplex splines, and free-from deformation. And the application we focus in this study is brain volume registration. This section reviews the related, previous work in these fields which are not presented in the introduction part.

4.2.1 Volumetric Simplex Splines

Multivariate simplex splines were first presented by Boor [14]. In essence, multivariate simplex splines are the volumetric projection of higher dimensional simplices onto a lower dimensional space \mathbb{R}^m . From the point of view of blossoming, Dahmen *et al.* [13] proposed triangular B-splines. Later, Greiner and Seidel [21] demonstrated their practical feasibility in graphics and shape design. Pfeifle and Seidel developed a faster evaluation technique for quadratic bivariate DMS-spline surfaces [59] and applied it to the scattered data fitting of triangular B-spline [61]. Hua and Qin presented a volumetric sculpting framework that employs trivariate scalar nonuniform B-splines as underlying representation [27, 29]. More recently, they applied trivariate simplex splines to the representation of solid geometry, the modeling of heterogeneous material attributes, and the reconstruction of continuous volumetric splines from discretized volumetric inputs via data fitting [25, 26]. Tan *et al.* applied the hierarchical simplex splines to volume reconstruction from planar images [87]. Later they proposed dynamic spherical volumetric simplex splines and successfully applied the volume representation scheme to brain biomedical behavior simulation [89].

4.2.2 Brain Volume Registration

On the application front, in recent years, tremendous efforts from biomedical research communities have been devoted into the brain volume registration since accurate registration of brain can have many potential applications, e.g., computer-aided surgical planning/surgery, computer-assisted disease/injury positioning, accurate radiation therapy, and many other medical benefits. We only review several of them in the interest of space. In [84], Studholme *et al.* demonstrated the efficacy of measures of voxel intensity similarity in automatic registration of brain volumes derived from magnetic resonance imaging and positron emission tomography (PET). Liu *et al.* presented the method which employs mutual information matrix for high-dimensional mutual information registration of intermodality brain volumes [37]. Myers summarized the application of PET-MR brain volume registration [49].

4.3 Volumetric Simplex Splines

First, let us review some content of the volumetric simplex splines, the mathematic model deployed in our free-form based nonrigid registration.

A degree n volumetric simplex spline, $M(\mathbf{x}|\mathbf{x}_0, \dots, \mathbf{x}_{n+3})$, can be defined as a function of $\mathbf{x} \in \mathbb{R}^3$ over the half open convex hull of a point set $\mathbf{V} = [\mathbf{x}_0, \dots, \mathbf{x}_{n+3})$, depending on the $n + 4$ knots $\mathbf{x}_i \in \mathbb{R}^3, i = 0, \dots, n + 3$. The volumetric simplex splines may be formulated recursively. When $n = 0$,

$$M(\mathbf{x}|\mathbf{x}_0, \dots, \mathbf{x}_3) = \begin{cases} \frac{1}{|\text{Vol}_{\mathbb{R}^3}(\mathbf{x}_0, \dots, \mathbf{x}_3)|}, & \mathbf{x} \in [\mathbf{x}_0, \dots, \mathbf{x}_3), \\ 0, & \text{otherwise,} \end{cases}$$

and when $n > 0$, select four points $\mathbf{W} = \{\mathbf{x}_{k_0}, \mathbf{x}_{k_1}, \mathbf{x}_{k_2}, \mathbf{x}_{k_3}\}$ from \mathbf{V} , such that \mathbf{W} is affinely independent, then

$$M(\mathbf{x}|\mathbf{x}_0, \dots, \mathbf{x}_{n+3}) = \sum_{j=0}^3 \lambda_j(\mathbf{x}|\mathbf{W}) M(\mathbf{x}|\mathbf{V} \setminus \{\mathbf{x}_{k_j}\}), \quad (4.1)$$

where $\sum_{j=0}^3 \lambda_j(\mathbf{x}|\mathbf{W}) = 1$ and $\sum_{j=0}^3 \lambda_j(\mathbf{x}|\mathbf{W}) \mathbf{x}_{k_j} = \mathbf{x}$.

The directional derivative of $M(\mathbf{x}|\mathbf{V})$ with respect to a vector \mathbf{d} is defined as follows

$$D_{\mathbf{d}}M(\mathbf{x}|\mathbf{V}) = n \sum_{j=0}^3 \mu_j(\mathbf{d}|\mathbf{W}) M(\mathbf{x}|\mathbf{V} \setminus \{\mathbf{x}_{k_j}\}), \quad (4.2)$$

where $\mathbf{d} = \sum_{j=0}^3 \mu_j(\mathbf{d}|\mathbf{W}) \mathbf{x}_{k_j}$ and $\sum_{j=0}^3 \mu_j(\mathbf{d}|\mathbf{W}) = 0$.

The basis functions of normalized volumetric simplex splines are then defined as

$$N_{\beta}^I(\mathbf{u}) = |\det(\mathbf{p}_i, \mathbf{q}_j, \mathbf{r}_k, \mathbf{s}_l)| M(\mathbf{u}|V_{\beta}^I), \quad (4.3)$$

where the β denotes the traverse of 4-tuple $(i, j, k, l), i + j + k + l = n$, and I denotes one tetrahedron in domain \mathbf{T} .

The simplex spline volume is the combination of a set of basis functions with control points

\mathbf{c}_β^I

$$\mathbf{s}(\mathbf{u}) = \sum_{I \in \mathbf{T}} \sum_{|\beta|=n} \mathbf{c}_\beta^I N_\beta^I(\mathbf{u}). \quad (4.4)$$

Figure 4.2-(a) shows a cubic volumetric simplex spline domain which is naturally an icosahedron. Figure 4.2-(b) exhibits the corresponding volumetric simplex spline solid.

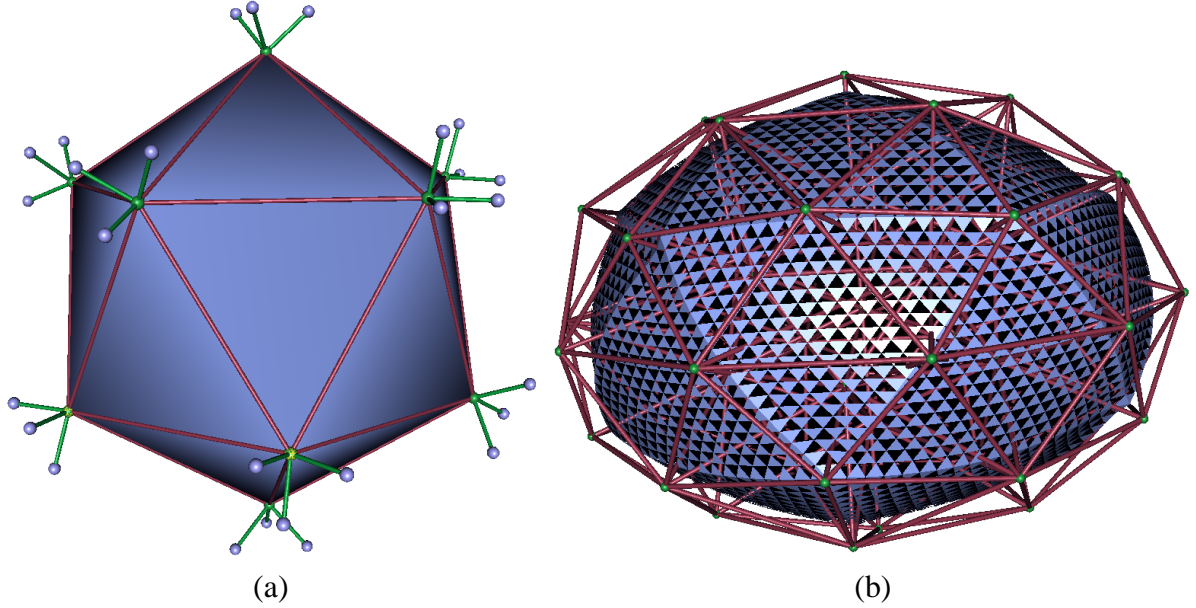


Figure 4.2: (a) A cubic volumetric simplex spline domain with knots associated; (b) The control solid defined over (a). The tetrahedra of the control solid are scaled in order to emphasize its non-empty solid interior geometry.

In the interest of space, readers may refer to [25] [89] for a complete description of volumetric simplex splines.

4.4 Embedding Space Initialization

As we stated in the introduction part, we first embed the floating volume into the embedding space, i.e., the control space associated to the volumetric simplex spline volume. In this section, we articulate the preparatory step before the registration step: domain and control space initialization.

4.4.1 Simplex Spline Initialization

We employ the method described in [89] to create the spherical volumetric simplex domain. Admittedly, we can choose any canonic shape as the domain. We prefer sphere domain since the human brain is topologically equivalent to a sphere and the tetrahedralization of a sphere domain is more uniform than any other genus-zero primitives such as cube and cylinder. In practice, we find that a cubic simplex spline with domain derived from the icosahedron suffices our registration purpose. *Figure 4.2* illustrates the domain and initial control space we employed in our framework.

4.4.2 Floating Volume Embedding

The control solid illustrated in *Figure 4.2-(b)* serves as the embedding space. In order to achieve better performance from the framework, however, we need to take the following two requirements into account in practice.

1. The embedding space should have a uniform mesh configuration at the initialization.

A uniform embedding space can tremendously reduce the computational time and increase the registration efficiency. While multiresolution structure is needed to further decrease the registration error, uniform mesh configuration of the embedding space will exhibit its great potentiality.

2. The embedding space should completely contain the floating volume. When the boundary of the control net is convex, the control space of simplex spline volume should be within the control net, i.e., the control space should never reach the control net. Correspondingly, the embedded objects should be within the control space completely. *Figure 4.3-(a)* illustrates the 2D case of this phenomenon.

Observing all the above-mentioned aspects, *Figure 4.3-(b)* illustrates the final control space with the floating brain volume embedded. Note that the brain is within the boundary of the control space, which is demonstrated as the scaled solid in *Figure 4.2-(b)*.

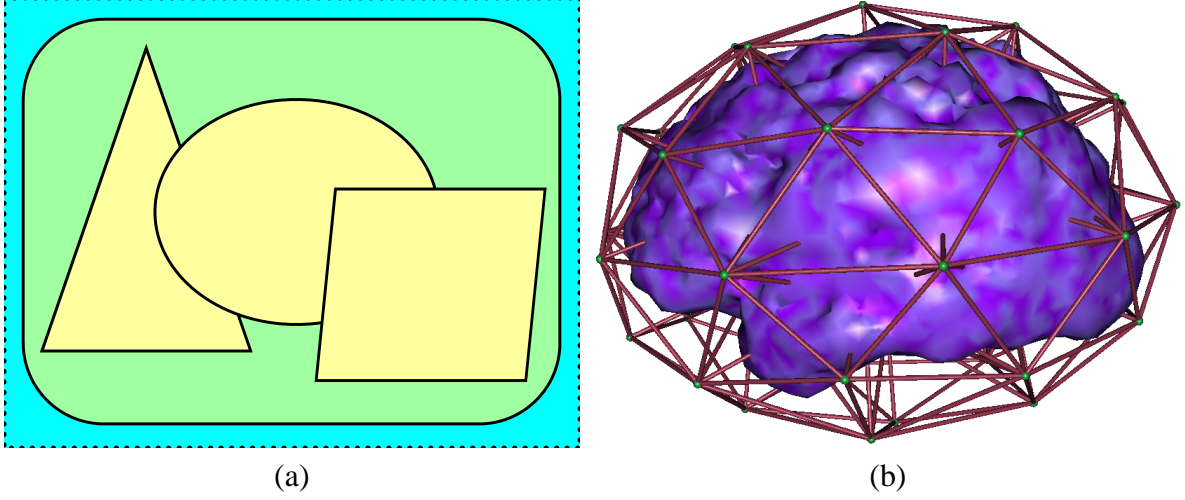


Figure 4.3: (a) The relationship among the control net, the control space and the embedded objects. The dotted line of the blue rectangle denotes the boundary of a control net, the green rounded-corner rectangle denotes the control space with three yellow objects embedded; (b) The embedding space with the floating brain volume embedded. In the figure, the blue tetrahedra mesh denotes the control net while the green dots denote the control points.

4.5 Volume Registration Problem Statement

The objective of volume registration of two volumes, \mathbf{A} and \mathbf{B} (without loss of generality, say, we register \mathbf{A} to \mathbf{B}), is to find the optimal transformation: $T : (x, y, z) \mapsto (x', y', z')$ which maps the point (x, y, z) in volume \mathbf{A} to (x', y', z') in volume \mathbf{B} . In general, the motion of the floating volume is distinct so that rigid affine transformation is not sufficient for the purpose. As we employ volumetric simplex spline as the volume representation scheme, now the floating volume is expressed as

$$s(\mathbf{u}, \mathbf{c}) = \sum_{I \in \mathbf{T}} \sum_{|\beta|=n} \mathbf{c}_{\beta}^I N_{\beta}^I(\mathbf{u}), \quad (4.5)$$

where we put the \mathbf{c} into the parameter position of function s , to emphasize the volumetric simplex spline volume s is now not only the function of \mathbf{u} , but the function of \mathbf{c} . Hence we can rewrite the objective function in the following way. Let $s_{\mathbf{A}} = s(\mathbf{u}, \mathbf{c}_{\mathbf{A}})$ be the floating volume \mathbf{A} where $\mathbf{c}_{\mathbf{A}}$ is the control points of the control net of the volumetric simplex spline volume, and $s_{\mathbf{B}}$ be the reference volume \mathbf{B} in the same manner, now the objective of volume registration is to find the optimal transformation: $T : \mathbf{c}_{\mathbf{A}} \mapsto \mathbf{c}_{\mathbf{A}'}$ where $s(\mathbf{u}, \mathbf{c}_{\mathbf{A}'})$ and $s_{\mathbf{B}}$ have

the most correlation.

4.6 Global Transformation Model

Global transformation aims at providing the rough alignment between s_A and s_B since non-rigid volume registration schemes requires the rough shape of the two to-be-registered volumes, i.e, large deformation between the two volumes will fail the volume registration algorithm using local free-from deformation method. As we illustrated in the introduction part, here we employ the rigid affine transformation to achieve the global deformation. The objective function is to maximize the normalized mutual information between $R(s(u, c_A))$ and s_B , where R is the rigid affine transformation. Note that we take the advantage of $R(s(u, c_A)) = s(u, R(c_A))$ from the property of volumetric simplex spline.

4.7 Local Deformation Model

The globe deformation only describes the global motion of the floating brain volume, and it only yields the rough shape of from s_A to s_B . Hence a local deformation, which models the local deformation of the floating brain, is required. Here we employ an free-from deformation model based on volumetric simplex splines, to achieve the local deformation. Here the basic idea of local deformation, is to embed the to-be-deformed volume into the embedding space, and then to deform the brain by maneuvering an underlying mesh of control points. Please refer to *Chapter 4.4.2* for the detailed embedding techniques. More details of local deformation model will be given in *Chapter 4.7.1*.

4.7.1 Volume-Preserving Local Deformation

Our local deformation algorithm employs NMI similarity measure E_{NMI} , volume preserving penalty term E_{Volume} , and smoothness penalty term E_{Smooth} to constrain the local deformation within the embedding space. The registration cost function is as follows

$$E_{total} = aE_{NMI} - bE_{Volume} - cE_{Smooth}, \quad (4.6)$$

where a , b and c are user-specified coefficients controlling the relative influence of E_{NMI} , E_{Volume} and E_{Smooth} , respectively. The signs, $+$ and $-$ before each term denote that during the local deformation, we want to maximize the similarity measure E_{NMI} , and minimize two penalties E_{Volume} and E_{Smooth} . We will explain later in this section why each term bears the sign $+$ or $-$.

4.7.2 Normalized Mutual Information Measure

To measure the degree of alignment between the reference volume and the floating volume, one preliminary step is to define a similarity criterion. One of the widely-used voxel-based similarity measures is the sum of squared difference (SSD). Yet same part of human body may have different image intensities in different imaging modalities, which makes SSD insufficient in intermodality volume registration. Alternatively, we employ mutual information (MI) [11, 99] in our framework, which has been shown to align volumes from different modalities accurately and robustly.

MI, denoted by $I(\mathbf{s}_A, \mathbf{s}_B)$, is the measurement of the degree of dependence between two volumes, \mathbf{s}_A and \mathbf{s}_B , respectively. It is measured through the distance between the joint distribution and the the distribution associated to the case of complete independence, by means of Kullback-Leibler measure [98] as follows

$$I(\mathbf{s}_A, \mathbf{s}_B) = H(\mathbf{s}_A) + H(\mathbf{s}_B) - H(\mathbf{s}_A, \mathbf{s}_B), \quad (4.7)$$

where $H(\mathbf{s}_A)$ and $H(\mathbf{s}_B)$ denote the marginal entropies of \mathbf{s}_A and \mathbf{s}_B respectively, and $H(\mathbf{s}_A, \mathbf{s}_B)$ denotes their joint entropy. Those entropy quantities can be calculated as follows

$$H(\mathbf{s}_A) = - \sum_a p_{\mathbf{s}_A}(a) \lg p_{\mathbf{s}_A}(a), \quad (4.8)$$

$$H(\mathbf{s}_A, \mathbf{s}_B) = - \sum_{a,b} p_{\mathbf{s}_A, \mathbf{s}_B}(a, b) \lg p_{\mathbf{s}_A, \mathbf{s}_B}(a, b), \quad (4.9)$$

where $p_{\mathbf{s}_A}(a)$ indicates the marginal probability distribution of \mathbf{s}_A and $p_{\mathbf{s}_A, \mathbf{s}_B}(a, b)$ indicates the joint probability distribution of \mathbf{s}_A and \mathbf{s}_B .

If the two volumes are registered, $I(\mathbf{s}_A, \mathbf{s}_B)$ reaches its maximal. Studholme [85] has shown that $I(\mathbf{s}_A, \mathbf{s}_B)$ is dependant on the overlap between the two volumes. To avoid any dependency on the amount of image overlap, in our framework, we will employ normalized mutual information (NMI) [85] as the measurement of the degree of volume registration as follows

$$E_{NMI} = \frac{H(\mathbf{s}_A) + H(\mathbf{s}_B)}{H(\mathbf{s}_A, \mathbf{s}_B)}. \quad (4.10)$$

Similarly here, if the two volumes are registered, E_{NMI} reaches its maximal. Hence in Equation 4.6 E_{NMI} has the positive sign. Similar forms of normalized mutual information have been proposed by Maes *et al.* [38].

4.7.3 Volume-Preserving Term

The volume-preserving constraint is based on the biomedical observation that many tissues in the human body, for instance, the human brain, are approximately incompressible for small deformations and short time periods.

The volume-preserving term is purely geometry related. As stated in Chapter 4.3, the dimension of \mathbf{s} is the same as the generalized control point \mathbf{c}_β^I . For the simplicity of the formula expression, let $\mathbf{s} = (s_x, s_y, s_z)$ to emphasize the pure geometry extracted from \mathbf{s} , where the subscript denotes the component. In a small neighborhood of the point (x, y, z) , which has the parametric value \mathbf{u} , the local compression caused by the deformation can be calculated in terms of the Jacobian determinant as follows

$$\mathbf{J}(\mathbf{u}) = \det \begin{pmatrix} \frac{\partial s_x(\mathbf{u})}{\partial x} & \frac{\partial s_x(\mathbf{u})}{\partial y} & \frac{\partial s_x(\mathbf{u})}{\partial z} \\ \frac{\partial s_y(\mathbf{u})}{\partial x} & \frac{\partial s_y(\mathbf{u})}{\partial y} & \frac{\partial s_y(\mathbf{u})}{\partial z} \\ \frac{\partial s_z(\mathbf{u})}{\partial x} & \frac{\partial s_z(\mathbf{u})}{\partial y} & \frac{\partial s_z(\mathbf{u})}{\partial z} \end{pmatrix}. \quad (4.11)$$

The value $\mathbf{J}(\mathbf{u})$ equals to 1.0 if the deformation at \mathbf{u} is volume-preserving, greater than 1.0 if there is local expansion, and less than 1.0 if there is local compression.

Now according to the directional derivative of $M(\mathbf{x}|\mathbf{V})$ with respect to a vector \mathbf{d} defined in *Equation 4.2*, the directional derivative of the basis functions of normalized simplex splines with respect to a vector \mathbf{d} is defined as

$$D_{\mathbf{d}}N_{\beta}^I(\mathbf{u}) = |\det(\mathbf{p}_i, \mathbf{q}_j, \mathbf{r}_k, \mathbf{s}_l)|D_{\mathbf{d}}M(\mathbf{u}|V_{\beta}^I). \quad (4.12)$$

In the interest of space, readers may refer to *Equation 4.3* for the details of each term in this equation. Similarly, the directional derivative of a simplex spline volume of degree n is defined as

$$D_{\mathbf{d}}\mathbf{s}(\mathbf{u}) = \sum_{I \in \mathbf{T}} \sum_{|\beta|=n} \mathbf{c}_{\beta}^I D_{\mathbf{d}}N_{\beta}^I(\mathbf{u}). \quad (4.13)$$

Now the Jacobian determinant can be computed as

$$\mathbf{J}(\mathbf{u}) = \det \begin{pmatrix} D_{(1,0,0)}\mathbf{s}(\mathbf{u}) \\ D_{(0,1,0)}\mathbf{s}(\mathbf{u}) \\ D_{(0,0,1)}\mathbf{s}(\mathbf{u}) \end{pmatrix}. \quad (4.14)$$

Then incompressibility constraint term is defined as the integral of the absolute logarithm of the Jacobian determinant, integrated over the domain Ω

$$E_{Volume} = \int_{\Omega} |\log(\mathbf{J}(\mathbf{u}))| d\mathbf{u}. \quad (4.15)$$

From the above equation, we observe that E_{Volume} is non-negative. If there is no local volume variation and E_{Volume} reaches its minimal, 0. Hence in *Equation 4.6* E_{Volume} has the negative sign.

4.7.4 Smoothness Term

We further constrain the deformation to be smooth by adding another penalty term, thin plate spline-based bending energy [4]. In our scheme, this penalty quantity is the 3D counterpart of the 2D one. Here the penalty term is composed of second-order derivatives of the deformation as follows

$$E_{Smooth} = \int_{\Omega} \left(\frac{\partial^2 \mathbf{s}_x}{\partial x^2} + \frac{\partial^2 \mathbf{s}_y}{\partial y^2} + \frac{\partial^2 \mathbf{s}_z}{\partial z^2} \right) + 2 \times \left[\left(\frac{\partial \mathbf{s}_x}{\partial x} \frac{\partial \mathbf{s}_y}{\partial y} \right)^2 + \left(\frac{\partial \mathbf{s}_y}{\partial y} \frac{\partial \mathbf{s}_z}{\partial z} \right)^2 + \left(\frac{\partial \mathbf{s}_z}{\partial z} \frac{\partial \mathbf{s}_x}{\partial x} \right)^2 \right] d\mathbf{u}. \quad (4.16)$$

Similar to the volume-preserving term, the smoothness term is also purely geometry related. According the recurrence relation of basis function M , along with its derivation rule [46] of the high order derivative, the second order derivative of $M(\mathbf{x}|\mathbf{V})$ with respect to a vector \mathbf{d} is defined as follows

$$D_{\mathbf{d}}^2 M(\mathbf{x}|\mathbf{V}) = n \sum_{j=0}^3 \mu_j(\mathbf{d}|\mathbf{W}) D_{\mathbf{d}} M(\mathbf{x}|\mathbf{V} \setminus \{\mathbf{x}_{k_j}\}), \quad (4.17)$$

where $\mathbf{x} = \sum_{j=0}^3 \mu_j(\mathbf{d}|\mathbf{W}) \mathbf{x}_{k_j}$ and $\sum_{j=0}^3 \mu_j(\mathbf{d}|\mathbf{W}) = 0$. Now the second order derivative of the basis functions of normalized simplex splines with respect to a vector \mathbf{d} is defined as

$$D_{\mathbf{d}}^2 N_{\beta}^I(\mathbf{u}) = |\det(\mathbf{p}_i, \mathbf{q}_j, \mathbf{r}_k, \mathbf{s}_l)| D_{\mathbf{d}}^2 M(\mathbf{u}|V_{\beta}^I). \quad (4.18)$$

Similarly, the second order derivative of a simplex spline volume of degree n is defined as

$$D_{\mathbf{d}}^2 \mathbf{s}(\mathbf{u}) = \sum_{I \in \mathbf{T}} \sum_{|\beta|=n} \mathbf{c}_{\beta}^I D_{\mathbf{d}}^2 N_{\beta}^I(\mathbf{u}). \quad (4.19)$$

Now the second-order derivative of the deformation can be easily computed as, e.g.,

$$\frac{\partial^2 \mathbf{s}_x}{\partial x^2} = [D_{(1,0,0)}(D_{(1,0,0)}\mathbf{s}(\mathbf{u}))]_x. \quad (4.20)$$

Other entries in *Equation 4.16* can be computed in the same manner.

Note that the penalty term is zero for any affine transformations and it only penalize non-affine transformations. Hence in *Equation 4.6* E_{Smooth} has the negative sign.

4.8 Multiresolution Volumetric Simplex Splines

For some regions with very large deformations, it is often desirable to introduce extra degrees of freedom into the spline representation in order to improve the registration quality. However, current tensor product B-spline representations will introduce more unnecessary degree of freedom. The 2D case of this limit is shown in *Figure 4.4-(a)*. In sharp contrast to it, multiresolution volumetric simplex splines are more suitable for this purpose because of its non-tensor product nature and true local support property. The 2D case of this merit is depicted in *Figure 4.4-(b)*.

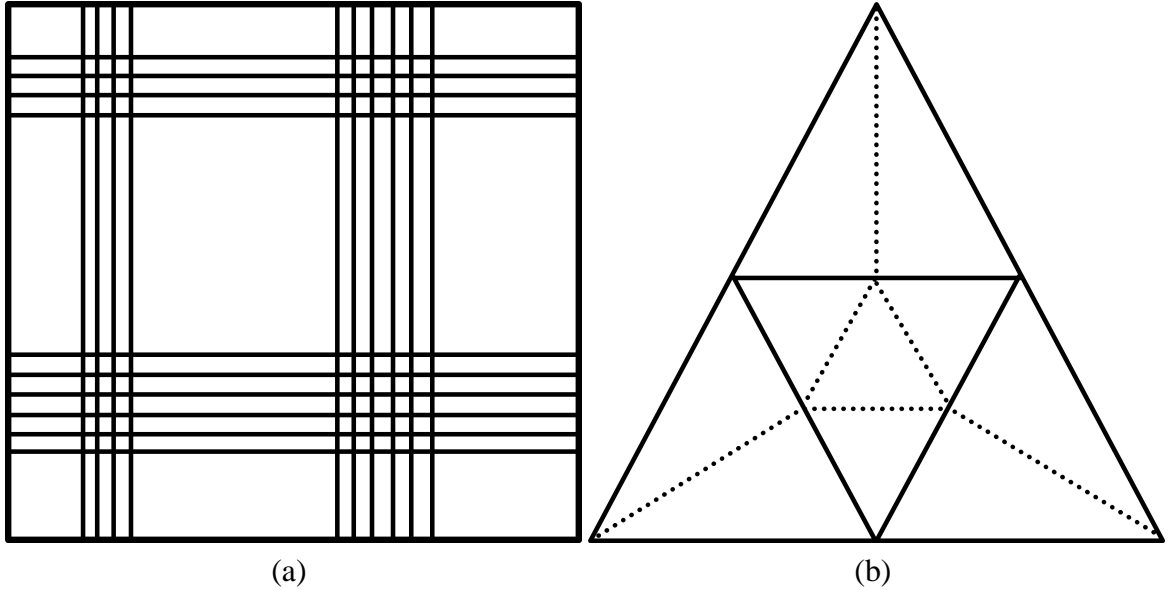


Figure 4.4: (a) Multiresolution tensor product B-splines. While increasing the resolution of region of interest, other regions are affected because of its tensor product nature; (b) Multiresolution simplices. True local support can be steadily achieved because of its non-tensor product nature.

Before we introduce the multiresolution volumetric simplex splines, let us first review some results on a triangular B-spline.

Theorem (Piecewise polynomial representation) [80] Let F be any piecewise polynomial of degree n over a given triangulation T , and let F_I be the restriction of F to the triangle $\Delta(I)$ and f_I be the polar form of F_I . Then the following identity holds for all \mathbf{u}

$$F(\mathbf{u}) = \sum_{I \in T} \sum_{|\beta|=n} f_I() N_{\beta}^I(\mathbf{u}). \quad (4.21)$$

For more information about polar form, we refer the readers to [79, 80].

The above theorem holds for a general $s(\geq 2)$ -variate simplex spline. Let I be the tetrahedron of interest in the domain of $s(\mathbf{u})$, and we want to add more degrees of freedom in I to model the large deformation. There are two different ways to solve this problem. The first is knot insertion, in which one knot is inserted into the tetrahedron I , and I is subdivided into four tetrahedra. Multiple knots can be inserted one by one. The second is multiresolution structure, whose domain is a regularly subdivided tetrahedra of I . The major differences between knot insertion and multiresolution structures (see *Figure 4.5*) are as follows

- Multiresolution structures do not change the original spline $s(\mathbf{u})$, while knot insertion does affect the spline $s(\mathbf{u})$.
- Multiresolution structures need special technique to maintain certain continuity between the original spline and new spline, while knot insertion does not.
- Multiresolution structures would not introduce poor quality tetrahedra, while knot insertion does so inevitably, which should be avoided in the implementation.

If the registration error metric, i.e., the difference of NMI inside a tetrahedron I is greater than a user-specified value, we construct the multiresolution volumetric simplex spline as follows

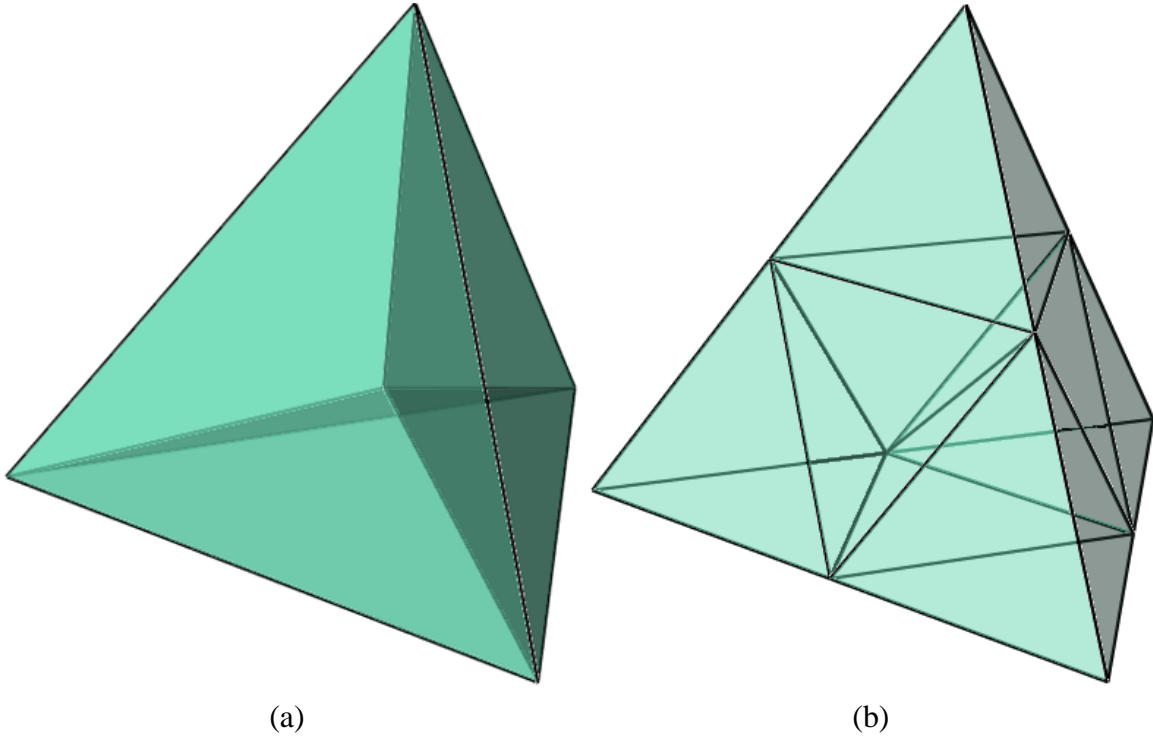


Figure 4.5: (a) Knot insertion. After one knot is inserted at the barycenter of the original tetrahedron, the original one is subdivided into four tetrahedra; (b) Multiresolution simplices. After knots are inserted at the center of the edges of the original tetrahedron, the original one is subdivided into eight tetrahedra.

1. Subdivide the I into eight tetrahedra, as shown in *Figure 4.5-(b)*.
2. Assign sub-knots to the newly inserted primary knots, according to the rule of domain validity [25].
3. Subdivide the each direct neighbor tetrahedron into four tetrahedra, as shown in *Figure 4.4-(b)*.
4. Compute the initial position of control points by subdividing the control net into a second level.

As the tetrahedralization of the multiresolutional of I will not affect the original spline, we maintain C^{n-1} -continuity between the newly added tetrahedra and original ones.

4.9 Experimental Results

We implemented the framework on a Dell XPS4700 desktop with Quad Cores 2.84GHz CPU and 4GB RAM. The system is written in VC++ and VTK 4.6. In our intensive experiments, we discovered that the second level multiresolution volumetric simplex spline can achieve better registration accuracy than a the first level configuration. The configuration of the multiresolution volumetric simplex spline and embedding space is depicted in *Table 4.1*. As we can see from the table, from first-level to second-level, the number of control points is increased correspondingly. Hence more degrees of freedom will be introduced to the system, which is more capable of registering volumes with large deformation.

First-level Configuration			
	# of Tetrahedra	# of Knots	# of Control Points
Quadratic	20	39	55
Cubic	20	52	147
Second-level Configuration			
	# of Tetrahedra	# of Knots	# of Control Points
Quadratic	160	165	309
Cubic	160	220	903

Table 4.1: Statistics of multiresolution volumetric simplex spline domain and control space configuration.

To measure the performance of our proposed algorithm, we also compared the registration quality obtained using our multiresolution volumetric simplex spline-based free-form deformation (MVSS-FFD) and the existing registration algorithm using tensor product B-spline-based free-form deformation (TPBS-FFD) [69], respectively. A comparison of the runtime was also performed between our MVSS-FFD method and existing TPBS-FFD method. Detailed experimental results will be presented in the following sections.

4.9.1 Experiments on Simulated Brain Volumes

We conducted experiments on several intramodality brain volumes registration. Due to the difficulty to produce known nonrigid motion fields in the tissues of brain, we created several

deformed volumes by applying the brain modeling and simulation techniques with dynamic spherical volumetric simplex splines [89]. We prefer such techniques for two reasons. First, the mathematic foundation of the simulation scheme is also the volumetric simplex spline volume, the same with our volume registration paradigm; Second, the simulated brain volume is validated with the ground true. The simulated brain volumes have been chosen as the references images respectively.

Figure 4.6 illustrates one case study in which the subject is lying on his/her left side. We also conduct the comparison with the results obtained from tensor product B-spline-based free-form deformation. In order to better visualize the deformation field of the volumes, one axial cross section view of each volume was presented.

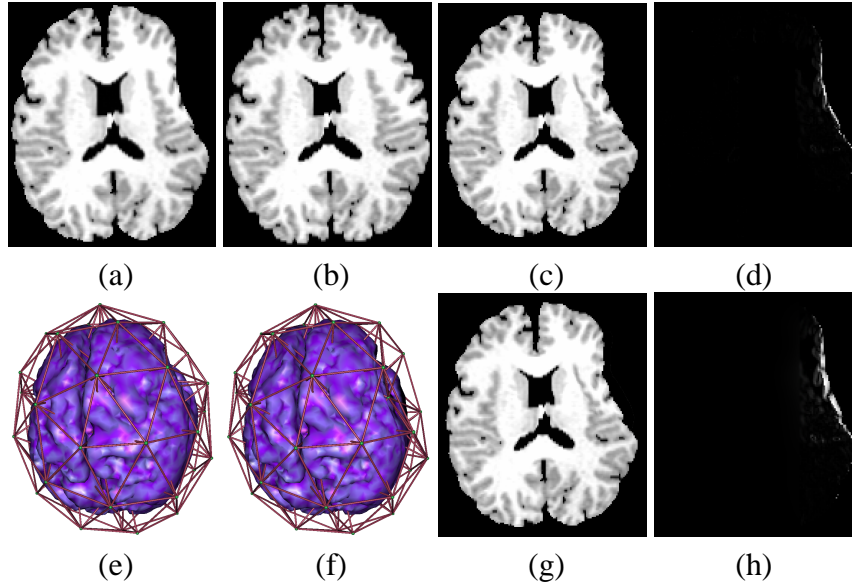


Figure 4.6: One case study. (a) The reference brain volume; (b) The floating volume to be registered to (a); (c) The registered volume using our MVSS-FFD method; (d) The image difference between (a) and (c); (e) The control space before registration; (f) The control space after registration; (g) The registered volume using existing TPBS-FFD method; (h) The image difference between (a) and (g).

Figure 4.7 illustrates another case study in which the subject is lying on his/her right side.

Note that, in *Figure 4.6* and *Figure 4.7*, since the floating and reference volumes are all acquired from the same imaging modality, MRI, the misregistration can be directly presented

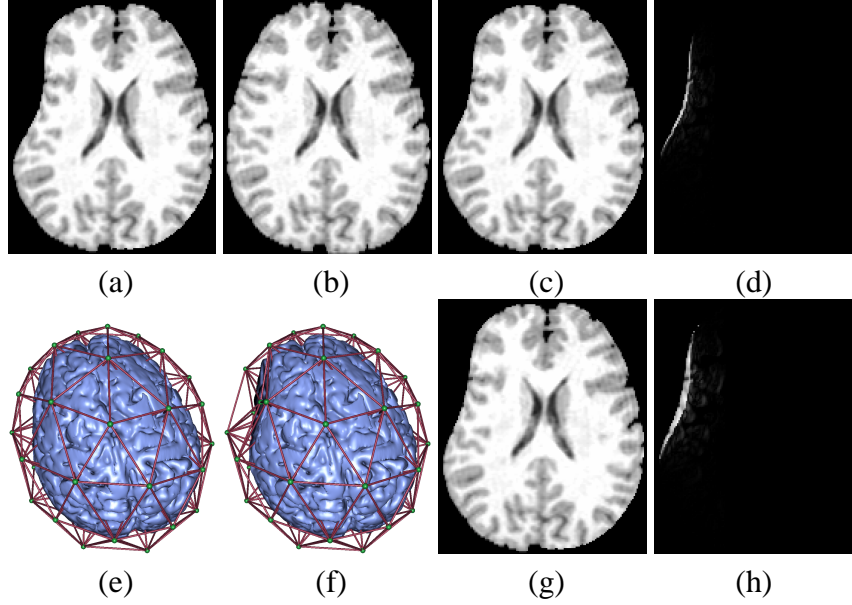


Figure 4.7: Another case study. (a) The reference brain volume; (b) The floating volume to be registered to (a); (c) The registered volume using our MVSS-FFD method; (d) The image difference between (a) and (c); (e) The control space before registration; (f) The control space after registration; (g) The registered volume using existing TPBS-FFD method; (h) The image difference between (a) and (g).

as the image difference between the two volumes. The results shows that our MVSS-FFD paradigm can achieve better outcome than TPBS-FFD method.

4.9.2 Comparison with Existing Algorithms

As the *Equation 4.6* has no analytic solution, we employ gradient descent method [82] to solve it. Average runtime between our MVSS-FFD registration for one paired volumes is 38 minutes, while existing TPBS-FFD method needs 1 hour and 36 minutes to accomplish the job. The improvement is greatly attributed to the non-tensor, truly local support properties of volumetric simplex splines, thus less degree of freedom is involved in the system. Detailed comparison is list in *Table 4.2*. The comparison between the runtime consumed by our MVSS-FFD method and existing TPBS-FFD method, demonstrates that our paradigm is more efficient.

Quantitative measure of the registration results between our MVSS-FFD method and TPBS-FFD method are listed in *Table 4.3*.

	MVSS-FFD	TPBS-FFD
Embedding Space	MVSS Control Space	12^3 Uniform Grid
# of Control Points	903	1728
Degree of Freedom	2709	5184
Runtime (hh:mm)	00:38	01:36

Table 4.2: Statistics of runtime comparison between the registration approaches using our multiresolution volumetric simplex spline-based free-form deformation and regular free-form deformation using tensor product B-spline scheme. Note that the degree of the domain is cubic in both cases.

Patient ID	NMI before Simulation	NMI from TPBS-FFD	NMI from MVSS-FFD	Registration Enhancement
A	1.865863	1.840674	1.856525	0.015851
B	1.959156	1.925738	1.945176	0.019438
C	1.920168	1.884962	1.913941	0.028979
D	1.881957	1.853549	1.862940	0.009391
E	1.844318	1.803465	1.834528	0.031063
F	1.936534	1.909266	1.920119	0.010853

Table 4.3: Statistics of registration results using our MVSS-FFD method with comparison to TPBS-FFD method. The registration quality is evaluated using the normalized mutual information between the resulting floating brain volume and the reference brain volume.

4.10 Comparison with Existing Methods

In this section, we will briefly compare our volume registration paradigm with other volume registration schemes. As there are quite a lot literature on this research topic, I only choose several of them as the representative ones.

Authors	Method	Nonrigid	High-Genus Support
Studholme <i>et al.</i> [84]	Voxel Intensity Similarity	No	Not Applicable
Rueckert <i>et al.</i> [76]	B-Spline Based Free-Form Deformation	Yes	Trimming and Patching
Wang <i>et al.</i> [100]	NURBS Based Free-Form Deformation	Yes	Trimming and Patching
Our Method	Multivariate Simplex Spline Based Free-Form Deformation	Yes	Naturally Supportive

Table 4.4: Comparison of volume registration schemes.

As we may see from the table, similarity measure is inadequate for volume registration although it is frequently employed as part of the solution. Most of current research on volume registration is based on free-form deformation. Although B-spline is widely used in this research domain, it is computational inefficient to register high-genus models because of its tensor product nature. On the other end of the spectrum, our unrival volume registration scheme is based on multivariate simplex spline which is a true non-tensor product method with natural high-genus support.

4.11 Summary

In this chapter, a novel nonrigid volume registration paradigm using multiresolution volumetric simplex spline-based free-form deformation has been proposed. Although volumetric simplex has already been a powerful tool in both engineering and medical research realm, it has never been applied to the intramodality or intermodality nonrigid volume registration. Our approach first embeds the floating volume into the control space associated with its volumetric simplex spline. With the guidance of normalized mutual information between the floating and reference volume, a rigid affine transformation is applied to the control points of the control space, to obtain an initial rigid alignment. After that, a local, nonrigid, multiresolution volumetric simplex spline-based free-form deformation is applied to the floating volume. We introduce volume similarity term, volume preserving term and smoothness term to our framework to achieve better registration result. Multiresolution simplices greatly reduce the degree of the freedom of the system, increase the registration quality and shorten the computational time. The experimental results have demonstrated the excellent performance of our technique, which can be effectively employed to brain volume registration as well as other intramodality and intermodality medical imaging registration.

CHAPTER 5:

PHYSICALLY BASED MODELING AND SIMULATION WITH DYNAMIC SPHERICAL MULTIVARIATE SIMPLEX SPLINES

In this chapter, we present a novel computational modeling and simulation framework based on dynamic spherical multivariate simplex splines (DSMSS). The framework can handle the modeling and simulation of genus-zero objects with real physical properties. In this framework, we first develop an accurate and efficient algorithm to reconstruct the high-fidelity digital model of a real-world object with spherical multivariate simplex splines which can represent with accuracy geometric, material, and other properties of the object simultaneously. With the tight coupling of Lagrangian mechanics, the dynamic multivariate simplex splines representing the object can accurately simulate its physical behavior because it can unify the geometric and material properties in the simulation. The visualization can be directly computed from the object's geometric or physical representation based on the dynamic spherical multivariate simplex splines during simulation without interpolation or resampling. We have applied the framework for biomechanic simulation of brain deformations, such as brain shifting during the surgery and brain injury under blunt impact. We have compared our simulation results with the ground truth obtained through intra-operative magnetic resonance imaging and the real biomechanic experiments. The evaluations demonstrate the excellent performance of our new technique.

5.1 Introduction and Motivation

Modeling, simulation and assessment of digital representations of heterogeneous objects acquired from real-world are very challenging research tasks and have many potential applications. The fundamental objectives are to unambiguously model high-dimensional heterogeneous objects, accurately and effectively simulate their behaviors, and rigorously analyze their dynamic natures. Among many important aspects of physically based modeling and simulation, the accuracy is of utmost importance since only physically realistic simulation can be

used to represent the true reality and provide valuable information for the simulation-based assessment and analysis. In existing approaches, several different representations are typically required throughout the simulation of real-world models in computerized environments. That is to say, each stage within the entire physical simulation pipeline, including modeling (e.g., meshing, material modeling), simulation, analysis, visualization, typically takes as input a different representation of the modeled object, which requires costly and error-prone data conversions throughout the entire simulation process. It will certainly introduce error into the pipeline. For instance, in order to simulate the brain deformation, a linear solid mesh needs to be generated for finite element methods (FEMs) from the voxel-based representation of the brain representing the geometry of the brain (which has a highly convoluted cortical surface and many subtle sub-cortical structures). Then, manual material editing needs to be conducted to assign material properties to solid meshes. The FEM properties are linearly interpolated during simulation and resampled once again to voxels' intensities for visualization. Certainly, conversions among volumetric datasets, solid meshes, finite elements, and voxels based on linear interpolation or resampling will introduce error. In addition, more errors will be brought into the pipeline as the constructed linear solid mesh may not well represent both geometry and material distribution simultaneously. The geometric, physical, and mechanical properties are not tightly integrated into the simulation. As a result, the current practice impedes the accurate modeling and simulation of digital models of real-world objects. With ever-improving computing power comes the strong demand for more accurate, robust, and powerful solid modeling and simulation paradigms that are efficacious for the modeling, simulation, analysis, and visualization of digital models of real-world objects.

In order to bridge the gap and overcome the aforementioned deficiencies, we develop an integrated computational framework based on dynamic spherical volumetric simplex splines (DSVSS) that can greatly improve the accuracy and efficacy of modeling and simulation of heterogenous objects since the framework can not only reconstruct with high accuracy geo-

metric, material, and other quantities associated with heterogeneous real-world models, but also simulate the complicated dynamics precisely by tightly coupling these physical properties into simulation. The integration of geometric modeling, material modeling, and simulation is the key to the success of simulation of real-world objects. In contrast to existing techniques, our framework uses a single representation that requires no data conversion. The advantages of our framework result from many attractive properties of multivariate splines. In comparison with tensor-product NURBS, multivariate simplex splines are non-tensor-product in nature. They are essentially piecewise polynomials of the lowest possible degree and the highest possible continuity everywhere across their entire tetrahedral domain. For example, given an object of simplex splines with degree n , it can achieve C^{n-1} continuity. Furthermore, C^0 , other varying continuities, and even discontinuity can be accommodated through different knot and control point placements and/or different arrangements of domain tetrahedra in 3D. Furthermore, simplex splines are ideal to represent heterogeneous material distributions through the tight coupling of control points and their attributes. From dynamic simulation's point of view, they are finite elements which can be directly brought into finite element formulations and physics-based analysis without losing any information. Finite elements can be derived directly from the simplex spline representation, which can also be visualized via volumetric ray-casting without discretization [25]. Trivariate simplex splines are obtained through the projection of n -dimensional simplices onto 3D. Projecting them one step further onto 2D for visualization results in bivariate simplex splines of one degree higher than the original solid model, therefore, simplex splines facilitate the visualization task with an analytical, closed-form formulation. It is not necessary to perform any resampling and/or interpolation operations. Local adaptivity and local/global subdivision via knot insertion can be readily achieved.

On the application front, in recent years, tremendous efforts from biomedical research communities have been devoted into the brain simulation since accurate simulation of brain deformations can have many potential applications, e.g., computer-aided surgical planning/surgery,

computer-assisted disease/injury positioning, accurate radiation therapy, and many other medical benefits [39]. Various methods are emerging for simulation of the brains in different physical environments. However, most brain volume simulation techniques still depend on linear geometric representation and FEMs as we have already described above. No advanced computational models are available for better simulation. As we all know, the brain is a highly convoluted organ rich of geometric, anatomical, and material variations. In order to obtain realistic deformation simulation of the brain, it is very important to construct a digital model which can simultaneously represent its geometry, imaging intensities, and material properties, and then integrate the properties into the biomechanic simulation. Consider that the human brain is topologically equivalent to a solid sphere, our proposed dynamic spherical volumetric simplex splines are perfect for modeling, simulation, and analysis of such an object. The spherical volumetric simplex splines are defined over a solid spherical tetrahedralization. In this chapter, we apply and evaluate our simulation framework on various human brain deformations.

As depicted in *Figure 5.1*, the developed framework is fully automated without human intervention. The spherical domain is constructed from the subdivision of an icosahedron and harmonic volumetric mapping. With spherical domain and harmonic volume parameterization, the continuous volumetric representation of the modeled object is obtained through fitting spherical volumetric simplex splines to the real-world volume data. Physical properties can then be integrated into the system to unify the geometric representation as well as the physical representation. With Lagrangian dynamics essentials integrated into the pipeline, the powerful framework yields the dynamic representation of the digital model. The dynamic representation of the digital model can facilitate multiple tasks such as model assessment, biomechanic simulation, and visualization.

Our contributions in this chapter can be summarized as follows:

- We develop a physical simulation framework which seamlessly integrates geometric

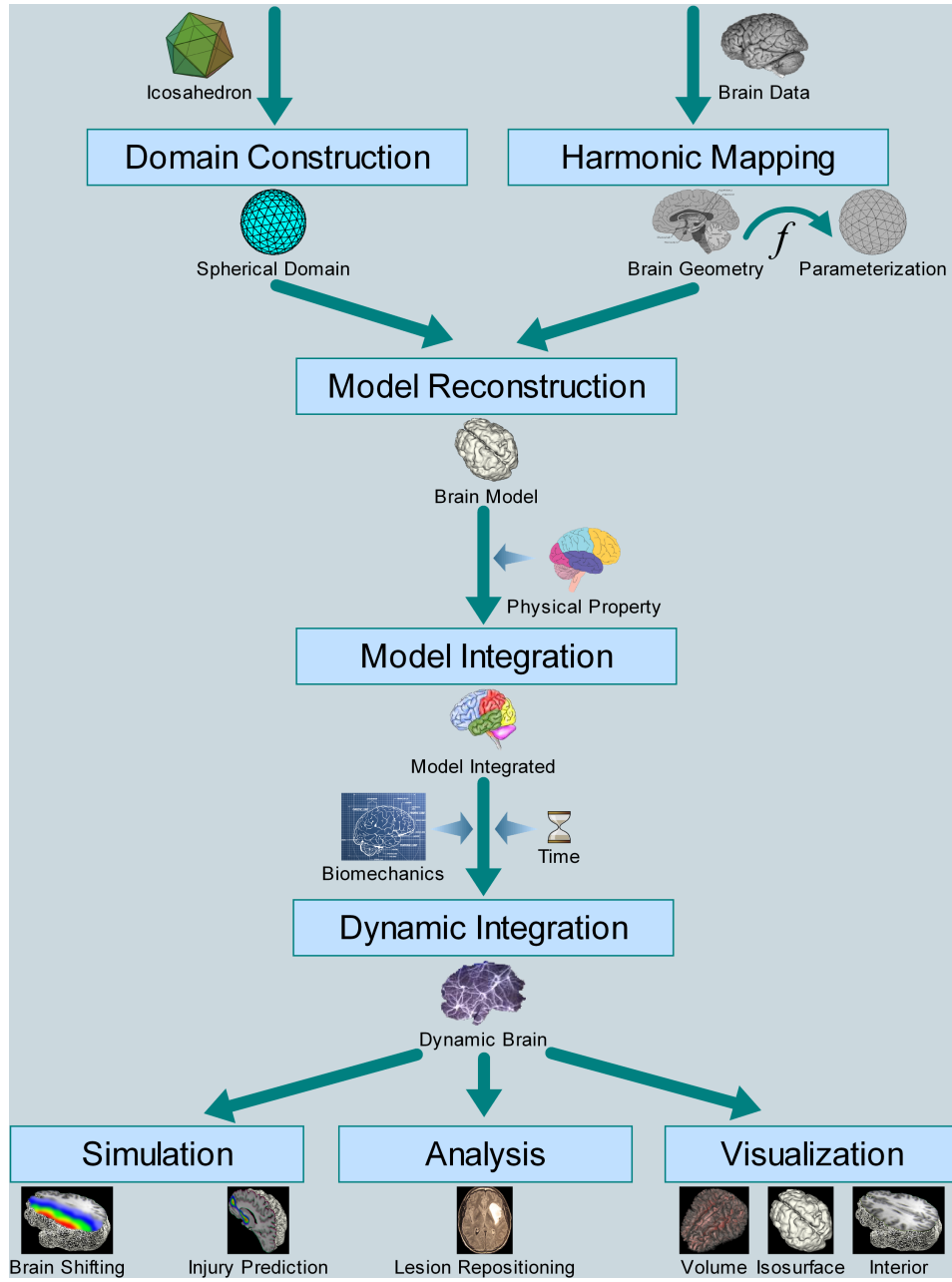


Figure 5.1: Illustration of the pipeline of our DSVSS framework. The rectangles inside the pipeline indicate tasks, and the icons with text under them denote the inputs and outputs of tasks.

properties, physical properties, and dynamic behaviors together. The consistent, uniform representation throughout each stage of modeling and simulation is a single degree n spherical volumetric simplex spline. It is ideal for simulating complex, heterogeneous

real-world objects.

- The heterogeneous model reconstructed from the digitalization of a real-world object is faithful and of high-fidelity in terms of its geometry and material distribution. The model reconstruction procedure is automatic, and the maximal fitting error to the original data can be controlled by user's specification interactively.
- During the simulation, the geometry and physical properties of the volumetric model can be computed using the analytic representation without any need for numerical approximations such as cubic interpolation or quadratic resampling. Hence, physical simulation, including all downstream processes, such as analysis and evaluation, can be achieved more accurately and robustly.
- We apply the dynamic spherical simplex splines scheme in the simulation and analysis of brain models. The unified scheme can achieve very accurate simulation compared with the ground-truth results because it can tightly integrate the geometric and material properties in the simulation. Our framework has great potential to provide simulation-based assessment for innovative computer-aided diagnosis of brain injury cases.

5.1.1 Previous Work

This section reviews the previous work related to the theory and application of multivariate simplex splines and physically based modeling and simulation. In particular, we provide the brief background regarding the brain simulation and its potential applications.

Multivariate Simplex Splines

From projection's point of view, univariate B-splines can be intuitively formulated as volumetric shadows of higher dimensional simplices, i.e., we can obtain B-splines of arbitrary degree n by taking a simplex in the $(n + 1)$ -dimensional space and volumetrically projecting it onto R^1 . Motivated by this idea of Curry and Schoenberg, C. de Boor [14] presented a brief description of multivariate simplex splines. In essence, multivariate simplex splines are the

volumetric projection of higher dimensional simplices onto a lower dimensional space R^m . Simplex splines have many attractive properties such as piecewise polynomials over general tetrahedral domains, local support, higher-order smoothness, and positivity, making them potentially ideal in engineering design applications [21]. From the point of view of blossoming, Dahmen *et al.* [13] proposed triangular B-splines. Later, Greiner and Seidel [21] demonstrated their practical feasibility in graphics and shape design.

In contrast to theoretical advances, the application of simplex splines has been rather under-explored. Pfeifle and Seidel developed a faster evaluation technique for quadratic bivariate DMS-spline surfaces [59] and applied it to the scattered data fitting of triangular B-spline [61]. Recently, Rössl *et al.* [56] presented a novel approach to reconstruct volume from structure-gridded samples using trivariate quadric super splines defined on a uniform tetrahedral partition. They used Bernstein-Bézier techniques to compute and evaluate the trivariate spline and its gradient. Hua and Qin presented a volumetric sculpting framework that employs trivariate scalar nonuniform B-splines as underlying representation [27, 29]. More recently, they applied trivariate simplex splines to the representation of solid geometry, the modeling of heterogeneous material attributes, and the reconstruction of continuous volumetric splines from discretized volumetric inputs via data fitting [26]. Tan *et al.* applied the hierarchical simplex splines to volume reconstruction from planar images [87].

Physically Based Modeling and Biomechanic Simulation

Free-form deformable models were first introduced to the modeling community by Terzopoulos *et al.* [91], and they have been improved by a number of researchers over the past 20 years. Celniker and Gossard developed an interesting prototype system [4] for interactive free-form design based on the finite-element optimization of energy functionals proposed in [91]. Bloor and Wilson developed related models using similar energies and numerical optimization [2]. Welch and Witkin extended the approach to trimmed hierarchical B-splines for interactive modeling of free-form surfaces with constrained variational optimization [104]. Terzopoulos

and Qin [93, 65] devised dynamic physically based generalization of NURBS (D-NURBS). Later, they further developed dynamic triangular B-splines [64] paradigm for high topology surface modeling. The new paradigm on simplex spline finite elements is substantially more sophisticated and is expected to produce even more true-to-life simulation results.

As for simulation of digital models of real-world objects, researchers have focused on FEM meshing, which can represent the shape of the objects, and physical laws and properties, which govern the model's behavior. Zhang *et al.* presented a method for 3D mesh generation from imaging data [108]. They further designed an algorithm for automatic 3D mesh generation for a domain with multiple materials. In general, the main objective of FEM meshing is to construct a nicely-shaped elements which can represent both geometry and material of the real-world models for accurate and robust simulation. However, due to its linear representations in general, it cannot accurately represent the geometric and physical properties of real-world objects. For simulation-based assessment of real-world objects, e.g., the brain, these FEM representations are not able to obtain an accurate and objective analysis result [107].

Biomechanic simulation of brain behaviors such as brain shifting and brain injury gains ever-increasing importance in recent years while these behaviors remain an unclear problem for public health professionals. Although impeded by that fact that brain material properties can not be retrieved directly from the human brain in vivo, there is a certain number of research which have been done either using animal brains or modifying brain biomechanic parameters to approach the real situation. Margulies *et al.* studied the relationship between non-preconditioned and preconditioned biomechanic response of brain tissue from porcine [18]. Later they further investigated the homogeneity of gray matter by measuring stiffness of cerebral cortex and comparing it to the thalamus of porcine brain [10]. Many investigations have been conducted using mathematical finite element modeling [75, 31, 107]. In general, the cerebral tissues in their models were represented by homogeneous materials. Recent studies started to make distinctions between gray and while matters. In terms of applications, brain

deformation simulation facilitates researchers and clinicians new prospects in clinical practice [39].

5.2 Spherical Multivariate Simplex Spline Volume

Generally, volumetric simplex spline can take as input any domain with arbitrary geometry and topology due to its non-tensor-product nature. Spherical simplex spline volume is defined by volumetric simplex splines over a spherical volumetric domain. Here, we choose the sphere domain since mapping most organic objects in the biomedical research field to a sphere results in less distortion and more uniform distribution of sampling points, which reduces the difficulty in the fitting procedure. Note that, our volumetric simplex spline volumes represent not only boundary geometry, but also interior geometry. They can represent physical or material attributes over the entire solid as well.

Generally, volumetric simplex spline can take as input any domain with arbitrary geometry and topology due to its non-tensor-product nature. Spherical simplex spline volume is defined by volumetric simplex splines over a spherical volumetric domain. Here, we choose the sphere domain since mapping most organic objects in the biomedical research field to a sphere results in less distortion and more uniform distribution of sampling points, which reduces the difficulty in the fitting procedure. Note that, our volumetric simplex spline volumes represent not only boundary geometry, but also interior geometry. They can represent physical or material attributes over the entire solid as well.

5.2.1 Spherical Volumetric Simplex Splines

Now let $\mathbb{S}^3 = \{\mathbf{x} \in \mathbb{R}^3, \|\mathbf{x}\| \leq c\}$ denote a solid sphere in \mathbb{R}^3 . Without loss of generality, let \mathbb{S}^3 be a unit solid sphere, i.e., $c = 1$. Let \mathbf{T} be an arbitrary “proper” tetrahedralization of \mathbb{S}^3 . Here, “proper” means that every pair of domain tetrahedra are disjoint, or share exactly one vertex, one edge, or one face. To each vertex \mathbf{t} of the tetrahedralization \mathbf{T} , we assign a knot cloud, which is a sequence of points $[\mathbf{t}_0, \mathbf{t}_1, \dots, \mathbf{t}_n]$, where $\mathbf{t}_0 \equiv \mathbf{t}$. We call \mathbf{t} primary-knot and $[\mathbf{t}_1, \dots, \mathbf{t}_n]$ sub-knots. *Figure 3.1-(a)* shows 4 vertices with cubic knot clouds associated,

which are labeled as $\mathbf{p}, \mathbf{q}, \mathbf{r}$, or \mathbf{s} group, respectively. The primary-knots are rendered with yellow dots and sub-knots with blue dots. We will use these two colors to differentiate the primary-knots and sub-knots in the rest illustrations.

For every tetrahedron $I = (\mathbf{p}, \mathbf{q}, \mathbf{r}, \mathbf{s}) \in \mathbf{T}$, in addition to the requirements specified in Chapter 3.3.2, we particular require

- if I is a boundary tetrahedron, the sub-knots assigned to the boundary vertices must lie outside of \mathbb{S}^3 , i.e, all the sub-knots should be distributed outside of the unit solid sphere.

Figure 5.2-(a) illustrates a spherical volumetric simplex spline and its domain with its cubic knot clouds associated. As observed in the figure, the sub-knots assigned to the boundary vertices of the sphere domain are positioned outside of the sphere. Figure 5.2-(b) shows the control space and the evaluated spherical volumetric simplex volume.

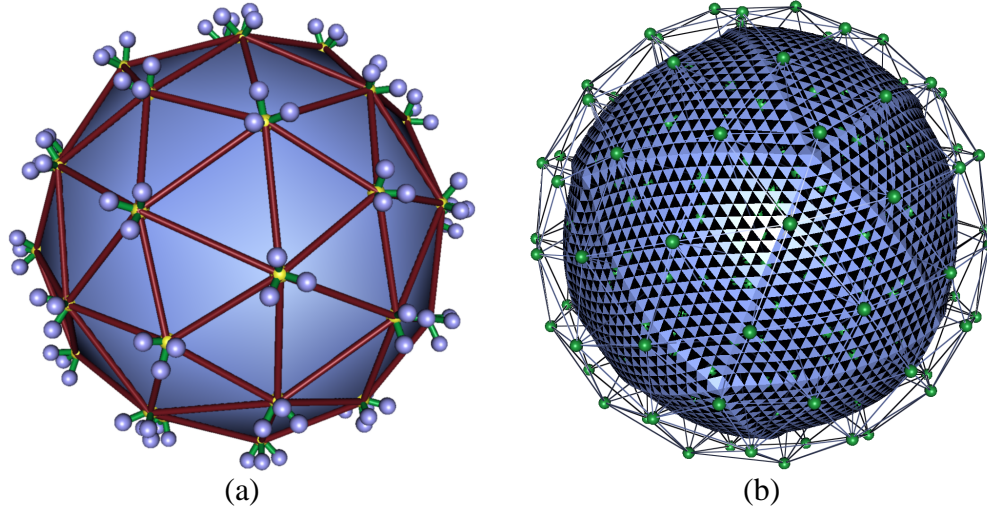


Figure 5.2: (a) The spherical domain with assigned knot clouds for defining spherical volumetric simplex splines. The yellow and blue dots denote primary-knots and sub-knots, respectively; (b) The spherical simplex spline volume defined upon the domain in (a). The green dots denote the control points. The evaluated spherical volume simplex volume is scaled to show its nonempty interior property.

5.2.2 Initial Construction of Spherical Volumetric Domain

Theoretically, domain tetrahedralization, \mathbf{T} , can be an arbitrary tetrahedralization of a unit solid sphere, \mathbb{S}^3 , as aforementioned in *Chapter 5.2.1*. However, in practice, two important aspects of the domain tetrahedralization should be carefully considered:

- \mathbf{T} should be as uniform as possible, i.e., minimize $\frac{\max(\text{Vol}_{I \in \mathbf{T}})}{\min(\text{Vol}_{I' \in \mathbf{T}})}$. Uniform tetrahedralization at the same hierarchical level will decrease the recursion time while hierarchical structure is needed.
- \mathbf{T} should avoid bad-shaped tetrahedra in Delaunay tetrahedralization. Bad-shaped tetrahedra, for instance, slivers, will increase numerical error during the evaluation.

Constrained Delaunay tetrahedralization [15] can observe the second requirement, but it will introduce very large and very small tetrahedra thus can not comply with the first requirement. Instead, we tetrahedralize a regular icosahedron and then make use of harmonic volumetric mapping to map the tetrahedralization to a solid sphere. As a result, the solid sphere tetrahedralization is uniform and its quality is better than what constrained Delaunay tetrahedralization can offer.

Figure 5.3 shows the flow of domain establishment and the knots distribution. Note that, in *Figure 5.3-(d)*, the sub-knots associated with boundary vertices are placed outside of the sphere. The uniform tetrahedralization may be subdivided and refined when necessary, e.g., modeling discontinuity as described later.

5.2.3 Volumetric Parameterization

To find a volumetric parameterization of a genus-zero solid, harmonic volumetric mapping facilitates a viable solution. Harmonic volumetric mapping was first implemented for applications by Wang *et al.* [102, 103]. They successfully exposed its merits by applying the approach to brain mapping which can be considered as a genus-zero volume. Recently Li *et al.* [36] further extended the scheme to high-genus harmonic volumetric mapping and employed it in solid

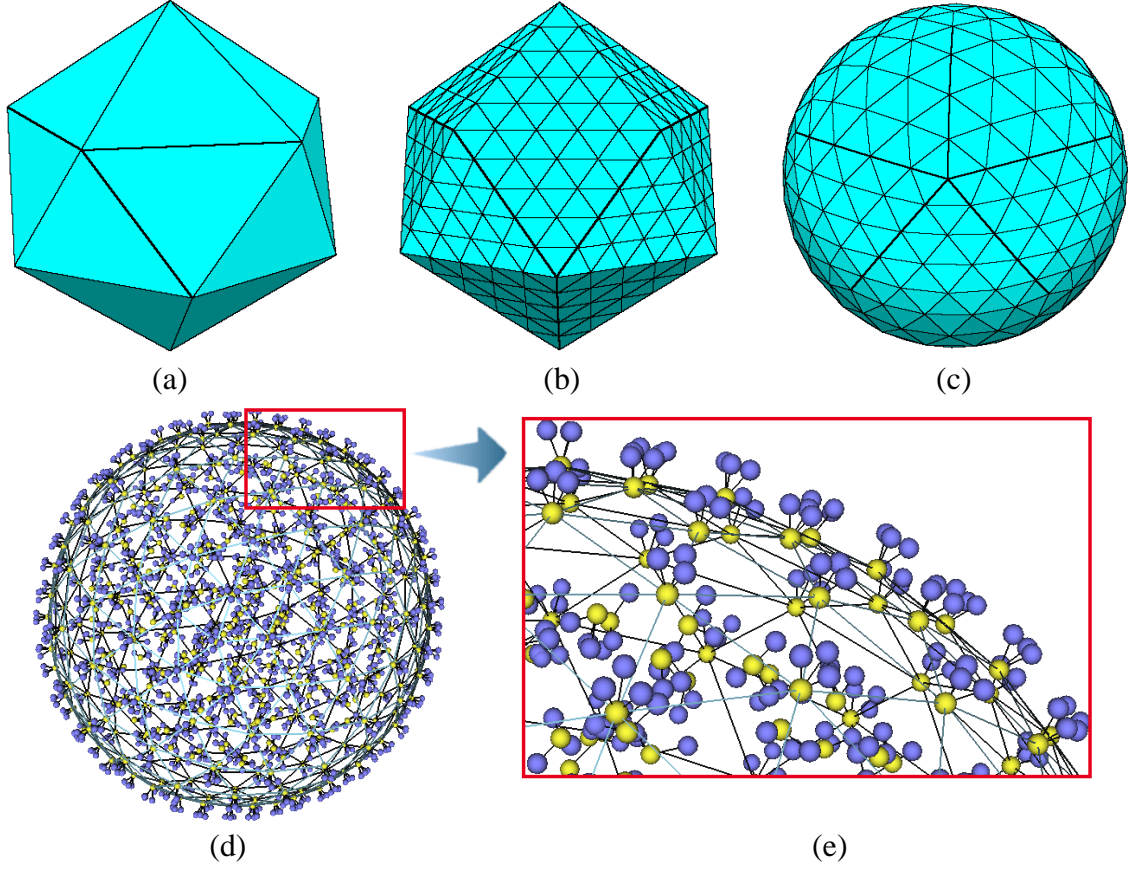


Figure 5.3: (a) A regular icosahedron, which is the best approximation of a solid sphere among all regular polyhedra; (b) Tetrahedralization of (a) is uniform and it is easy to implement; (c) Harmonic mapping from (b) to a unit solid sphere yields the domain tetrahedralization, consisting of uniform and well-shaped tetrahedra; (d) A domain with cubic knot clouds assigned to (c); (e) A close view of the domain picked from (d).

modeling applications. Harmonic volumetric mapping can be formulated as follows:

Given two solid objects M_1 and M_2 , and their boundary surfaces ∂M_1 and ∂M_2 . Suppose that \vec{f}' is the conformal mapping [22, 101] between ∂M_1 and ∂M_2 , which is pre-computed. The harmonic volumetric mapping $\vec{f}: M_1 \mapsto M_2$ satisfies:

$$\begin{cases} \nabla^2 \vec{f}(v) = 0, & v \in M_1 \setminus \partial M_1, \\ \vec{f}(v) = \vec{f}'(v), & v \in \partial M_1, \end{cases}$$

where the ∇^2 is the Laplacian operator defined continuously in 3D as

$$\frac{\partial^2}{\partial x^2} + \frac{\partial^2}{\partial y^2} + \frac{\partial^2}{\partial z^2},$$

and $\nabla^2 \vec{f} = 0$ for $\vec{f} = (f_0, f_1, f_2)$ is equivalent to $\nabla^2 f_i = 0$ for all $i = 0, 1, 2$.

The harmonic volumetric mapping f here minimizes a harmonic energy $E(f)$ [103], which is defined as

$$E(f) = \sum_{(u,v)} k(u,v)(f(u) - f(v))^2, \quad (5.1)$$

where $k(u,v)$ is the string constant defined in edge between u and v . Here, f can be solved using steepest descent algorithm.

The algorithmic procedure of harmonic volumetric mapping is concisely summarized as follows:

1. For each boundary vertex, v , $v \in \partial M_1$, let $\vec{f}(v) = \vec{f}'(v)$; for each interior vertex, v , $v \in M_1 \setminus \partial M_1$, let $\vec{f}(v) = \vec{0}$, compute the harmonic energy E_0 using *Equation 5.1*.
2. For each interior vertex, v , $v \in M_1 \setminus \partial M_1$, compute its derivative $D\vec{f}$ using steepest descent algorithm, then update $\vec{f}(v)$ by $\delta \vec{f}(v) = -D\vec{f}(t)\delta t$, δt is the step length.
3. Compute the harmonic energy E ; if $E - E_0$ is less than user specified threshold δE , the algorithm stops; Otherwise assign E to E_0 and repeat step (2) through step (3).

Figure 5.4 shows the harmonic volumetric mapping from one brain to a solid unit sphere. After the mapping has been established, the point parameterization and correspondence between the domain and the object can now be stored as the input of our spherical simplex spline model reconstruction algorithm.

5.2.4 Fitting with Spherical Volumetric Simplex Splines

After harmonic volumetric mapping, a finite number of discretized sampling points of the physical object, $(x_i, y_i, z_i, \rho_i)_{i=1}^m$, and their parametric coordinates in the domain, $(u_i, v_i, w_i)_{i=1}^m$,

can be retrieved. ρ_i denote a physical attribute. Note that, there could be multimodality physical attributes with more dimensions. In this case, all we need to do is to increase the dimensions and add the additional variables into the sampling. All the computation remains the same. Without loss of generality, we only consider one type of attribute here in order to simplify the mathematical notation. The sampling point pairs indicates the parameterization from the solid sphere domain to the to-be-modeled object. Volumetric simplex spline is an ideal tool for fitting the geometry as well as the physical properties of the volumetric object. In this section, we will describe how to fit spherical volumetric simplex splines to the real-world model.

The problem of model reconstruction in our system can be stated as follows: given a set $P = \{\mathbf{p}_i\}_{i=1}^m$ of points, $\mathbf{p}_i = (x_i, y_i, z_i, \rho_i) \in \mathbb{R}^4$, and $G = \{\mathbf{g}_i\}_{i=1}^m$, $\mathbf{g}_i = (x_i, y_i, z_i) \in \mathbb{R}^3$ denoting the pure geometry extracted from the sampling points, find a volumetric simplex splines volume $\mathbf{s} : \mathbb{R}^3 \rightarrow \mathbb{R}^3$ that approximates G .

Since we are interested in reconstructing the model with respect to its solid geometry, our spherical simplex spline volumes are vector functions, i.e., the control points $\mathbf{c}_\beta^I \in \mathbb{R}^3$ are vectors. Unlike the existing fitting algorithms with simplex splines which usually find the parametric domain which is close to the original geometry of the to-be-fitted dataset [25, 26], we use the position (u_i, v_i, w_i) within the solid sphere as the data point \mathbf{g}_i 's parametric value. Therefore, we need to minimize the following objective function:

$$\min E_{dist}(\mathbf{s}) = \sum_{i=1}^m (\mathbf{g}_i - \mathbf{s}(u_i, v_i, w_i))^2. \quad (5.2)$$

Equation 5.2 is a typical least squares problem. If the control points are treated as free variables, it falls into a very special category of nonlinear programming, i.e., unconstrained convex quadratic programming, which has the following form:

$$E_{dist} = \frac{1}{2} \mathbf{x}^T Q \mathbf{x} + \mathbf{c}^T \mathbf{x} + f,$$

where $\mathbf{x} = (\dots, \mathbf{c}_\beta^I, \dots)^T$,

$$Q = \begin{pmatrix} & & \vdots & & \\ & \dots & 2 \sum_{i=1}^m N_\beta^I(u_i, v_i, w_i) N_{\beta'}^{I'}(u_i, v_i, w_i) & \dots & \\ & & \vdots & & \end{pmatrix},$$

$$\mathbf{c} = (\dots, -2 \sum_{i=1}^m \mathbf{g}_i N_\beta^I(u_i, v_i, w_i), \dots)^T,$$

and $f = \sum_{i=1}^m \mathbf{g}_i^2$. Note that, Q is a positive definite, symmetric and sparse matrix. Interior-point method can solve this problem very efficiently.

After reconstruction procedure, we can achieve an integrated representation incorporating the object's solid geometry, \mathbf{s} , and its material attribute, \mathbf{d} , at the same time. The scheme can be expressed as

$$\begin{bmatrix} \mathbf{s} \\ \mathbf{d} \end{bmatrix}(\mathbf{u}) = \sum_{I \in \mathbf{T}} \sum_{|\beta|=n} \begin{bmatrix} \mathbf{c} \\ d_c \end{bmatrix} N(\mathbf{u}|V_\beta^I), \quad (5.3)$$

where \mathbf{c} and d_c are the control points and control coefficients for solid geometry and material attributes, respectively.

To model discontinuity in attribute field, we first detect where the discontinuity occurs, then decompose the original domain into two separated new domains with shared vertices and edges as the 2D illustration in *Figure 5.5*. This simple mechanism maintains the consistent structure of the domains. The evaluation, hierarchy structure, and data structure all remain the same. Therefore, we can perform the same evaluation on these two domains simultaneously as if the evaluation is performed on a single domain. With the association of different control coefficients, the functional evaluation can output a discontinuity in material field corresponding to the shared edges. This change will not affect the geometry of the DSVSS volume as long as the associated control points remain the same.

5.3 Dynamic Spherical Multivariate Simplex Splines

In this section, we formulate our dynamic spherical volumetric simplex splines. We integrate mass, dissipation, and deformation energy into static simplex spline models, and employ Lagrangian dynamics to derive their equations of motion. Consequently, the static control points of the geometric model become generalized time-varying physical coordinates in the dynamic model.

5.3.1 Geometry and Kinematics of Simplex Spline Volumes

The dynamic simplex splines further extend the geometric simplex splines by incorporating time into the volume representation. Now the function of representation bears both parametric variable \mathbf{u} and time t as follows:

$$\mathbf{s}(\mathbf{u}, t) = \sum_{I \in \mathbf{T}} \sum_{|\beta|=n} \mathbf{c}_\beta^I(t) N_\beta^I(\mathbf{u}). \quad (5.4)$$

For simplicity of formulation expression, we define the vector of generalized coordinates of control points \mathbf{c}_β^I as:

$$\mathbf{c} = [\cdots, \mathbf{c}_\beta^{I^\top}, \cdots]^\top, \quad (5.5)$$

where \top denotes transposition. We then express *Equation 5.4* as $\mathbf{s}(\mathbf{u}, \mathbf{c})$ in order to emphasize its dependence on \mathbf{c} whose components are functions of time. Hence, the velocity of the dynamic simplex splines is:

$$\dot{\mathbf{s}}(\mathbf{u}, t) = \mathbf{J} \dot{\mathbf{c}}, \quad (5.6)$$

where the overstruck dot denotes a time derivative and Jacobian matrix $\mathbf{J}(\mathbf{u})$ is the concatenation of the vectors $\partial \mathbf{s} / \partial \mathbf{c}_\beta^I$. Assuming m tetrahedral in the parametric domain, β traverses $k = (n+1)(n+2)(n+3)/6$ possible tetrads whose components sum to n . Because \mathbf{s} is a 4-vector and \mathbf{c} is an $M = 4mk$ dimensional vector, \mathbf{J} is a $4 \times M$ matrix, which is expressed as

$$\mathbf{J} = \left[\cdots, \begin{bmatrix} N_{\beta}^I & 0 & 0 & 0 \\ 0 & N_{\beta}^I & 0 & 0 \\ 0 & 0 & N_{\beta}^I & 0 \\ 0 & 0 & 0 & N_{\beta}^I \end{bmatrix}, \cdots \right], \quad (5.7)$$

where $N_{\beta}^I(\mathbf{u}) = \frac{\partial \mathbf{s}_x}{\partial \mathbf{c}_{\beta_x}^I} = \frac{\partial \mathbf{s}_y}{\partial \mathbf{c}_{\beta_y}^I} = \frac{\partial \mathbf{s}_z}{\partial \mathbf{c}_{\beta_z}^I} = \frac{\partial \mathbf{s}_d}{\partial \mathbf{c}_{\beta_d}^I}$.

The subscripts x, y, z and d denote derivatives of the components of the 4-vector: Cartesian coordinates and physical property, respectively. Apparently, the solid volume can be presented as the production of the product of the Jacobian matrix and the generalized coordinate vector,

$$\mathbf{s}(\mathbf{u}, \mathbf{c}) = \mathbf{J}\mathbf{c}. \quad (5.8)$$

5.3.2 Lagrange Equations of Motion

Lagrange dynamics are widely used in physics-based shape design. In this section, we derive the equations of motion of dynamic simplex splines by applying Lagrangian dynamics [20]. We express the kinetic energy due to the prescribed mass distribution function $\mu(u, v, w)$, and a Raleigh dissipation energy due to a damping density function $\gamma(u, v, w)$. Both energy functions are defined over the parametric domain of the volume. The mass distribution function and damping density function are reconstructed with spherical volumetric simplex splines as well, as described in *Chapter 5.2.4*. 3D thin-plate-like energy under tension energy model [4, 24, 104, 90] is employed here in order to define an elastic potential energy,

$$\begin{aligned} U = \frac{1}{2} \iiint (\alpha_{1,1} \mathbf{s}_u^2 + \alpha_{2,2} \mathbf{s}_v^2 + \alpha_{3,3} \mathbf{s}_w^2 + \\ \beta_{1,1} \mathbf{s}_{uu}^2 + \beta_{1,2} \mathbf{s}_{uv}^2 + \beta_{1,3} \mathbf{s}_{uw}^2 + \beta_{2,2} \mathbf{s}_{vv}^2 + \\ \beta_{2,3} \mathbf{s}_{vw}^2 + \beta_{3,3} \mathbf{s}_{ww}^2) du dv dw. \end{aligned} \quad (5.9)$$

The subscripts on \mathbf{s} denote the parametric partial derivatives. The $\alpha_{i,j}(u, v, w)$ and $\beta_{i,j}(u, v, w)$ are elasticity functions which control tension and rigidity, respectively. Other energies, requiring greater computational cost, are also applicable, for instance, the non-quadratic, curvature-based energies in [92, 48]. Applying the Lagrangian formulation, we obtain the second-order equations of motion

$$\mathbf{M}\ddot{\mathbf{c}} + \mathbf{D}\dot{\mathbf{c}} + \mathbf{K}\mathbf{c} = \mathbf{f}_c, \quad (5.10)$$

where the mass matrix is

$$\mathbf{M} = \iiint \mu \mathbf{J}^\top \mathbf{J} du dv dw, \quad (5.11)$$

the damping matrix is

$$\mathbf{D} = \iiint \gamma \mathbf{J}^\top \mathbf{J} du dv dw, \quad (5.12)$$

and the stiffness matrix is

$$\begin{aligned} \mathbf{K} = \iiint & (\alpha_{1,1} \mathbf{J}_u^\top \mathbf{J}_u + \alpha_{2,2} \mathbf{J}_v^\top \mathbf{J}_v + \alpha_{3,3} \mathbf{J}_w^\top \mathbf{J}_w + \\ & \beta_{1,1} \mathbf{J}_{uu}^\top \mathbf{J}_{uu} + \beta_{1,2} \mathbf{J}_{uv}^\top \mathbf{J}_{uv} + \beta_{1,3} \mathbf{J}_{uw}^\top \mathbf{J}_{uw} + \\ & \beta_{2,2} \mathbf{J}_{vv}^\top \mathbf{J}_{vv} + \beta_{2,3} \mathbf{J}_{vw}^\top \mathbf{J}_{vw} + \beta_{3,3} \mathbf{J}_{ww}^\top \mathbf{J}_{ww}) du dv dw. \end{aligned} \quad (5.13)$$

\mathbf{M} , \mathbf{D} and \mathbf{K} are all $M \times M$ matrices. \mathbf{f}_c is the generalized force, which is obtained through the principle of virtual work [20] done by the applied force distribution $\mathbf{f}(u, v, w, t)$. \mathbf{f}_c can be computed as follows:

$$\mathbf{f}_c = \iiint \mathbf{J}^\top \mathbf{f}(u, v, w, t) du dv dw. \quad (5.14)$$

5.4 Finite Element Framework

The evolution of the vector of generalized coordinates, $\mathbf{c}(t)$, is determined by the second-order nonlinear differential equation. *Equation 5.10* with physical parameter dependent matri-

ces, does not have an analytical solution. Instead, we obtain an efficient numerical implementation using finite-element techniques.

Standard finite element methods explicitly integrate the individual element matrices into the global matrices that appear in the discrete equations of motion [32]. Although applicable in some environments, it is infeasible in our infrastructure because of its unacceptably high computational cost. Instead, we pursue an iterative matrix solver to avoid the cost of assembling the global matrices \mathbf{M} , \mathbf{D} , and \mathbf{K} , working instead with the individual dynamic simplex spline element matrices. We construct finite element data structures, similar to [64], which facilitates the parallel computation of element matrices.

5.4.1 Data Structures for Dynamic Simplex Spline Finite Elements

We define an element data structure which contains the geometric specification of the tetrahedron patch element along with its physical properties. In each element, we allocate an elemental mass, damping, and stiffness matrix, and include the quantities such as the mass $\mu(u, v, w)$, damping $\gamma(u, v, w)$, and elasticity $\alpha_{i,j}(u, v, w)$ and $\beta_{i,j}(u, v, w)$ functions. A complete dynamic simplex spline consists of an ordered array of elements with additional information. The element structure includes pointers to appropriate components of the global vector \mathbf{c} . Neighboring tetrahedra will share some generalized coordinates.

The physical parameters, such as mass $\mu(u, v, w)$, damping $\gamma(u, v, w)$, and elasticity, $\alpha_{i,j}(u, v, w)$ and $\beta_{i,j}(u, v, w)$, need to be measured and computed before the calculation of element matrices. In this section, as the goal of the applications is to simulate the biomechanical behavior of the brain, we directly adopt μ and γ from the brain study conducted by Zhang *et al.* [106]. According to the relationship of elastic moduli of elastic isotropic materials [95], α and β can be computed from Bulk modulus and Poisson's ratio as follows:

$$\alpha = 3B(1 - 2\nu), \quad (5.15)$$

$$\beta = \frac{3B(1-2\nu)}{(2+2\nu)}, \quad (5.16)$$

where B is the Bulk modulus and ν is the Poisson's ratio of brain tissues. After we get the physical parameters for different types of brain tissues, we then take these coefficients into the fitting procedure to integrate them into our DSVSS framework. Now the volume representation can be described as follows:

$$\begin{bmatrix} \mathbf{s} \\ \mu \\ \gamma \\ \alpha \\ \beta \end{bmatrix}(\mathbf{u}) = \sum_{I \in \mathbf{T}} \sum_{|\beta|=n} \begin{bmatrix} \mathbf{c} \\ \mu_c \\ \gamma_c \\ \alpha_c \\ \beta_c \end{bmatrix} N(\mathbf{u}|V_\beta^I), \quad (5.17)$$

where \mathbf{c} and $\mu_c, \gamma_c, \alpha_c, \beta_c$ are the control points and control coefficients for solid geometry and material physical attributes, respectively. Homogeneously taking the parameters into the element without fitting may sound feasible. However, it is the fitting procedure that takes attribute field discontinuity into account to achieve a model of high fidelity.

5.4.2 Calculation of Element Matrices

We employ Gaussian quadrature [62] to numerically evaluate the integral expressions for the mass, damping, and stiffness matrices associated with each element. In this section, we explain the expression of the element damping matrix in detail; the expressions of mass and stiffness matrix will follow suit. Assuming the parametric domain of the element is $I(v_0, v_1, v_2, v_3)$ where v_i denotes the vertex, the expression for entry d_{ij} of the damping matrix takes the integral form

$$d_{ij} = \int_{I \in T} \int_{I(v_0, v_1, v_2, v_3)} \gamma(u, v, w) f_{ij}(u, v, w) du dv dw, \quad (5.18)$$

where f_{ij} is evaluated using the recursive expression in *Equation 4.1*. Given integers N_g , we can find the corresponding Gauss weights a_g , and parametric abscissas u_g, v_g , and w_g such that d_{ij} can be approximated by

$$d_{ij} \approx \sum_{g=1}^{N_g} a_g \gamma(u_g, v_g, w_g) f_{ij}(u_g, v_g, w_g). \quad (5.19)$$

In our system, we choose N_g to be 10 for cubic dynamic simplex splines. Because of the irregularity of the knot distribution, many of the f_{ij} vanish over the sub-space of $I(v_0, v_1, v_2, v_3)$. We can further subdivide the $I(v_0, v_1, v_2, v_3)$ to minimize the numerical error.

5.4.3 Discrete Dynamics Equations

In this section, we will derive the discrete dynamics equations based on *Equation 5.10*. In order to integrate it in a simulation system, e.g., tissue simulation during surgery, it is important to provide users with visual feedback about the evolution state of the DSVSS model. Rather than using computation-intensive time integration methods which may traverse the largest possible time steps, it is more crucial to provide a smoothly simulated display by maintaining the continuity of the dynamics from one step to the next. Therefore, it is much desirable to employ less costly yet stable time integration methods that take reasonable time steps.

The state of the dynamic simplex splines at time $t + \Delta t$ is integrated using prior states at t and $t - \Delta t$. To maintain the stability of the integration scheme, especially for high stiffness configurations with large elasticity functions, we use an implicit time integration method, which employs discrete derivatives of \mathbf{c} using backward differences. The velocity expression is

$$\dot{\mathbf{c}}^{t+\Delta t} \approx (\mathbf{c}^{(t+\Delta t)} - \mathbf{c}^{(t-\Delta t)})/2\Delta t, \quad (5.20)$$

and the acceleration expression is

$$\ddot{\mathbf{c}}^{t+\Delta t} \approx (\mathbf{c}^{(t+\Delta t)} - 2\mathbf{c}^{(t)} + \mathbf{c}^{(t-\Delta t)})/\Delta t^2. \quad (5.21)$$

Then the time integration formula can be expressed as

$$\begin{aligned} (2\mathbf{M} + \Delta t\mathbf{D} + 2\Delta t^2\mathbf{K})\mathbf{c}^{(t+\Delta t)} = \\ 2\Delta t^2\mathbf{f}_c + 4\mathbf{M}\mathbf{c}^{(t)} - (2\mathbf{M} - \Delta t\mathbf{D})\mathbf{c}^{(t-\Delta t)}, \end{aligned} \quad (5.22)$$

where the superscripts denote evaluation of the quantities at the indicated times. The matrices and forces are evaluated at time t . Our extensive experiments have shown that this discretization scheme produces satisfactory results. Instability due to large transient applied forces can be reduced by shortening the time integration step adaptively.

The equations of motion allow physically realistic simulation of real-world models with complex dynamics. However, it is possible to make simplifications to the equations of motion to further reduce the computational cost of solving *Equation 5.22* when we simulate some more complicated volumes which bears more tetrahedra in its domain. In certain solid modeling and simulation applications where the inertial terms are not taken into count, the *Equation 5.10* can be simplified by setting the mass density function to zero. Without computation of the acceleration terms or storage of mass matrices, the algorithm is more efficient. With zero mass density, *Equation 5.10* simplifies to

$$\mathbf{D}\dot{\mathbf{c}} + \mathbf{K}\mathbf{c} = \mathbf{f}_c. \quad (5.23)$$

Discretizing the corresponding derivatives of \mathbf{c} in *Equation 5.23* with backward differences, the integration formula becomes

$$(\mathbf{D} + \Delta t\mathbf{K})\mathbf{c}^{(t+\Delta t)} = \Delta t\mathbf{f}_c + \mathbf{D}\mathbf{c}^{(t)}. \quad (5.24)$$

5.5 Brain Simulation Using DSMSS Volume

With the reconstruction of brain model from both MRI data and material map using our spherical volumetric simplex splines, we can obtain an analytic representation simultaneously describing both geometric and physical properties of the brain. Thus, brain simulations, such as brain shifting, deformation, and brain injury predication, can be achieved via the simulation-based analysis. In this section, we present the accurate brain reconstruction and simulation using our unified scheme, DSVSS volume. The reconstruction process is fully automated, and for brain simulation, the user only needs to initialize a few environmental parameters, e.g., the gravity and the resected skull in brain shifting simulation.

5.5.1 Fitting Spherical Volumetric Simplex Splines to Brain Data

Taking a set of high-resolution brain SPGR MR scans, we first strip away the skull and only retain the brain volume as shown in *Figure 5.6-(a)*. With the initial tetrahedralization of the brain model and harmonic volumetric mapping, we can obtain the parameterization of the data points of the brain tetrahedralization as described in *Chapter 5.2.3*, i.e., the parameterization describes the correspondence between the brain data points and parametric coordinates in the sphere domain. Fitting spherical volumetric simplex splines to the geometric representation, we can reconstruct the geometry of the brain nicely as shown in *Figure 5.4*. To model the intensities (for visualization purpose) and material distribution (for simulation purpose), we can start with the same spherical tetrahedral domain, and then subdivide and refine the domain [87], when necessary, to model more sophisticated material variations or discontinuities as described in *Chapter 5.2.4*. Note that, the intensities and material of brain structures are related since the imaging procedure can be considered as a function mapping of the material maps to scanned images. So the required domain for intensities and material distributions are very similar. *Figure 5.6* shows the reconstruction result with different rendering techniques and

Equation 5.25 shows the reconstructed representation,

$$\begin{bmatrix} \mathbf{s} \\ \mathbf{d} \\ \mathbf{I} \end{bmatrix}(\mathbf{u}) = \sum_{I \in \mathbf{T}} \sum_{|\beta|=n} \begin{bmatrix} \mathbf{c} \\ d_c \\ I_c \end{bmatrix} N(\mathbf{u}|V_\beta^I), \quad (5.25)$$

where \mathbf{s} denotes the solid geometry of the brain, \mathbf{d} denotes the reconstructed physical attributes of the brain, and \mathbf{I} denotes the reconstructed image intensities from the high-resolution SPGR MRI sequence. \mathbf{c} , d_c and I_c are the control points and control coefficients. The accuracy of the data fitting is documented in the experimental result section. After obtaining high-quality DSVSS volume representation of the brain model, we can use it to simulate brain deformation during surgery for computer-assisted surgical planning/surgery, or even for an innovative simulation-based diagnosis for brain injury under blunt impact.

5.5.2 Brain Shifting during Surgery

As known by brain surgery professionals, after a patient's skull is open, the brain will behave increasing deformation, known as brain shifting, during ongoing surgical procedures, predominantly due to the gravity and the drainage of cerebrospinal fluid. This will inevitably lead to the repositioning of the surgical targets embedded in brain. As a compensation to increase the spatial accuracy of modern neuronavigation systems, intraoperative magnetic resonance imaging (IMRI) is widely used for quantitative analysis and visualization of this phenomenon [50]. Nevertheless, despite its virtually real-time aspects, IMRI only provides very low-resolution intraoperative MR image which can never substitute the high-resolution pre-operative SPGR MR image used to determine with high accuracy key dimensions of the brain and the locations of the surgical targets embedded in the brain. We employ our dynamic spherical volumetric simplex splines model into the brain simulation to compute the brain shifting.

In our framework, brain shifting can be simulated by applying constant gravity force \vec{G} to the brain. The material properties that we used in our experiments were obtained from *the bio-*

mechanics group at Wayne State University (WSU). After setting up the physical parameters of an individual brain, we also need to take the nature boundary of the brain, the skull, into consideration. The fact is that no matter what manner the brain behaves deformation, it lies inside the skull, i.e., its nature boundary will not exceed the skull. Therefore, spatial geometric constraints need to be enforced. We add the soft constraints with forces. When there is shifting outside the boundary, we insert corresponding forces along the opposite direction of the movement to the simulation procedure.

Figure 5.7 illustrates the brain shifting simulation using our framework when taking out the resected skull over the right temporal lobe. The green contour shows the deformation clearly. Our shifting simulation results highly agree with the fact captured by IMRI. The experiments show that it is effective to use our model to recover motion and deformation from image data. Based on 20 simulation experiments, quantitative comparison between the IMRI volumes and our simulated brain volumes by co-registration shows that our system can achieve an excellent accuracy of 92.2%. The accuracy of a single simulation, denoted by A , is calculated as the normalized sum of squared differences between the two volumes,

$$A = 1 - \frac{\sum_a \|S - R\|^2}{\sum_a \|R\|^2}, \quad (5.26)$$

where S is the volume obtained from our shifting simulation results and R is the registered IMRI volume. To make the comparison substantial and intra-sequence, we first register MRI volume to IMRI volume. *Figure 5.8* depicts another brain shifting simulation. The skull is resected over the left temporal lobe. The color map is blended into the figure to better visualize the deformation scale. Note that, when surgical tools are operating in the brain, there will be larger shifting and deformation.

As demonstrated from the available comparison and evaluation, our framework can accurately simulate the deformation of the brain (e.g., $\mathbf{s}(t)$) and simultaneously present high-quality and high-resolution visualization using the transformed SPGR image intensities, \mathbf{I} , modeled in

the reconstructed simplex spline volume (see *Equation 5.25*). It is very promising to use the framework in both surgical planning (e.g., predicting the shifting of the targets) and computer-assisted surgery (e.g., repositioning the targets with high-resolution display, \mathbf{I} , automatically computed based on the realistic deformation of the reconstructed brain, $\mathbf{s}(t)$).

5.5.3 Brain Injury Prediction

Here, we refer the brain injury prediction as a procedure of finding out the extent and location of the injury in the brain during a blunt impact. The injury frequently occurs to automobiles drivers during the collision and sports players during the acute sports activities such as football. Current brain surgeons and professionals rely indispensably on those modern neuroimaging and neuronavigation systems to pinpoint the injury. Clinically, the identification of the site and extend of injury within the brain without subjecting the patient to an imaging scanning, has its advantages. For instance, head injured patients are difficult to control and may not remain still long enough for the completion of the scanning. In some severe cases, time is so limited that patients even can not afford such a pre-operative scanning. Thus the demand of simulation-based Computer Aided Diagnosis (CAD) solution goes up to high gear. Oftentimes, the solution is referred as “brain injury modeling”.

One critical issue about BIM technique is to derive a patient-specific brain model based on a template model, thus skipping neuroimaging and neuronavigation, and saving computational time as well as pre-operation time. One widely employed way is to modify the exterior surface of each substructure from a general brain model followed by re-generation of the mesh. Ferrant *et al.* [17] and Miga *et al.* [47] developed their approaches respectively using this approach by meshing the entire brain without considering anatomical structures and material difference. Obviously, this approach is not accurate since the brain geometry, structures, and heterogeneous material variations are not considered. We employ our dynamic spherical simplex splines-based simulation framework to handle the situation. As for developing a patient-specific model, our method can quickly modify the control points/coefficients according to the

data fitting of the available data or information of the patient.

In our framework, we compute the stress field of the human brain under blunt impact using our DSVSS volume. Because the human brain has highly heterogeneous physical properties in different areas of the brain, such as the white matters, the gray matters, the cerebellum, the brainstem, the lateral ventricles, the third ventricles, the bridge veins, and so on. From this perspective, brain structures under direct impact are not necessarily the parts where brain injuries occur. With our unified solid representation through dynamic spherical volumetric simplex splines, blunt-impact injury can be simulated using our framework by applying an instantaneous impact to the brain model under given approximate impact conditions. The model incorporated in our framework can not only assist the physician in identifying the location and extend of damaged area without pre-operative scanning but also enable the designer of automobiles and helmets to improve the human-centered design of head-protective facilities.

Figure 5.9 demonstrates a brain injury prediction with a blunt impact on the frontal lobe. Time interval here is 3ms. Note that, we assume that the brain always lies inside the skull during the simulation. As in brain shifting simulation, we add corresponding contacting forces into the simulation when the brain is shifting outside the boundary. The corresponding contacting forces is along the opposite direction and linear to the extent of the brain movement. *Figure 5.9-(b-j)* shows the stress fields of the brain in each time step. Redder area indicates higher stress, which is a sign for a higher possibility of injury and bleeding. In the figure, the thalamus is under bigger stress as well beside the place under direct blunt impact. The result complies with the ground truth captured from the real biomechanic experiments on a human corpus model. Quantitative evaluation of our simulation result is obtained through the comparison with the ground truth.

Figure 5.10 shows two stress evolution curves of one landmark inside right thalamus under the specified blunt impact in *Figure 5.9*. The green one is the ground truth obtained from the real biomechanic experiments and the red one is the result simulated using our framework. The

result curves demonstrated that our simulation can obtain an accurate and satisfactory result, which has great potential for computer-aided diagnosis of brain injury under blunt impact.

Figure 5.11 illustrates another experiment regarding brain injury prediction. A different patient is undergoing a similar blunt impact on the left frontal lobe. The simulation shows that besides the spot under direct impact, the thalamus is another area where bleeding may happen, which also coincides with the ground truth fact.

5.6 Experimental Results

We have implemented a prototype system on a Dell Precision Workstation T7400, which has dual Xeon CPUs with Quad Cores and 4GB RAM. The system is written in VC++ and VTK 4.2. We perform experiments on several brain datasets. In order to compare the reconstruction qualities for patient-specific cases, we uniformly sample the brain geometric and physical fields into a unit cube.

Table 5.1 shows the configuration of DSMSS volumes reconstructed from different datasets. The performance statistics of our fitting algorithm is also included. From the table, one can observe that, compared with discrete mesh representation, our spherical multivariate simplex spline based representations have low storage requirements and can achieve high accuracy, e.g., fitting r.m.s. error $\leq \times 10^{-4}$. High computational cost is the challenging aspect of our algorithm. However, in practice, by applying multiresolution and multi-thread implementation of the geometric elements, the time cost can be greatly reduced.

Subject	Degree	Data Points	Tetrahedra	Control Points	Knots	Fitting Error
A	2	60298	2500	3871	1683	3.0375×10^{-4}
B	3	72357	2500	12431	2244	2.1483×10^{-4}
C	2	79593	4320	6525	2769	1.9743×10^{-4}
D	3	86226	4320	21117	3682	1.5290×10^{-4}

Table 5.1: Statistics of 3D reconstruction of brain models. The fitting error is presented by root-mean-square error.

Table 5.2 shows the performance of DSMSS framework applied to brain datasets. Both

brain biomechanic behaviors, brain shifting and brain injury, are simulated. Note that all the units in this table are metric. In the table, only the physical properties of white matter are listed. For the physical properties of different type of brain tissues, readers are referred to [106]. The averaged, overall computational time for the entire simulations demonstrated in *Figure 5.8* (brain shifting) and *Figure 5.9* or *Figure 5.11* (brain injury simulation) are listed in the table. Faster overall computations can be achieved by increasing the simulation time interval. The simulation results on brain shifting and brain injury prediction have been already illustrated in *Chapter 5.5*. Overall, our brain simulation results exhibit a reliable approximation of how brain behaves shifting and how brain could be injured in the real world when inputting the real material parameters.

Application	μ (kg/m^3)	γ ($1/s$)	α (GPa)	β (GPa)	Δt (ms)	Time ($hh : mm : ss$)
Shifting Simulation	1.04×10^{-6}	400	0.6570	0.2266	75	00:24:20
Impact Simulation	1.04×10^{-6}	400	0.6570	0.2266	3	00:22:33

Table 5.2: Physical parameters and statistics of brain biomechanic simulations.

5.7 Comparison with Existing Methods

In this section, we will briefly compare our object simulation paradigm with other object simulation schemes. As there are quite a lot literature on this research topic, I only choose several of them as the representative ones.

Authors	Volume Representation	High-genus Support
Welch and Witkin [104]	B-Spline Based Free-Form Deformation	Trimming and Patching
Terzopoulos and Qin [93]	Dynamic NURBS	Trimming and Patching
Qin and Terzopoulos [64]	Dynamic Triangular B-Spline	Naturally Supportive
Our Method	Dynamic Multivariate Simplex Spline	Naturally Supportive

Table 5.3: Comparison of object simulation schemes.

As we may see from the table, B-spline and its variances are widely employed as the un-

derlying volume representation schemes. However, its natural deficiency, the tensor product nature, greatly hinders its application. Dynamic bivariate simplex spline is ideal for surface simulation but incompetent for 3D object simulation. Our unrival physically based modeling and simulation scheme is based on multivariate simplex spline which is a true non-tensor product method with the best accuracy and high-genus support.

5.8 Summary

In this chapter, we have developed a novel simulation framework based on dynamic spherical multivariate simplex splines. We have introduced an automatic and accurate algorithm to fit the digital models of real-world objects with a single spherical multivariate simplex spline which can represent with accuracy geometric and material properties of objects simultaneously. With the integration of the Lagrangian mechanics, the dynamic multivariate simplex spline representing the real-world object can accurately simulate its physical behavior. We have applied the framework in the biomechanics simulation of the brain, such as brain shifting during the surgery and brain injury under sudden impact. We have compared the simulated results with the ground truth obtained through interactive magnetic resonance imaging and the ground truth from real biomechanic experiments. The experimental results have demonstrated the excellent performance of our technique, which can be effectively used in deformation-based brain simulation and simulation-based diagnosis/assessment. The robustness and accuracy result from the tight integration of the geometric and material properties into the simulation. In the near future, we will investigate more powerful simulation schemes based on our novel digital representations. Hierarchical simulation will also be explored to speed up the simulation for real-time applications. On the application side, we will develop a DSMSS model of an entire head, which allows us to simulate more sophisticated behaviors of the brain.

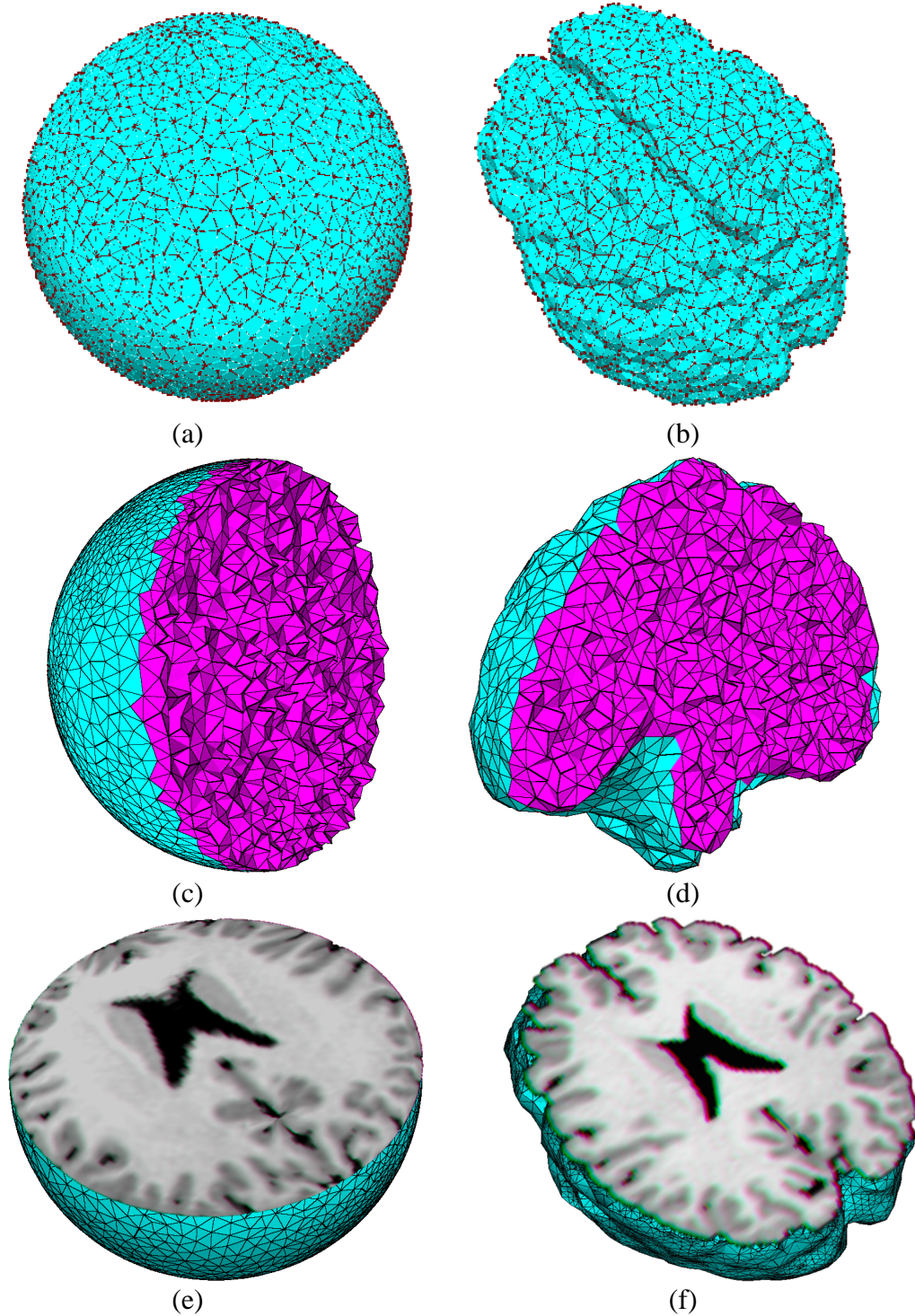


Figure 5.4: (a) The discretized point set in the spherical domain space; (b) The discretized data point set in the physical space, from the same angle of view as (a); (c-f) The shapes are cut into halves sagittally (c-d) and axially (e-f) in order to show the interior mapping between the parametric domain and the physical object.

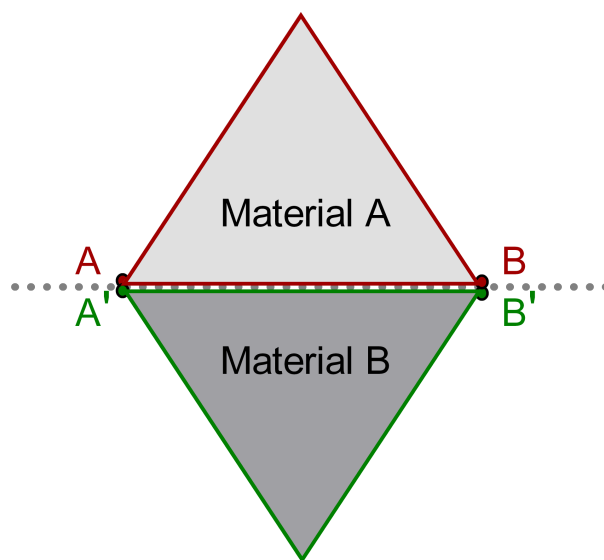


Figure 5.5: Modeling discontinuities with separated domain triangles. Even though A and A' are co-located, and B and B' are co-located, the domain triangles in red and green are belonged to two different domains.

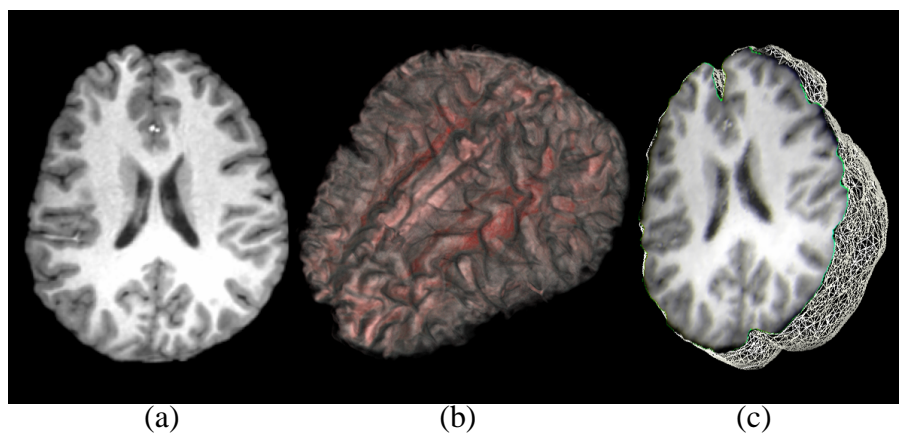


Figure 5.6: (a) An axial view of a slice high-resolution brain SPGR MRI dataset; (b) Volume visualization of the reconstructed DSVSS volume; (c) The volume is split to show its reconstructed interior intensities.

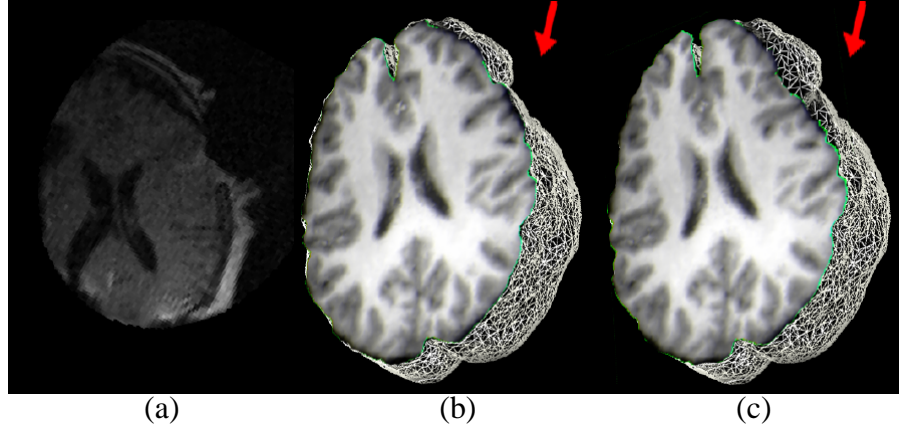


Figure 5.7: (a) One slice view of IMRI image; (b) The reconstructed DSVSS volume, where the cross-sectional view displays the DSVSS-captured image intensities reconstructed from the pre-operative high-resolution SPGR images; (c) The brain deformation simulated using our system, where the cross-sectional view is captured, from the same view angle as (b), to show the displacement from (b), and the green contour indicates the extent of displacement at the boundary. In (b) and (c) the red arrow denotes the orientation of gravity, and its position denotes the resected skull.

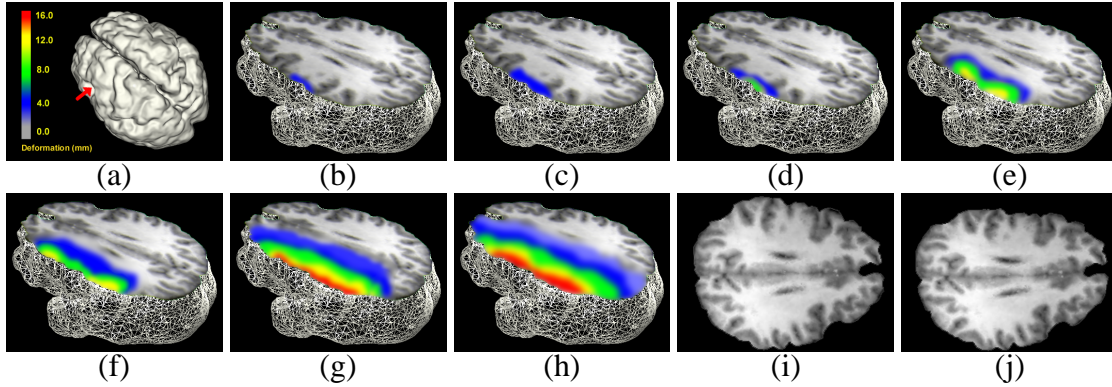


Figure 5.8: (a) The color map used to describe the deformation scale. The red arrow on the ISO-surface indicates the position where skull is resected; (b-h) Brain shifting simulation with a time interval of 75ms; (i-j) To better visualize the deformation, cross-section views of the first key frame (b) and last one (h) are retrieved. Deformed junction between the two hemispheres indicates the global brain shifting.

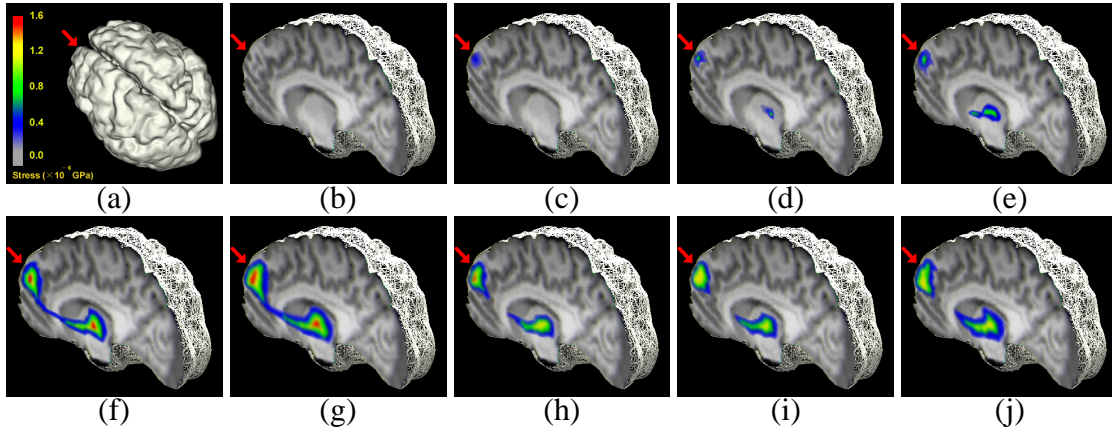


Figure 5.9: (a) The color map used to describe the stress field. The red arrow on the ISO-surface indicates the position where a blunt impact occurs; (b-j) Brain injury simulation with a time interval of 3ms. The blunt impact occurs at the front lobe. Simulation results indicate that in addition to the spot directly under the impact, there are some other positions where bleeding may happen.

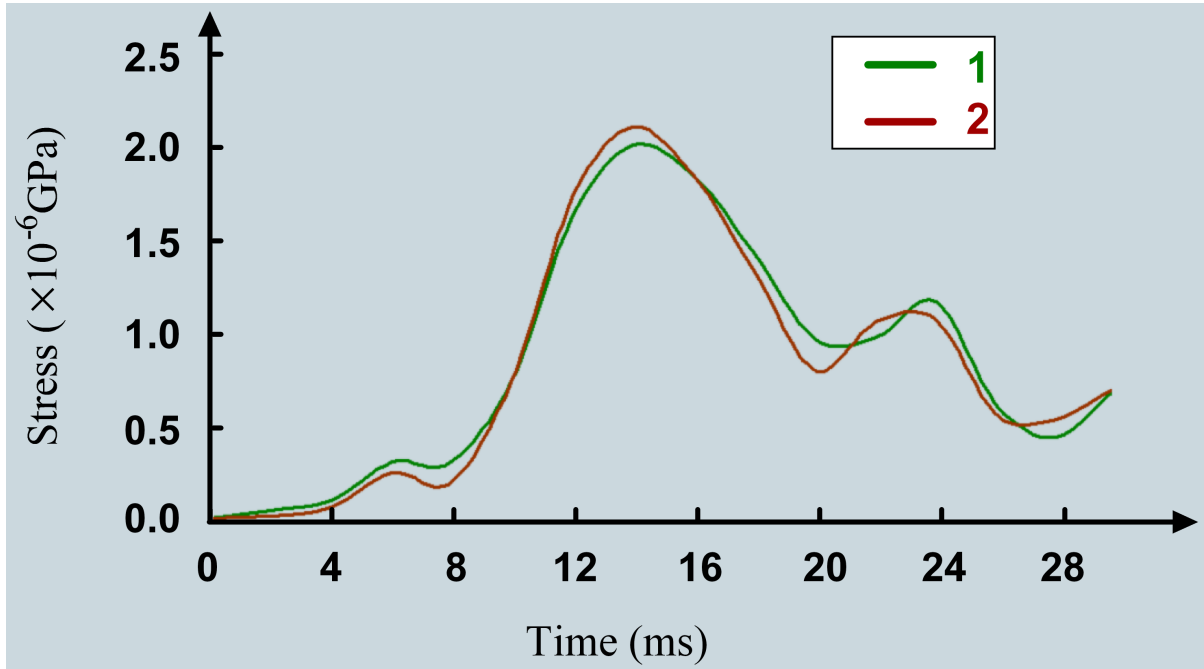


Figure 5.10: Comparison of stress evolutions of the right thalamus under a blunt impact. The green one is the simulation curve obtained from the real biomechanic experiments and the red one is the result simulated using our framework.

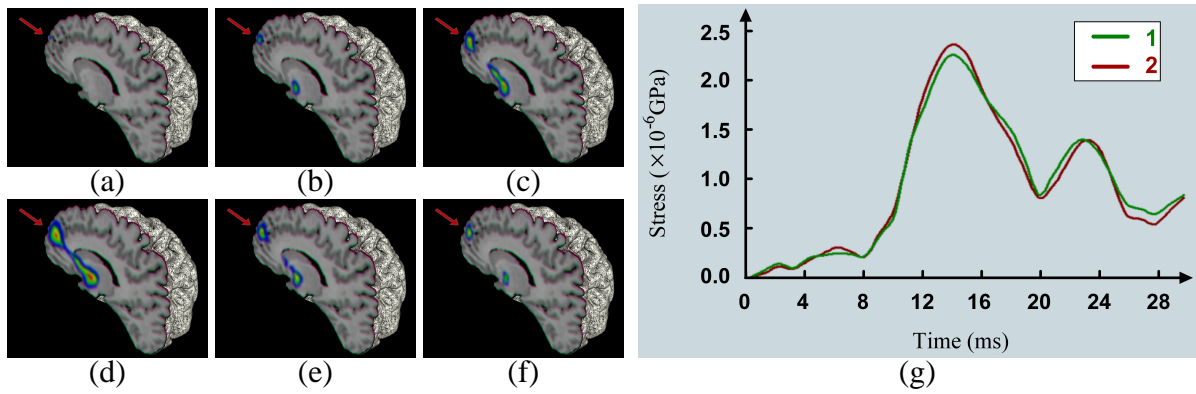


Figure 5.11: (a-f) Another brain injury simulation with a time interval of 3ms. The blunt impact occurs at the left front lobe; (g) Comparison of stress evolutions of the right thalamus under the blunt impact.

CHAPTER 6: CONCLUSION

The purpose of this chapter is twofold. We first summarize the contributions made by this dissertation, then we point towards the future work.

6.1 Contributions

In this dissertation, we are dedicated to present a general volume representation and modeling framework which employs dynamic multivariate simplex splines as its mathematic foundation. We have made contributions in different volume-related research topics, such as volume reconstruction, nonrigid volume registration, and physically based modeling and simulation.

1. *Volume Reconstruction from 2D Images with Multivariate Simplex Splines (Chapter 3).*

This part developed a new integral approach for representing, modeling, and reconstructing volume data with a hierarchical multivariate simplex spline model. The model is defined over a hierarchical and progressive tetrahedralization of arbitrary 3D domains. Our framework supports both structured and unstructured data. The modeled volume can be of complicated geometry and arbitrary topology. We have developed a new paradigm to reconstruct non-discrete models from a sequence of 2D images. With the flexible hierarchical structures, our method can adaptively refine the domain tetrahedralization and introduce more degrees of freedom locally for better fitting results. The volumes can then be re-modeled and re-edited by manipulating the control vectors and/or associated knots of multivariate simplex splines easily. Our results demonstrate that multivariate simplex spline is a powerful volume representation and modeling scheme with new and unique advantages which can be applied to diverse research areas.

2. *Nonrigid Volume Registration with Multivariate Simplex Spline Based Free-Form Deformation (Chapter 4).* This part presented a novel nonrigid volume registration paradigm using multivariate simplex spline based free-form deformation. Although multivariate

simplex has already been a powerful tool in both engineering and medical research realm, it has never been applied to the intramodality nonrigid volume registration. Our approach first embedded the floating volume into the control space associated with its multivariate simplex spline. With the guidance of normalized mutual information between the floating and the reference volume, a rigid affine transformation is applied to the control points of the control space, to obtain an initial rigid alignment. After that, a local, nonrigid multivariate simplex spline based free-form deformation was applied to the floating volume. We introduce normalized mutual information, volume preserving term and smoothness term to achieve better registration result. The experimental results have demonstrated that multivariate simplex spline volumes are ideal for deformation-based brain registration as well as other medical imaging registration.

3. *Physically Based Modeling and Simulation with Dynamic Spherical Multivariate Simplex Splines (Chapter 5)*. This part proposed a novel physically based modeling and simulation framework based on dynamic spherical multivariate simplex splines. We have introduced an automatic and accurate algorithm to fit the digital models of real-world objects with a single spherical multivariate simplex spline which can represent with accuracy geometric and material properties of objects simultaneously. With the integration of the Lagrangian mechanics, the dynamic multivariate simplex spline representing the real-world object can accurately simulate its physical behavior. We have applied the framework in the biomechanics simulation of the brain, such as brain shifting during the surgery and brain injury under sudden impact. We have compared the simulated results with the ground truth obtained through interactive magnetic resonance imaging and the ground truth from real biomechanic experiments. The experimental results have demonstrated the excellent performance of our technique, which can be effectively used in deformation-based brain simulation and simulation-based diagnosis/assessment.

These contributions are described in more detail and validated in the main body of the dissertation. Please refer to the corresponding chapters for details.

6.2 Future Work

This dissertation work also opens several venues for future work, with the focus on volume representation and modeling.

1. *Large Scale Deformed Volume Registration Using Surface Constrained 3D Mean Value Coordinates Interpolation.* Most of the current volume registration methods can only deal with volumes with small deformation. Volume registration with large scale deformation has been a severely under-explored research area for long time. One case in point is breast disease diagnosis. As the human breast is the most deformed organ while the subject's position is changed from supine to prone. The large scale deformation during the surgery will fail due to model inadequacy. In stead, I plan to investigate a novel volume registration method, where large scale deformation is presented between the volumes, using surface constrained 3D mean value coordinates interpolation.
2. *Hierarchical Simulation of Biomedical Behaviors of Human Organs.* Human organs are usually heterogenous models of complex geometry and arbitrary topology. Current prevalent human organ simulation schemes often employ traditional linear and nonlinear finite element methods which are computationally expensive. Visualization of the organ models usually require other representation schemes. This inconvenience further reduces the flexibility of the traditional methods and greatly limits other downstream applications. Instead, I plan to investigate a more powerful simulation schemes of human organs using dynamic multivariate simplex spline based digital volume representation. Multivariate simplex spline's native non-tensor product property makes it ideal for multiresolution modeling of heterogenous human organ models of complicated geometry and topology. To further reduce the computational cost, hierarchical simulation will be

explored to speed up the simulation for real-time applications.

These new research areas may not follow explicitly from this dissertation, however, we should take the new understanding of our proposed powerful volume representation and modeling framework gained through this dissertation into account.

APPENDIX

Publications

• *Journals*

- [1] **Y. Tan**, J. Hua and H. Qin, “Physically Based Modeling and Simulation with Dynamic Spherical Volumetric Simplex Splines”, *Computer-Aided Design*, 2009, DOI:10.1016/J.CAD.2009.02.014.
- [2] **Y. Tan**, J. Hua and M. Dong, “3D Reconstruction from 2D Images with Hierarchical Continuous Simplices”, *The Visual Computer*, 2007, vol. 23, no. 9-11, pp. 905-914.

• *Conferences*

- [3] **Y. Tan**, J. Hua and H. Qin, “Dynamic Spherical Volumetric Simplex Splines with Applications in Biomedical Simulation”, in *Proc. of ACM Solid and Physical Modeling Symposium*, 2008, pp. 103-119. (Note: This article was invited as one of the best papers to *Computer-Aided Design*.)
- [4] **Y. Tan**, J. Hua and M. Dong, “3D Reconstruction from 2D Images with Hierarchical Continuous Simplices”, in *Proc. of Computer Graphics International*, 2007. (Note: This article was invited as one of the best papers to *The Visual Computer*.)
- [5] **Y. Tan**, J. Hua and M. Dong, “Feature Curve-guided Volume Reconstruction from 2D Images”, in *Proc. of 2007 IEEE International Symposium on Biomedical Imaging: From Nano to Macro*, 2007, pp. 716-719.
- [6] **Y. Tan**, J. Ren, W. Ren and J. Hua, “Correlation Analysis between 3D Histology and microCT Imaging for Non-invasive Diagnosis of Osteolysis”, in *The Annual Joint Molecular Imaging Conference*, 2007, extended abstract.
- [7] W. Ren, O. Muzik, T. Mongner, P. Chakraborty, **Y. Tan**, B. Wu and J. Hua, “Assessing

Implant Wear-Induced Inflammation Using PET[^{11}C] PK11195 Imaging in a Rat Model of Knee Joint Replacement”, in *The 53rd Annual Meeting of the Orthopaedic Research Society*, 2007, extended abstract.

- ***Submitted Papers***

[8] **Y. Tan**, R. Liao, A. Kamen, H. Sundar, M. Pfister and J. Hua, “Deformable 2D/3D Registration for Abdominal Aortic Aneurysm Interventions”, submitted to *The 13th International Conference on Medical Image Computing and Computer Assisted Intervention*, 2010.

[9] **Y. Tan** and J. Hua, “Nonrigid Volume Registration Using Multiresolution Volumetric Simplex Spline Based Free-Form Deformation”, submitted to *SPM 2010: ACM Solid and Physical Modeling Symposium*, 2010.

- ***Papers in Preparation***

[10] **Y. Tan**, J. Hua and J. Ren, “A Unified Correlation Scheme between 3D Histology and microCT Volume”, planned submission to *IEEE Transactions on Medical Imaging*, 2010.

[11] **Y. Tan** and J. Hua, “Registration of Volumetric Objects with Large Deformations Using Surface Constrained 3D Mean Value Coordinates Interpolation”, planned submission to *IEEE Transactions on Medical Imaging*, 2010.

BIBLIOGRAPHY

- [1] BARDINET, E., OURSELIN, S., MALANDAIN, G., TANDE, D., PARAIN, K., AYACHE, N., AND YELNIK, J. Three dimensional functional cartography of the human basal ganglia by registration of optical and histological serial sections. In *Proceedings of IEEE International Symposium on Biomedical Imaging* (2002), pp. 329–332.
- [2] BLOOR, M., AND WILSON, M. Representing PDE surfaces in terms of B-splines. *Computer-Aided Design* 22, 6 (1990), 324–331.
- [3] BRAID, I. *Notes on a geometric modeller*. Shape Data Limited, 1980.
- [4] CELNIKER, G., AND GOSSARD, D. Deformable curve and surface finite elements for free-form shape design. *Computer Graphics* 25, 4 (1991), 257–266.
- [5] CHAN, H., AND CHUNG, A. Efficient 3d-3d vascular registration based on multiple orthogonal 2d projections. In *Second International Workshop on Biomedical Image Registration(WBIR 2003)* (2003), vol. 2717, pp. 301–310.
- [6] CHEN, H., AND VARSHNEY, P. Mutual information-based CT-MR brain image registration using generalized partial volume joint histogram estimation. *IEEE Transactions on Medical Imaging* 22, 9 (2003), 1111–1119.
- [7] CHOI, S., LEE, J., KIM, J., AND KIM, M. Volumetric object reconstruction using the 3d-mrf model-based segmentation. *IEEE Transactions on Medical Imaging* 16, 6 (1997), 887–892.
- [8] CIGNONI, P., CONSTANZA, D., MONTANI, C., ROCCHINI, C., AND SCOPIGNO, R. Simplification of tetrahedral meshes with accurate error evaluation. In *Proceedings of the conference on Visualization '00* (2000), pp. 85–92.

- [9] CIGNONI, P., DE FLORIANI, L., MONTANI, C., PUPPO, E., AND SCOPIGNO, R. Multiresolution modeling and visualization of volume data based on simplicial complexes. In *Proceedings of the 1994 Symposium on Volume Visualization* (1994), pp. 19–26.
- [10] COATS, B., AND MARGULIES, S. Material properties of porcine parietal cortex. *Journal of Biomechanics* 39 (2006), 2521–2525.
- [11] COLLIGNON, A., MAES, F., DELAERE, D., VANDERMEULEN, D., SEUTENS, P., AND MARCHAL, G. Automated multimodality image registration using information theory. In *Proceedings of the International Conference on Information Processing in Medical Imaging* (1995), pp. 263–274.
- [12] COLLINS, D., EVANS, A., HOLMES, C., AND PETERS, T. Automatic 3D segmentation of neuro-anatomical structures from MRI. In *Proceedings of the International Conference on Information Processing in Medical Imaging* (1995), pp. 139–152.
- [13] DAHMEN, W., MICCHELLI, C., AND SEIDEL, H.-P. Blossoming begets B-spline bases built better by B-patches. *Mathematics of Computation* 59, 199 (1992), 97–115.
- [14] DE BOOR, C. Splines as linear combinations of B-splines. In *Approximation Theory II* (1976), Academic Press, New York, pp. 1–47.
- [15] EDELSBRUNNER, H. *Geometry and Topology for Mesh Generation*. Cambridge University Press, 2001. Edited by P.G.Ciarlet and A.Iserles and R.V.Kohn and M.H.Wright.
- [16] EDWARDS, P., HILL, D., LITTLE, J., AND HAWKES, D. A threecomponent deformation model for image-guided surgery. *Medical Image Analysis* 2 (1998), 355–367.
- [17] FERRANT, M., WARFIELD, S., NABAVI, A., JOLESZ, F., AND KIKINIS, R. Registration of 3D intraoperative MR images of the brain using a finite element biomechanical model. In *MICCAI* (2000), pp. 19–28.

- [18] GEFEN, A., AND MARGULIES, S. Are in vivo and in situ brain tissues mechanically similar? *Journal of Biomechanics* 37 (2004), 1339–1352.
- [19] GIBSON, S., AND MIRTICH, B. A survey of deformable modeling in computer graphics. In *Technical Report TR-97-19* (1997).
- [20] GOSSICK, B. *Hamilton's principle and physical systems*. Academic Press, 1967. New York and London.
- [21] GREINER, G., AND SEIDEL, H.-P. Modeling with triangular B-splines. *IEEE Computer Graphics and Applications* 14, 2 (1994), 56–60.
- [22] GU, X., WANG, Y., CHAN, T., THOMPSON, P., AND YAU, S. Genus zero surface conformal mapping and its application to brain surface mapping. In *Information Processing in Medical Imaging* (2003), pp. 172–184.
- [23] HAGEMANN, A., ROHR, K., STIEHL, H., SPETZGER, U., AND GILSBACH, J. Biomechanical modeling of the human head for physically based, nonrigid image registration. *IEEE Transactions on Medical Imaging* 18 (1999), 875–884.
- [24] HALSTEAD, M., KASS, M., AND DEROSE, T. Efficient, fair interpolation using catmull-clark surfaces. In *Computer Graphics Proceedings, Annual Conference Series, Proc. ACM Siggraph93* (1993), pp. 35–44.
- [25] HUA, J., HE, Y., AND QIN, H. Multiresolution heterogeneous solid modeling and visualization using trivariate simplex splines. In *Proceedings of the Ninth ACM Symposium on Solid Modeling and Applications* (2004), pp. 47–58.
- [26] HUA, J., HE, Y., AND QIN, H. Trivariate simplex splines for inhomogeneous solid modeling in engineering design. *ASME Transactions: Journal of Computing and Information Science in Engineering* 5, 2 (2005), 149–157.

- [27] HUA, J., AND QIN, H. Haptic sculpting of volumetric implicit functions. In *Proceedings of the Ninth Pacific Conference on Computer Graphics and Applications (Pacific Graphics)* (2001), pp. 254–264.
- [28] HUA, J., AND QIN, H. Haptics-based volumetric modeling using dynamic spline-based implicit functions. In *Proceedings of IEEE Symposium on Volume Visualization and Graphics* (2002), pp. 55–64.
- [29] HUA, J., AND QIN, H. Haptics-based dynamic implicit solid modeling. In *IEEE Trans. on Visualization and Computer Graphics* (2003), vol. 10.
- [30] JAMES, D., AND PAI, D. Artdefo: Accurate real time deformable objects. In *Proceedings of SIGGRAPH'99* (1999), pp. 65–72.
- [31] KANG, H., WILLINGER, R., DIAW, B., AND CHINN, B. Modeling of the human head under impact conditions: A parametric study. In *Proceedings of 41th Stapp Car Crash Conference* (1997).
- [32] KARDESTUNCER, H. *Finite Element Handbook*. McGraw-Hill, 1987. New York.
- [33] KRINIDIS, S., NIKOU, C., AND PITAS, I. 3d volume reconstruction by serially acquired 2d slices using a distance transform-based global cost function. *Methods and Applications of Artificial Intelligence* 2308 (2002), 390–400.
- [34] LEE, S., AND BAJCSY, P. Feature based registration of fluorescent lscm imagery using region centroids. In *Proceedings of SPIE International Symposium in Medical Imaging* (2005), vol. 5747, pp. 170–181.
- [35] LEE, S., AND BAJCSY, P. Three-dimensional volume reconstruction based on trajectory fusion from confocal laser scanning microscope images. In *Proceedings of IEEE Conference on Computer Vision and Pattern Recognition (CVPR 06)* (2006), vol. 2, pp. 2221–2228.

- [36] LI, X., GUO, X., WANG, H., HE, Y., GU, X., AND QIN, H. Harmonic volumetric mapping for solid modeling applications. In *In Proceedings of the 2007 ACM Symposium on Solid and Physical Modeling (SPM'07)* (2007), pp. 109–120.
- [37] LIU, C., HU, S., GU, J., YANG, J., AND YU, M. Brain image registration based on entropy of mutual information matrix. In *Canadian Conference on Electrical and Computer Engineering* (2007), pp. 1163–1166.
- [38] MAES, F., COLLIGNON, A., VANDERMEULEN, D., MARECHAL, G., AND SUETENS, P. Multimodality image registration by maximization of mutual information. *IEEE Transactions of Medical Imaging* 16, 2 (1997), 187–198.
- [39] MAGUIRE, G., NOZ, M., RUSINEK, H., JAEGER, J., KRAMER, E., SANGER, J., AND SMITH, G. Graphics applied to medical image registration. In *IEEE Computer Graphics Application* (1991), vol. 11, pp. 20–28.
- [40] MANDAL, C., QIN, H., AND VEMURI, B. C. A novel fem-based dynamic framework for subdivision surfaces. In *Proceedings of the 5th ACM Symposium on Solid Modeling and Applications* (1999), pp. 191–202.
- [41] MARTIN, W., AND COHEN, E. Representation and extraction of volumetric attributes using trivariate splines: A mathematical framework. In *Proceedings of the 7th ACM Symposium on Solid Modeling and Applications* (2001), pp. 234–240.
- [42] McDONNELL, K., QIN, H., AND WLODARCZYK, R. Virtual clay: A real-time sculpting system with haptic toolkits. In *Proceedings of ACM Symposium on Interactive 3D Graphics* (2001), pp. 179–190.
- [43] MEAGHER, D. Geometric modeling using octree encoding. In *IEEE Computer Graphics and Application* (1982), vol. 19, pp. 129–147.

- [44] METAXAS, D., AND TERZOPOULOS, D. Dynamic deformation of solid primitives with constraints. In *Computer Graphics* (1992), vol. 26, pp. 309–312.
- [45] MEYER, C., BOES, J., KIM, B., BLAND, P., ZASADNY, K., KISON, P., KORAL, K., FREY, K., AND WAHL, R. Demonstration of accuracy and clinical versatility of mutual information for automatic multimodality image fusion using affine and thin-plate spline warped geometric deformations. *Medical Image Analysis* 1, 3 (1997), 195–207.
- [46] MICCHELLI, C. On a numerically efficient method for computing with multivariate B-splines. *Multivariate Approximation Theory* (1979), 211–248.
- [47] MIGA, M., SINHA, T. K., CASH, D. M., GALLOWAY, R., AND WEIL, R. Cortical surface registration for image-guided neurosurgery using laser-range scanning. *IEEE Transactions on Medical Imaging* 22, 8 (2003), 973–985.
- [48] MORETON, H., AND SEQUIN, C. Functional optimization for fair surface design. *Computer Graphics* 26, 2 (1992), 167–176.
- [49] MYERS, R. The application of PET-MR image registration in the brain. *The British Journal of Radiology* 75 (2002), S21–S35.
- [50] NIMSKY, C., GANSLANDT, O., CERNY, S., HASTREITER, P., GREINER, G., AND FAHLBUSCH, R. Quantification of, visualization of, and compensation for brain shift using intraoperative magnetic resonance imaging. *Neurosurgery* 47, 5 (2000), 1070–1080.
- [51] NÜRNBERGER, G., SCHUMAKER, L., AND ZEILFELDER, F. Lagrange interpolation by c^1 cubic splines on triangulated quadrangulations. *Adv. Comp. Math.* (2004).
- [52] NÜRNBERGER, G., AND ZEILFELDER, F. Lagrange interpolation by bivariate c^1 -splines with optimal approximation order. *Adv. Comp. Math.* (2004).

- [53] OHTAKE, Y., BELYAEV, A., ALEXA, M., TURK, G., AND SEIDEL, H.-P. Multi-level partition of unity implicits. In *SIGGRAPH'03* (2003), pp. 463–470.
- [54] PAI, D. Strands: Interactive simulation of thin solids using cosserat models. In *Proceedings of Eurographics* (2002), pp. 347–352.
- [55] PARK, S., AND LEE, K. High-dimensional trivariate NURBS representation for analyzing and visualizing fluid flow data. In *Computer and Graphics* (1997), vol. 21, pp. 473–482.
- [56] PAULY, M., GROSS, M., AND KOBBELT, L. Efficient simplification of point-sampled surfaces. *IEEE Visualization 02 Proceedings* (2002), 163–170.
- [57] PAULY, M., KEISER, R., KOBBELT, L., AND GROSS, M. Shape modeling with point-sampled geometry. *SIGGRAPH 03 Proceedings* (2003), 641–650.
- [58] PENTLAND, A., AND WILLIAMS, J. Good vibrations: Modal dynamics for graphics and animation. In *Computer Graphics* (1989), vol. 23, pp. 215–222.
- [59] PFEIFLE, R., AND SEIDEL, H.-P. Fast evaluation of quadratic bivariate DMS spline surfaces. In *Proceedings of Graphics Interface '94* (1994), pp. 182–189.
- [60] PFEIFLE, R., AND SEIDEL, H.-P. Fitting triangular B-splines to functional scattered data. In *Proceedings of Graphics Interface '95* (1995), pp. 80–88.
- [61] PFEIFLE, R., AND SEIDEL, H.-P. Scattered data approximation with triangular B-splines. *Advance Course on Fairshape* (1996), 253–263.
- [62] PRESS, W., FLANNEY, B., TEUKOLSKY, S., AND VETTERLING, W. *Numerical Recipes: The Art of Scientific Computing*. Cambridge University Press, 1986. Cambridge.

- [63] QIN, H., MANDAL, C., AND VEMURI, B. Dynamic catmull-clark subdivision surfaces. *IEEE Transaction on Visualization and Computer Graphics* 4, 3 (1998), 215–229.
- [64] QIN, H., AND TERZOPOULOS, D. Dynamic manipulation of triangular B-splines. In *In Proceedings of Third Symposium on Solid Modeling and Applications (Solid Modeling '95)* (1995), pp. 351–360.
- [65] QIN, H., AND TERZOPOULOS, D. Dynamic NURBS with geometric constraints for physics-based shape design. *Computer Aided Design* 27, 2 (1995), 111–127.
- [66] QIN, H., AND TERZOPOULOS, D. D-nurbs: A physics-based framework for geometric design. *IEEE Transaction on Visualization and Computer Graphics* 2, 1 (1996), 85–96.
- [67] RAVIV, A., AND ELBER, G. Three dimensional freeform sculpting via zero sets of scalar trivariate functions. In *Proceedings of 5th ACM Symposium on Solid Modeling and Applications* (1999), pp. 246–257.
- [68] REQUICHA, A., AND VOELCKER, B. Historical summary and contemporary assessment. In *IEEE Computer Graphics and Applications* (1982), vol. 2, pp. 9–24.
- [69] ROHLFING, T., MAURER, C., BLUEMKE, D., AND JACOBS, M. Volume-preserving nonrigid registration of MR breast images using free-form deformation with an incompressibility constraint. *IEEE Transactions on Medical Imaging* 22, 6 (2003), 730–741.
- [70] ROSA, R., CHIRCO, P., AND MASSARI, R. Reconstruction corrections in advanced neutron tomography algorithms. *IEEE Transactions on Nuclear Science* 52, 1 (2005), 400–403.
- [71] RÖSSL, C., ZEILFELDER, F., NÜRNBERGER, G., AND SEIDEL, H.-P. Visualization of volume data with quadratic super splines. In *IEEE Visualization 2003* (2003), pp. 393–400.

- [72] RÖSSL, C., ZEILFELDER, F., NÜRNBERGER, G., AND SEIDEL, H.-P. Reconstruction of volume data with quadratic super splines. In *IEEE Trans. Vis. Comput. Graph* (2004), vol. 10, pp. 397–409.
- [73] RÖSSL, C., ZEILFELDER, F., NÜRNBERGER, G., AND SEIDEL, H.-P. Spline approximation of general volumetric data. In *ACM Symposium on Solid Modeling and Applications* (2004).
- [74] ROXBOROUGH, T., AND NIELSON, G. Tetrahedron based, least squares, progressive volume models with application to freehand ultrasound data. In *Proceedings of the conference on Visualization '00* (2000), pp. 93–100.
- [75] RUAN, J., KHALIL, T., AND KING, A. Human head dynamic reponse to side impact by finite element modeling. *Transactions of the ASME 113* (1991), 276–283.
- [76] RUECKERT, D., SONODA, L., HAYES, C., HILL, D., LEACH, M., AND HAWKES, D. Nonrigid registration using free-form deformations: Applications to breast mr images. *IEEE Transactions on Medcial Imaging 18*, 8 (1999), 712–721.
- [77] RVACHEV, V. Geometric applications of logic algebra. *Naukova Dumka* (1967).
- [78] SCHMITT, B., PASKO, A., AND SCHLICK, C. Constructive modeling of FRep solids using spline volumes. In *Proceedings of the 6th ACM Symposium on Solid Modeling and Applications* (2001), pp. 321–322.
- [79] SEIDEL, H.-P. An introduction to polar forms. *IEEE Computer Graphics and Applications 13*, 1 (1993), 38–46.
- [80] SEIDEL, H.-P. Polar forms and triangular B-spline surfaces. In *In Blossoming: The New Polar-Form Approach to Spline Curves and Surfaces, SIGGRAPH '91 Course Notes #26* (1994), pp. 235–286.

- [81] SHAPIRO, V. Real functions for representation of rigid solids. In *Technical Report TR91-1245* (1991).
- [82] SNYMAN, J. *Practical Mathematical Optimization: An Introduction to Basic Optimization Theory and Classical and New Gradient-Based Algorithms (Applied Optimization)*. Springer, 2005.
- [83] STUDHOLME, C., HILL, D., AND HAWKES, D. Multiresolution voxel similarity measure for MR-PET registration. In *Proceedings of the International Conference on Information Processing in Medical Imaging* (1995), pp. 287–298.
- [84] STUDHOLME, C., HILL, D., AND HAWKES, D. Automated three-dimensional registration of magnetic resonance and positron emission tomography brain images by multiresolution optimization of voxel similarity measures. *Medical Physics* 24 (1997), 25–35.
- [85] STUDHOLME, C., HILL, D., AND HAWKES, D. An overlap invariant entropy measure of 3D medical image alignment. *Pattern Recognition* 32, 1 (1998), 71–86.
- [86] SZELISKI, R., AND TONNESEN, D. Surface modeling with oriented particle systems. In *Proceedings of SIGGRAPH'92* (1992), pp. 185–194.
- [87] TAN, Y., HUA, J., AND DONG, M. 3D reconstruction from 2D images with hierarchical continuous simplices. *The Visual Computer* 23, 9-11 (2007), 905–914.
- [88] TAN, Y., HUA, J., AND DONG, M. Feature curve-guided volume reconstruction from 2d images. In *Proceedings of 2007 IEEE International Symposium on Biomedical Imaging: From Nano to Macro* (2007), pp. 716–719.
- [89] TAN, Y., HUA, J., AND QIN, H. Dynamic spherical volumetric simplex splines with applications in biomedical simulation. In *Proceedings of the ACM Solid and Physical Modeling Symposium (SPM 2008)* (2008), pp. 103–119.

- [90] TERZOPOULOS, D. Regularization of inverse visual problems involving discontinuities. In *IEEE Transactions on Pattern Analysis and Machine Intelligence* (1986), vol. 8, pp. 413–424.
- [91] TERZOPOULOS, D., AND FLEISCHER, K. Deformable models. *The Visual Computer* 4, 6 (1988), 306–331.
- [92] TERZOPOULOS, D., PLATT, J., BARR, A., AND FLEISCHER, K. Elastically deformable models. *Computer Graphics* 21, 4 (1987), 205–214.
- [93] TERZOPOULOS, D., AND QIN, H. Dynamic NURBS with geometric constraints for interactive sculpting. In *ACM Transactions on Graphics* (1994), vol. 13, pp. 103–136.
- [94] THIRION, J. Image matching as a diffusion process: An analogy with maxwells demons. *Medical Image Analysis* 2, 3 (1998), 243–260.
- [95] TING, T. *Anisotropic Elasticity*. Oxford University Press, 1996.
- [96] TONNESEN, D. Modeling liquids and solids using thermal particles. In *Proceedings of Graphics Interface* (1991), pp. 255–262.
- [97] TROTTS, I., HAMANN, B., AND JOY, K. Simplification of tetrahedral meshes with error bounds. *IEEE Trans. on Visualization and Computer Graphics* 5, 3 (1999), 224–237.
- [98] VAJDA, I. *Theory of Statistical Inference and Information*. Kluwer Academic Publishers, Dordrecht, 1989.
- [99] VIOLA, P. *Alignment by Maximization of Mutual Information*. Ph.d. dissertation, Massachusetts Institute of Technology, Cambridge, 1995.
- [100] WANG, J., AND JIANG, T. Nonrigid registration of brain MRI using NURBS. *Pattern Recognition Letters* 28, 2 (2007), 214–223.

- [101] WANG, Y., GU, X., CHAN, T., THOMPSON, P., AND YAU, S. Intrinsic brain surface conformal mapping using a variational method. In *SPIE International Symposium on Medical Imaging* (2004).
- [102] WANG, Y., GU, X., CHAN, T., THOMPSON, P., AND YAU, S. Volumetric harmonic brain mapping. In *In ISBI'04: IEEE International Symposium on Biomedical Imaging: Macro to Nano* (2004), pp. 1275–1278.
- [103] WANG, Y., GU, X., AND YAU, S. Volumetric harmonic map. *Communications in Information and Systems* 3, 3 (2004), 191–202.
- [104] WELCH, W., AND WITKIN, A. Variational surface modeling. *Computer Graphics* 26, 2 (1992), 157–166.
- [105] YAO, J., AND TAYLOR, R. Tetrahedral mesh modeling of density data for anatomical atlases and intensity-based registration. In *Proceedings of the third International Conference on Medical Image Computing and Computer-Assisted Intervention* (2000), pp. 531–540.
- [106] ZHANG, L., BAE, J., HARDY, W., MONSON, K., MANLEY, G., GOLDSMITH, W., YANG, K., AND KING, A. Computational study of the contribution of the vasculature on the dynamic response of the brain. *Stapp Car Crash Journal* 46 (2002), 145–164.
- [107] ZHANG, L., YANG, K., DWARAMPUDI, R., LI, K. O. T., KUN, C., HARDY, W., KHALIL, T., AND KING, A. Recent advances in brain injury research: A new human head model development and validation. *Stapp Car Crash Journal* 45 (2001), 369–393.
- [108] ZHANG, Y., HUGHES, T., AND BAJAJ, C. Automatic 3D mesh generation for a domain with multiple materials. In *Proceedings of the 16th International Meshing Roundtable* (2007), pp. 367–386.

- [109] ZUO, C., JIANG, A., BUFF, B., MAHON, T., AND WONG, T. Automatic motion correction for breast MR imaging. *Radiology* 198, 3 (1996), 903–906.

ABSTRACT

DYNAMIC MULTIVARIATE SIMPLEX SPLINES FOR VOLUME REPRESENTATION AND MODELING

by

YUNHAO TAN

August 2010

Advisor: Dr. Jing Hua

Major: Computer Science

Degree: Doctor of Philosophy

Volume representation and modeling of heterogeneous objects acquired from real world are very challenging research tasks and playing fundamental roles in many potential applications, e.g., volume reconstruction, volume simulation and volume registration. In order to accurately and efficiently represent and model the real-world objects, this dissertation proposes an integrated computational framework based on dynamic multivariate simplex splines (DMSS) that can greatly improve the accuracy and efficacy of modeling and simulation of heterogeneous objects. The framework can not only reconstruct with high accuracy geometric, material, and other quantities associated with heterogeneous real-world models, but also simulate the complicated dynamics precisely by tightly coupling these physical properties into simulation. The integration of geometric modeling and material modeling is the key to the success of representation and modeling of real-world objects.

The proposed framework has been successfully applied to multiple research areas, such as volume reconstruction and visualization, nonrigid volume registration, and physically based modeling and simulation.

AUTOBIOGRAPHICAL STATEMENT

YUNHAO TAN

Yunhao Tan is a Ph.D. candidate in the Department of Computer Science at Wayne State University where he is a research assistant in the Graphics & Imaging Laboratory. He received his B.E. degree from Beijing Information Technology Institute in 2001, then he worked for Beijing Bear Technology Group as a software engineer till 2003. His research interests include computer graphics, visualization, and medical imaging. He is a student member of IEEE.